Title: Hypoxia Promotes Early Tumorigenesis through Dynamical-Mechanical Balance and Genetic Instability

Authors: Zhengduo Wang[1], Li Tian[2], Bo Li[1,*]

Affiliations:

[1]The Institute for Advanced Studies, Wuhan University, Wuhan, 430072, China.

[2]Department of Physics, Wenzhou University, Wenzhou, 325000, China.

[*]Corresponding Author: libo@whu.edu.cn

Abstract: Understanding early tumor formation is essential for cancer prevention, but most studies focus on later stages. Hypoxia, a key feature of the tumor microenvironment, influences cancer progression, yet its impact on early tumorigenesis remains vague. Here, we record 3D tumor spheroid development under hypoxic conditions by live cell imaging, enabling the first real-time study of tumor formation from a single cell. We find that hypoxia accelerates tumorigenesis by promoting directional movement and spheroid fusion. Meanwhile, hypoxia induces genetic instability, indicated by tiny nuclei cells and chromosomal aneuploidy. The interplay between dynamic and genetic instability optimizes the mechanical properties of the spheroid, creating positive feedback that drives further proliferation. These findings suggest potential strategies for early cancer prevention by targeting the environmental factors that influence dynamic-genetic coupling.

Main Text:

Introduction.

Cancer becomes life-threatening after multiple stages of transformation. Hallmarks of advanced stages, such as metastasis, typically indicate a poorer prognosis (*1*). Thus, characterizing tumor features earlier is critical for effective detection and prevention (*2, 3*). The prevailing model of early tumorigenesis posits that mutations confer a survival advantage, enabling transformed cells to proliferate and form primary tumors (*4*). However, this model remains indirectly supported. *In vivo* studies in animal models or patient samples rely predominantly on retrospective analyses, leaving early tumorigenesis poorly understood. Live cell imaging platforms enable direct observation of cellular processes within precisely controlled environments (*5, 6*). Recent advances in 3D culture systems now enable *ex vivo* study of more complex processes (*7, 8*), offering new avenues to investigate early tumorigenesis.

Hypoxia is a key microenvironmental factor that promotes cancer initiation and progression (*9-11*). While classical hypoxia signaling pathways influence diverse cellular processes (*12-17*), their role in early tumorigenesis remains unclear, largely due to a lack of direct evidence. Molecular analyses alone cannot capture the dynamic, spatial changes—like cell movement and fusion—that are critical in development (*18*) and metastasis (*19*). Furthermore, tumor cells interact with multiple environmental factors. Although mechanical forces influence tumorigenesis by modulating mechanical properties and adhesion (*20-22*), their interplay with hypoxia is poorly understood (*23*).

We developed an integrated platform to investigate early tumor formation, addressing a critical gap in understanding tumorigenesis. Hypoxia dramatically accelerates this process (**Fig. 1**). Contrary to molecular-centric models, we demonstrate that directional spheroid dynamics and fusion drive early tumorigenesis (**Fig. 2A-2D**). This fusion is facilitated by optimized mechanical-dynamical-molecular couplings and structurally supported by outreaching F-actin with underlying YAP signaling (**Fig. 2E-2F, 2I-2Q**). A concurrent emergence of genetic instability is marked by a new population of micronuclei cells, aneuploidy, and increased mitochondria number (**Fig. 3**). Post-fusion, a mechanics-genetic instability coupling promotes proliferation via p53 pathway modulation, further enhancing hypoxic growth (**Fig. 4**). These findings redefine hypoxia's role in early tumor formation and challenge classical models focused solely on molecular cell-cycle pathways.

The research platform includes several components (**Fig. S1**). First, a human kidney-derived tumor cell line, genetically modified for protein visualization, was used to analyze underlying mechanisms (**Fig. S2**, **Tables S1, S2**). The HEK293T tumour cell line (*7, 8, 24-26*) was seeded in a Matrigel suspension, where cells grew as 3D spheroids by occupying cavities larger than the spheroids (**Fig. S3A, S3B**). Notably, only in 3D culture did cancer and cancer stem cell markers express fully (**Figs. S4A-S4C**), rationalizing the system as a model for tumorigenesis (*25, 27*). A spinning-disk confocal microscope, coupled with a three-gas incubator, enabled long-term live-cell imaging with minimal phototoxicity. By adjusting nitrogen gas supply, tumorigenesis was observed under different oxygen conditions, from hypoxia (2%) to normoxia (21%). Finally, live-cell imaging data were analyzed using AI-assisted segmentation (**Fig. S3C, S3D**) alongside

molecular cell biology data (**Tables S3, S4**) to elucidate the mechanism. Further experimental details are provided in the **Methods** section.

Hypoxia Promotes Tumorigenesis Through Directional Fusion.

After 42 hours of culture, tumor spheroids formed under 2% oxygen were significantly larger than those grown under normoxic conditions (**Fig. 1A, Movie S1**). Quantitative analysis shows a fourfold increase in tumor size and total cell number under hypoxia, with a moderate decrease in spheroid number by 31% (**Fig. 1B**). These results clearly indicate that hypoxia accelerates early tumorigenesis. Two dynamic processes contribute to this effect: fusion between tumor spheroids and growth driven purely by cell proliferation. For both normoxia and hypoxia, fusion accounts for approximately 70% of tumorigenesis, significantly outweighing the ~30% contribution from proliferation alone (**Fig. 1C**). Under hypoxia, fusion frequency doubles (**Fig. 1D**), and fusion event duration decreases by 55% (**Fig. 1E**), leading to increased tumor size in a shorter time (**Movie S2**).

Fusion events can be further classified into two modes (**Fig. 1F**). In the directional mode, tumor spheroids move freely within the Matrigel network until their outer surfaces make contact (**Fig. 1H, Movie S3**). We refer to this as "directional fusion". In the growth mode, spheroid centers oscillate near their initial positions, and fusion results as a by-product of growth (**Fig. 1G, Movie S4**). Under hypoxic conditions, directional fusion predominates (**Fig. 1F**), indicating that hypoxia drives early tumorigenesis by increasing spheroid dynamics. Based on these results, we conclude that directional fusion events and associated spheroid dynamics are key drivers of enhanced tumorigenesis.

Tumor cells within spheroids exhibit greater survival than isolated cells in 3D cultures (*28, 29*), fostered by a protective microenvironment of close cell-cell contacts. This enhanced viability promotes cell dynamics and proliferation, establishing a positive feedback loop that accelerates tumorigenesis. Time-resolved analysis supports this model (**Figs. 1K–1N**). Under hypoxia, spheroid speed increases immediately, confirming dynamics as central to tumorigenesis. This rapidly lowers barriers to contact, elevating fusion frequency after a brief 6-hour lag. Proliferation rates rise ~10 hours later, reflecting improved survival in larger spheroids, with a marked increase in overall spheroid size signifying robust tumorigenesis after ~24 hours (**Fig. 1L**). This cascade is absent under normoxia, where speed, fusion, and proliferation remain stable (**Fig. 1K**). Thus, hypoxia initiates a cascade where enhanced dynamics drive fusion, which in turn promotes growth.

Accompanying the directional fusion process, notable heterogeneity in both the dynamics and morphology of spheroids emerges. Under hypoxic conditions, the standard deviations of both spheroid speed and size increase significantly compared to those observed in normoxia (**Figs. 1O, 1P**). As two spheroids are undergoing directional fusion, the dynamics of them slow down, aligning with the sharp decrease in speed observed approximately 10 hours after hypoxia treatment (**Fig 1L**). Since not all spheroids undergo fusion, those growing solely through proliferation naturally remain smaller than those formed via directional fusion, leading to a broader distribution of spheroid sizes under hypoxia (**Fig. 1P**).

Dynamical and Mechanical Balance Facilitates Spheroid Fusion.

Known its critical role in tumorigenesis, we examine the cellular and molecular mechanisms underlying the directional movements. Representative spheroid trajectories (**Figs 2A-2D**) show navigation ranges prior to fusion. Under hypoxia, spheroids become unpinned from their original positions, moving freely in 3D space, with speed increases by 57.4 % (**Fig. S5A, S5B**), allowing fusion to occur over greater distances (**Fig. S5C**). Remarkably, the motion of fusing spheroids shifts from a random walk to directional movement toward each other (**Figs. S5D, S5E**), efficiently enabling fusion and enhancing its frequency.

Hypoxic spheroids modulate their mechanics and morphology to facilitate directional fusion. They exhibit reduced circularity (**Fig. 2E**), greater deformation over time (**Fig. 2F**), and undergo more extensive structural reorganization after laser ablation of single cells (**Fig. 2G, Movie S5**). Nano-indentation confirms that individual cells within these spheroids are softer (**Fig. 2H**). Collectively, these mechanical adaptations enhance spheroid dynamics (**Figs. S5A-S5C**) and shorten fusion time (**Fig. 1E**). To define the molecular basis of these dynamical-mechanical couplings, we perturbed cell mechanics pharmacologically and genetically (**Table S5**). Enhancing actin polymerization phenocopies hypoxia, increasing tumor formation and fusion frequency (**Figs. 1C, 1D, Movie S6**), while its inhibition suppresses them. This manipulation also recapitulates hypoxic effects on circularity, fusion time, and heterogeneity (**Figs. 1E, 1O, 1P, 2E, 2F**). Chronological analysis confirms that actin polymerization drives a dynamic sequence identical to hypoxia (**Figs. 1M, 1N**), establishing it as a key molecular regulator.

The functional role of actin polymerization in early tumorigenesis observed in the present experiments implies the activation of those signal pathways that control cell responses to mechanical cues under hypoxia (*30*), although at the time of promoted actin polymerization, no upregulation of HIF1α yet occurs (**Fig. S4I**). Among those, Hippo signaling and its core regulator, YAP, play pivotal roles by regulating actin cytoskeleton dynamics and cellular mechanics (*31, 32*). Immunofluorescence staining reveals significant YAP1 nuclear accumulation under hypoxia (**Figs. 2I, 2J**) As the interaction between YAP and actin polymerization is mutual (*33, 34*), the YAP1 can in turn facilitate the fusion of tumor spheroids.

To define the structural basis of directional fusion, we analyzed subcellular dynamics. Immunostaining under hypoxia reveals that F-actin forms distinctive outreaching structures, specifically bridging adjacent fusing spheroids (**Figs. 2L, S6A-S6H; Movie S7**). These extensions are polarized, localizing to the inter-spheroid gap, and can attain lengths comparable to a spheroid's diameter (**Fig. 2K**), vastly extending their sensing range. Live-cell imaging confirms that F-actin protrusions dynamically elongate toward a target spheroid hours before fusion (**Figs. S6E-S6H; Movie S8**). Chronological analysis shows actin elongation coincides with accelerated spheroid movement and distance reduction, confirming their correlation (**Fig. 2M**). In addition, laser ablation of these F-actin extensions reduces hypoxic tumorigenesis (**Fig. S7**), proving their essential role as the structural basis for remote sensing and directional fusion.

To further assess the roles of cell-cell adhesion and cell-ECM interaction, we performed RNAi and OE manipulations of DSG2 and integrin β-3 (ITGB3), both of which have been reported to be hub modulator in tumorigenesis (*35, 36*). Here we briefly report that tumor spheroids reduce intercellular adhesion to facilitate greater deformation and enhance dynamics, while cell-ECM interaction plays a minor role in the hypoxic environment (**Fig. S8**). More detailed analysis of

these experiments can be found in the **Supplementary Materials**. In 2D cultures, however, cell-ECM interactions influence both tumorigenesis and directional fusion (**Fig. S9**), highlighting fundamental differences in dynamical-mechanical couplings between 2D and 3D culture systems.

The fusion and deformation of tumor spheroids represent complex adaptations beyond equilibrium physics. While greater deformation typically signifies reduced stiffness in equilibrium systems (*37*), we observe that actin polymerization—generally associated with increased stiffness (*38*)—paradoxically enhances deformation and dynamics here (**Figs. 1C-1F, 2E-2G, S5A-S5C**). Furthermore, neither additional actin polymerization nor DSG2 knockdown under hypoxia further enhances fusion (**Fig. S10**), indicating an optimal concentration for each molecule to maintain spheroid function. Transcriptomic analyses reveal hypoxia-induced upregulation of gene clusters involved in metabolism, cancer signaling, cytoskeletal dynamics, and ECM remodeling (**Figs. 2N, 2O, 2P, 2Q**). These findings show cells finely optimize their biomechanical and biochemical properties in response to hypoxia.

Genomic instability manifested as tiny cells and aneuploidy.

Following hypoxia treatment, a distinct cell type with notably small nuclei emerges within the tumor spheroids (**Figs 3A, 3B, 3C, 3D, S6**; **Movie S9**). These “tiny” cells, with nuclear sizes averaging 23.9 % of that of typical nuclei, are virtually absent under normoxic conditions. The nuclei size distribution shifts to a bimodal pattern under hypoxia, contrasting with the continuous distribution observed in normoxia (**Fig. 3E**). Chromosome immunostaining verifies these tiny nuclei as ring-shaped cells (**Fig. 3F**) rather than organelle-like entities, and their number-increase rate is nearly quadruple that of normal cells (**Fig. 3G**). The emergence of distinct nuclear size distribution and number increased rate provides strong evidence that these tiny nuclei represent a novel cell subtype within the tumor spheroid. This adaptation to environmental stress suggests underlying genetic instability, a known hallmark of cancer (*39*).

Tiny cells are pivotal for directional fusion. They localize predominantly at the spheroid surface, clustering specifically at the interface toward a neighboring spheroid to bridge the gap (**Figs. 3H-3J**). These cells colocalize with outreaching F-actin, which forms connecting channels (Inset of **Fig. 2L**). Their functional importance is confirmed by laser ablation, which reduces tumorigenesis (**Figs. S7A-S7D**). We propose that directional fusion arises from cytoskeletal-nuclear coordination: F-actin extends the sensing range, while motile tiny cells (**Fig. 3K**) act as "sentinels," traversing these channels and facilitating mass transport. Their high motility enables rapid positional adjustment and influences overall spheroid dynamics (**Figs. 1O, 1P**). Thus, the coupling between dynamical and genetic properties jointly determines the tumorigenesis rate.

At the chromosomal level, the genetic instability is manifested as aneuploidy. DNA fluorescence in situ hybridization (FISH) experiments show that under both normoxic and hypoxic conditions, more than 50% of the cells exhibited three copies of chromosomes 8 and 17 rather than the normal diploid number of two (**Figs. 3L, 3M, 3N, 3O**). This result is consistent with the real space observation (**Figs. 3L, 3M, 3N, 3O**) and sequencing analysis (**Figs. S4A, S4B, S4C**) that the 293T cells present cancer stem cell-like character under in 3D-cultured, namely, the 3D environment has already induced some degree of genetic instability to the tumor cells. Hypoxia treatment further increased the proportion of cells with chromosome 8 and 17 copy numbers other than two or three by about one fold, indicating elevated genomic instability at the chromosomal level. In particular,

the genes that encode TP53 and JUP lie on chromosome 17 (*40*, *41*), the abnormality of which is consistent with the loss of proliferation control by the mutation of p53 structure; and regulation of cell-cell adhesion, respectively. Note that the increase in chromosome number has already been detectable as early as 12 hours after hypoxia treatment, proving it to be a causal effect, just as the directional fusion, for the enhanced tumorigenesis. The aneuploidy persisted throughout the whole time course of the experiments since its occurrence. Usually, the genetic instability in cancer is discussed at a much later stage after the primary tumor has been constructed (*39*), it is remarkable that it occurs so early, accompanying the process that the tumors are formed from a few transformed cells.

Mitochondrial carry genes that regulate the cell metabolism (*42*), and thus act as the center of energy supply for bioactivities. Scanning electron microscopy revealed that the number of mitochondria per cell under hypoxic conditions is 30 % higher, compared with that of normoxia (**Figs. 3P, 3Q**). This consists of the genetic stability at the organelle level. The elevated mitochondrial count could help provide additional energy to support directional movement and enhanced cell proliferation under hypoxia.

Stimulated cell cycle enhances proliferation and spheroid growth.

Following directional fusion, the rate of cell proliferation shows a marked increase, indicating a coupling between spheroid dynamics and cell proliferation (**Fig. 1L**). Although cell proliferation-driven growth of the tumor spheroid is less prominent than fusion, it still accounts for approximately 20 % of the overall tumorigenesis rate (**Fig. 1C**). Under hypoxic conditions, this contribution rises by 40 % (**Fig. 1C**), alongside a substantial increase in cell proliferation rate (**Figs. 4A, 4B**), underscoring the importance of proliferation-driven growth in tumor spheroid development.

To visualize cell cycle dynamics, we employed the FUCCI technique, enabling precise tracking of cell cycle phases (**Supplementary Materials, Table S2**). Statistical analysis reveals that under hypoxia, the proportion of cells in the S/G2/M phases is approximately 10 % higher than under normoxia (**Fig. 4C**), suggesting a hypoxia-induced acceleration of cell proliferation. Over time, this effect amplifies, with nearly all cells entering the S/G2/M phases after 42 hours of hypoxia exposure (**Figs. 4E, 4I; Movie S10**). Notably, the rate of increase in the S/G2/M cell proportion is non-linear. Initially, the proportion of cells in G1 and S/G2/M remains stable, but after a critical threshold, the S/G2/M phase proportion begins a rapid ascent (**Fig. 4I**), marking a proliferation rate jump confirmed by cell counts (**Fig. 1L**). This analysis supports the hypothesis that larger spheroids, which are better suited for cell survival in 3D culture, stimulate cell proliferation, contributing to overall spheroid growth.

Mechanistically, the stimulation of the cell cycle within the nucleus is linked to cytoskeletal dynamics, echoing previous studies at the molecular level (*43*). When actin polymerization is activated, the proportion of cells in S/G2/M phases increases, even in the absence of hypoxia (**Fig. 4J**). Conversely, inhibiting actin polymerization prevents this increase in S/G2/M phase cells under hypoxia (**Fig. 4K**). Tiny cells, which number increase at a rate four times that of normal cells, fail to form when actin polymerization is suppressed (**Fig. 3E**). Thus, in addition to hypoxia, specific cytoskeletal conditions are essential for the generation of tiny cells and the enhanced

proliferation they drive. Therefore, the proliferation within tumor spheroids are modulated by cytoskeletal mechanics, linking external mechanical properties to nuclear behavior.

Immunostaining reveals the mechanism for stimulated cell cycling via p53 (**Figs. 4L-4N**). As a known guardian of genome integrity (*44*), p53's role in tumorigenesis is context-dependent (*45*, *46*). We find that under normoxia and early hypoxia, nuclear p53 acts to restrict proliferation in already-transformed HEK293T cells, which exhibit spheroid growth and aneuploidy even at baseline (**Figs. 1D, 2B, 2E, 2F, 3N, 3O**). However, after 48 hours of hypoxia, prolonged stress induces p53 mutation, disrupting its nuclear localization and function (**Figs. 4L-4N**). This loss of proliferative control accelerates growth, as confirmed by FUCCI imaging. Thus, proliferation emerges from dynamic-genetic coupling: hypoxia-driven fusion and genetic instability increase cell numbers, with larger spheroids enhancing survival, while p53 mutation releases cell-cycle checkpoints, collectively propelling a malignant growth state.

Summary and Discussion

In summary, this study provides experimental insights into how hypoxia accelerates early tumorigenesis (**Fig. S12**). By establishing a 3-dimensional culture, we are able to construct an *ex vivo* system in which tumor spheroid are formed from individual cancer stem cells. We find that the enhanced directional dynamics, whose underlying balance with the cytoskeletal mechanics and cell cycle kinetics are the major driving factor of tumorigenesis. The genetic instability fully involves early tumorigenesis by coupling with the dynamical processes. These findings not only challenge traditional linear models of early tumorigenesis that often reduce it to simple proliferation and growth but also offer potential prevention or therapeutic strategy aiming at the dynamo-mechano-physio-coupling, in addition to those targeting classical signal pathways (*47*). The scenario proposed by our experiment is valid for the primary tumor formation from individual cancer stem cell (*48*), as well for the metastatic formation from the disseminated cells at the distal end (*49*).

Our findings also raise new research questions. Dynamics, a concept typically outside the focus of molecular cell biology, proves critical for understanding tumorigenesis in this context. However, the transcriptomic analysis fails to identify classical signaling pathways in existing databases (**Fig. S13**), although chemical hypoxia induced by $CoCl_2$ replicates similar spheroid behaviors (**Fig. S14**) – suggesting unknown molecular mechanisms underlying the observed dynamic processes. The relation between phenotypic heterogeneity and genetic instability needs to be further elucidated. Moreover, the consequence of the behaviors in early tumorigenesis, namely, their potential involvement in later stages of cancer development, such as metastasis, should be tested by an *in vivo* model. Last but not least, whether the model proposed by this work is general to tumorigenesis needs to be tested in other specific cancer cell lines.

References and Notes

1. D. Hanahan, R. A. Weinberg, The hallmarks of cancer. *Cell* **100**, 57-70 (2000).
2. D. Crosby *et al.*, Early detection of cancer. *Science* **375**, eaay9040 (2022).

3. K. Unger-Saldaña, Challenges to the early diagnosis and treatment of breast cancer in developing countries. *World J Clin Oncol* **5**, 465-477 (2014).
4. C. A. Klein, Parallel progression of primary tumours and metastases. *Nat Rev Cancer* **9**, 302-312 (2009).
5. J. Chen, K. E. Poskanzer, M. R. Freeman, K. R. Monk, Live-imaging of astrocyte morphogenesis and function in zebrafish neural circuits. *Nat Neurosci* **23**, 1297-1306 (2020).
6. A. Domingo-Muelas *et al.*, Human embryo live imaging reveals nuclear DNA shedding during blastocyst expansion and biopsy. *Cell* **186**, 3166-3181.e3118 (2023).
7. A. Le *et al.*, Tumorigenicity of hypoxic respiring cancer cells revealed by a hypoxia-cell cycle dual reporter. *Proc Natl Acad Sci U S A* **111**, 12486-12491 (2014).
8. S. Riffle, R. N. Pandey, M. Albert, R. S. Hegde, Linking hypoxia, DNA damage and proliferation in multicellular tumor spheroids. *BMC Cancer* **17**, 338 (2017).
9. A. Mohyeldin, T. Garzón-Muvdi, A. Quiñones-Hinojosa, Oxygen in stem cell biology: a critical component of the stem cell niche. *Cell Stem Cell* **7**, 150-161 (2010).
10. R. G. Bristow, R. P. Hill, Hypoxia and metabolism. Hypoxia, DNA repair and genetic instability. *Nat Rev Cancer* **8**, 180-192 (2008).
11. D. M. Gilkes, G. L. Semenza, D. Wirtz, Hypoxia and the extracellular matrix: drivers of tumour metastasis. *Nat Rev Cancer* **14**, 430-439 (2014).
12. B. Keith, R. S. Johnson, M. C. Simon, HIF1α and HIF2α: sibling rivalry in hypoxic tumour growth and progression. *Nat Rev Cancer* **12**, 9-22 (2011).
13. M. E. Hubbi, G. L. Semenza, Regulation of cell proliferation by hypoxia-inducible factors. *Am J Physiol Cell Physiol* **309**, C775-782 (2015).
14. J. H. Park *et al.*, Tumor hypoxia represses γδ T cell-mediated antitumor immunity against brain tumors. *Nat Immunol* **22**, 336-346 (2021).
15. C. Befani, P. Liakos, The role of hypoxia-inducible factor-2 alpha in angiogenesis. *J Cell Physiol* **233**, 9087-9098 (2018).
16. E. B. Rankin, A. J. Giaccia, Hypoxic control of metastasis. *Science* **352**, 175-180 (2016).
17. S. Ma *et al.*, Hypoxia induces HIF1α-dependent epigenetic vulnerability in triple negative breast cancer to confer immune effector dysfunction and resistance to anti-PD-1 immunotherapy. *Nat Commun* **13**, 4118 (2022).
18. M. N. Shahbazi, E. D. Siggia, M. Zernicka-Goetz, Self-organization of stem cells into embryos: A window on early mammalian development. *Science* **364**, 948-951 (2019).
19. C. H. Stuelten, C. A. Parent, D. J. Montell, Cell motility in cancer invasion and metastasis: insights from simple model organisms. *Nat Rev Cancer* **18**, 296-312 (2018).
20. A. Labernadie *et al.*, A mechanically active heterotypic E-cadherin/N-cadherin adhesion enables fibroblasts to drive cancer cell invasion. *Nat Cell Biol* **19**, 224-237 (2017).
21. H. Hamidi, J. Ivaska, Every step of the way: integrins in cancer progression and metastasis. *Nat Rev Cancer* **18**, 533-548 (2018).
22. V. F. Fiore *et al.*, Mechanics of a multilayer epithelium instruct tumour architecture and function. *Nature* **585**, 433-439 (2020).

23. D. Wirtz, K. Konstantopoulos, P. C. Searson, The physics of cancer: the role of physical interactions and mechanical forces in metastasis. *Nat Rev Cancer* **11**, 512-522 (2011).
24. A. A. Stepanenko, V. V. Dmitrenko, HEK293 in cell biology and cancer research: phenotype, karyotype, tumorigenicity, and stress-induced genome-phenotype evolution. *Gene* **569**, 182-190 (2015).
25. B. G. Debeb *et al.*, Characterizing cancer cells with cancer stem cell-like features in 293T human embryonic kidney cells. *Mol Cancer* **9**, 180 (2010).
26. C. Shen *et al.*, The tumorigenicity diversification in human embryonic kidney 293 cell line cultured in vitro. *Biologicals* **36**, 263-268 (2008).
27. B. Keith, M. C. Simon, Hypoxia-inducible factors, stem cells, and cancer. *Cell* **129**, 465-472 (2007).
28. N. Aceto *et al.*, Circulating tumor cell clusters are oligoclonal precursors of breast cancer metastasis. *Cell* **158**, 1110-1122 (2014).
29. K. J. Cheung, A. J. Ewald, A collective route to metastasis: Seeding by tumor cell clusters. *Science* **352**, 167-169 (2016).
30. H. S. Leong, A. F. Chambers, Hypoxia promotes tumor cell motility via RhoA and ROCK1 signaling pathways. *Proc Natl Acad Sci U S A* **111**, 887-888 (2014).
31. M. Aragona *et al.*, A mechanical checkpoint controls multicellular growth through YAP/TAZ regulation by actin-processing factors. *Cell* **154**, 1047-1059 (2013).
32. G. Halder, S. Dupont, S. Piccolo, Transduction of mechanical and cytoskeletal cues by YAP and TAZ. *Nat Rev Mol Cell Biol* **13**, 591-600 (2012).
33. A. Nagasawa-Masuda, K. Terai, Yap/Taz transcriptional activity is essential for vascular regression via Ctgf expression and actin polymerization. *PLoS One* **12**, e0174633 (2017).
34. J. Gao *et al.*, Mechanical force regulation of YAP by F-actin and GPCR revealed by super-resolution imaging. *Nanoscale* **12**, 2703-2714 (2020).
35. S. Qin *et al.*, DSG2 expression is correlated with poor prognosis and promotes early-stage cervical cancer. *Cancer Cell Int* **20**, 206 (2020).
36. C. Zhu *et al.*, ITGB3/CD61: a hub modulator and target in the tumor microenvironment. *Am J Transl Res* **11**, 7195-7208 (2019).
37. I. Levental, P. C. Georges, P. A. Janmey, Soft biological materials and their impact on cell function. *Soft Matter* **3**, 299-306 (2007).
38. J. Stricker, T. Falzone, M. L. Gardel, Mechanics of the F-actin cytoskeleton. *J Biomech* **43**, 9-14 (2010).
39. C. Lengauer, K. W. Kinzler, B. Vogelstein, Genetic instabilities in human cancers. *Nature* **396**, 643-649 (1998).
40. F. van Kampen *et al.*, Deletion of 17p in cancers: Guilt by (p53) association. *Oncogene* **44**, 637-651 (2025).
41. L. De Marchis, C. Cropp, Z. M. Sheng, S. Bargo, R. Callahan, Candidate target genes for loss of heterozygosity on human chromosome 17q21. *Br J Cancer* **90**, 2384-2389 (2004).

42. J. L. Fetterman, S. W. Ballinger, Mitochondrial genetics regulate nuclear gene expression through metabolites. *Proc Natl Acad Sci U S A* **116**, 15763-15765 (2019).
43. P. P. Provenzano, P. J. Keely, Mechanical signaling through the cytoskeleton regulates cell proliferation by coordinated focal adhesion and Rho GTPase signaling. *J Cell Sci* **124**, 1195-1205 (2011).
44. R. Weinberg, The Biology of Cancer. (2006).
45. P. Carmeliet *et al.*, Role of HIF-1alpha in hypoxia-mediated apoptosis, cell proliferation and tumour angiogenesis. *Nature* **394**, 485-490 (1998).
46. T. G. Graeber *et al.*, Hypoxia-mediated selection of cells with diminished apoptotic potential in solid tumours. *Nature* **379**, 88-91 (1996).
47. W. R. Wilson, M. P. Hay, Targeting hypoxia in cancer therapy. *Nat Rev Cancer* **11**, 393-410 (2011).
48. R. J. Ward, P. B. Dirks, Cancer stem cells: at the headwaters of tumor development. *Annu Rev Pathol* **2**, 175-189 (2007).
49. W. T. Liao, Y. P. Ye, Y. J. Deng, X. W. Bian, Y. Q. Ding, Metastatic cancer stem cells: from the concept to therapeutics. *Am J Stem Cells* **3**, 46-62 (2014).

Acknowledgments: We thank Min Bao from Oujiang Laboratory for helpful discussions; Ruirui Gao and Yeqing Leng from Wuhan University for sharing monoclonal transfected cell lines; Meng Shao, Limin Zheng, and Yilin Sun from Westlake University for scanning electron microscopy imaging; Yinping Gao from Westlake University and Jie Wang from Oujiang Laboratory for STED imaging; Danyan Yang from CSR biotech for SIM imaging; and ChatGTP for grammar checking and text polishing.

Funding:

National Natural Science Foundation of China, Distinguished Young Scholars Grant (Overseas).

Wuhan University, Talents Startup Funding.

Author contributions:

Conceptualization: BL

Methodology: BL, ZDW

Investigation: BL, ZDW, LT

Visualization: ZDW

Funding acquisition: BL

Project administration: BL

Supervision: BL

Writing – original draft: BL, ZDW

Writing – review & editing: BL, ZDW, LT

Competing interests: The Authors declare that they have no competing interests.

Data and materials availability: All data are available in the main text or the supplementary materials.

Supplementary Materials

Materials and Methods

Supplementary Text

Figs. S1 to S13

Tables S1 to S5

References (1-50)

Movies S1 to S10

Data S1 to S13

Code S1 to S3

Figure Captions

Fig. 1. Hypoxia promotes early tumorigenesis by directional fusion. (**A**) Confocal images of HEK293T cells cultured in 3D Matrigel under 21% oxygen (left) and 2% oxygen (right) for 42 hours. The images are the typical reflection of more than three independent experiments. The green and red channels are LifeAct and H2B, respectively. The scale bar is 100 µm. (**B**) Cell number, maximum cross-sectional area of tumor spheroids, and total number of spheroids after 48 hours of 3D culture. (**C**) Tumorigenesis rate of HEK293T cells under different conditions of normoxia, hypoxia and PHAi treatments. The shaded area in the first two columns represents the parts of tumorigenesis contributed by growth. (**D**) Fusion frequency of tumor spheroids under different culture conditions. (**E**) Time required for the directional fusion under different culture conditions of normoxia, hypoxia, PHAi, and RNAi treatments. (**F**) Proportion of directional and growth modes in the fusion under different culture conditions of normoxia, hypoxia, PHAi, and RNAi treatments. (**G, H, I, J**) Representative confocal images of more than three independent experiments that reflect the tumor spheroids fusion under different culture conditions. The left panels are images taken at 0 hours and the right panels are taken at 42 hours after the treatment. Compared with the normal 21% oxygen control (**G**), directional fusion is promoted under 2% hypoxia condition (**H**) or Rho activator II treatment (**I**). The directional fusion under hypoxia disappears after Y-27632 treatment (**J**). Green and red channels are LifeAct and H2B, respectively. The scale bar is 20 µm. (**K, L, M, N**) Time evolution of maximum cross-sectional area, fusion frequency, cell number, and speed of the spheroids under conditions of 21% Oxygen (**K**), 2% Oxygen (**L**), 21% Oxygen with Rho Activator II (**M**), and 2% Oxygen with Y-27632 (**N**). (**O, P**) Standard deviation of the spheroid speed (**O**) and maximum cross-sectional area (**P**) across different culture conditions. For all statistical plots, unpaired Student's t-test ($n > 3$ experiments, data are mean ± SEM) was conducted for all data with **** $P < 0.0001$, *** $P < 0.001$, ** $P < 0.1$, * $P < 0.5$, ns $P > 0.5$. The error bars are the standard error of the mean of the data.

Fig. 2. Dynamics of the tumor spheroids during the directional fusion. (**A, B, C, D**) Typical trajectories of tumor spheroids in 24 hours under different culture conditions of normal 21% oxygen (**A**), 2% hypoxia (**B**), Rho-activate II treatment under normoxia (**C**), and Y-27632 treatment under hypoxia (**D**). The data is a typical reflection of three independent experiments. The colors represent different tumor spheroids. (**E**) Circularity of the tumor spheroid during directional fusion under different culture conditions. (**F**) Time evolution of the tumor spheroid circularity during the directional fusion under various culture conditions of normoxia, hypoxia, PHAi, and RNAi treatments. (**G**) Degree of deformation of the tumor spheroid after laser ablation under different culture conditions of 21% normal oxygen, 2% hypoxia, normoxia treated with Rho-activate II, and hypoxia treated with Y-27632. The wavelength of the laser is 405 nm and the power of ablation is 50 mW. (**H**) Cellular Young's modulus under normoxia or hypoxia culture conditions. Further promotion of actin polymerization or the inhibition of intercellular interactions under hypoxic conditions suppress early tumorigenesis. (**I**) Representative confocal images of YAP1 immunofluorescence in 3D cultured cancer cell spheroids under normoxic conditions for 48 h (left), hypoxic conditions for 12 h (middle), and hypoxic conditions for 48 h (right). YAP1

immunostaining is shown in red, and nuclei were counterstained with Hoechst (blue). The scale bar is 20 µm. (**J**) Quantification of mean YAP1 fluorescence intensity in the nucleus of 3D cultured cancer cell spheroids under normoxic conditions for 48 h, hypoxic conditions for 12 h, and hypoxic conditions for 48 h. (**K**) The length of out-reaching F-actin from the spheroid surface in normoxia and hypoxia conditions. (**L**) Typical immunostaining images of the tumor spheroids under normoxia (Left) and hypoxic (Right) conditions. The green channel is F-actin, the red is H2B and the blue channel is Hoechst. The dashed white circles indicate the outreaching F-acting structure that bridges two fusing tumor spheroids. The inset of right is an enlarged view of the outreaching F-actin channel between two spheroids. The dashed green line depicts the envelop of the spheroids and the channel. The dashed white circles demonstrate the tiny nuclei and the dashed red circles demonstrate the normal nuclei. The scale bar is 20 µm. (**M**) Time evolution of the F-actin bridge length, the distance between the spheroid and the spheroids' speed during directional fusion. (**N, O, P, Q**) Differential analysis of 3-dimensional HEK293T transcriptomic data under hypoxia and normoxia conditions. (**N**) KEGG biological process enrichment analysis of differentially expressed genes. The bubble plot shows the top ten enriched biological processes. The y-axis is described as follows. 1: extracellular structure organization, 2: extracellular matrix organization, 3: gland development, 4: nucleoside diphosphate metabolic process, 5: NAD metabolic process, 6: glucose catabolic process, 7: glucose catabolic process to pyruvate, I8: canonical glycolysis, 9: NADH regeneration, 10: glycolytic process through glucose−6−phosphate. (**O**) KEGG pathway enrichment analysis of differentially expressed genes. The bubble plot shows the top ten KEGG pathways. The y-axis is described as follows. 1: PI3K−Akt signaling pathway, 2: MAPK signaling pathway, 3: Calcium signaling pathway, J4: Oxidative phosphorylation, J5: Protein digestion and absorption, 6: ECM−receptor interaction, 7: Biosynthesis of amino acids, 8: Glycolysis / Gluconeogenesis, 9: Arginine and proline metabolism, 10: Pentose phosphate pathway. (**P**) KEGG enrichment analysis of differentially expressed genes related to cytoskeletal dynamics. The y-axis is described as follows. 1: cell growth, 2: cell−cell junction, 3: regulation of GTPase activity, 4: actin binding, 5: cell−substrate junction, 6: actin filament organization , 7: focal adhesion, 8: positive regulation of GTPase, 9: activity Ras GTPase binding, 10: tubulin binding,11: embryonic organ morphogenesis, 12: actin filament binding, 13: site of polarized growth, 14: adherens junction, 15: Rho GTPase binding, 16: actin filament, 17: Rac GTPase binding. (**Q**) KEGG molecular function enrichment analysis of differentially expressed genes. The y-axis is described as follows. 1: channel activity, 2: passive transmembrane transporter activity, 3: metal ion transmembrane transporter activity, L4: ion channel activity, 5: monovalent inorganic cation transmembrane transporter activity, 6: cation channel activity, 7: gated channel activity, 8: extracellular matrix structural constituent, 9: growth factor binding, 10: extracellular matrix structural constituent conferring tensile strength. For all the KEGG plots, the size of each bubble represents the number of genes involved, while the color indicates the significance level (p-value). The mRNA samples are extracted from cells in 3-dimensional culture after 24 hours of 2% (hypoxia) or 20% (normoxia) oxygen treatment. All data are from three independent experiments. For all statistical plots, unpaired Student's t-test ($n > 3$ experiments, data are mean ± SEM) was

conducted for all data with **** P < 0.0001, *** P < 0.001, ** P < 0.1, * P <0.5, ns P > 0.5. The error bars are the standard error of the mean of the data.

Fig. 3. Micronuclei, aneuploidy, and mitochondria hyperplasia. (**A, B, C, D**) Typical confocal images from more than three independent experiments of tumor spheroid composed of HEK293T-FUCCI cells in 3D culture for 42 hours under 2% oxygen conditions. The cells are labeled with FUCCI, in which the color indicates different stages of the cell cycle. - Red marks hCdt1, indicating cells are in the G1 phase, and green marks hGem, indicating cells are in the S/G2/M phases. The white dotted circle indicates the nucleus of the tiny cells. The scale bar is 10 µm. (**E**) Probability distribution of nucleus sizes under different 3D culture conditions of normoxia, hypoxia, normoxia treated with Rho-activate II, and hypoxia treated with Y-27632. The dashed line indicates a bimodal distribution in the probability of nuclear size under hypoxic conditions, suggesting the presence of nuclei with different sizes. (**F**) Representative stimulated emission depletion (STED) images of cells stained with SIR-DNA to label nuclei and tiny nuclei. The scale bar is 2.5 µm. (**G**) Relative changes in the number of tiny and normal nuclei over the same period of 42 hours. (**H**) Confocal images of HEK293T-FUCCI tumor spheroids during the directional fusion process. The tiny cells appear at the proximal gap between the two spheroids during the fusion but are not observed before and after. The white arrow in (**H**) indicates the nucleus of the tiny cells. The green and red channels are hCdt1 and hGem, respectively. (**I**) Probability distribution of the distance ("d" in the inset) between the tiny and normal cells the center of tumor spheroids during directional fusion. A distance of 1 indicates positioning at the spheroid's edge. The inset of (**I**) schematically demonstrates the relative positions between the tiny cells and the spheroids. (**J**) Probability distribution of the angle ("θ" in the inset of **(J**) between the tiny cell nucleus–spheroid center axis and the spheroid center-spheroid center axis during the directional fusion. A smaller θ value means a closer location to proximal ends of the axis that connects the mass centers of the two spheroids. The inset of (**J**) is the enlarged part of the gap region between two fusing spheroids. The white arrow indicates the nucleus of the tiny cells. (**K**) Speed of tiny and large nuclei in cells. (**L,M**) Representative confocal images showing DNA FISH labeling of the centromere of chromosome 8 (**L**) and chromosome 17 (**M**) in 3D-cultured cancer cell spheroids under normoxia (48 h, left) and hypoxia (48 h, right). The centromeres are visualized with green fluorescent labeling. Nuclei were counterstained with Hoechst (blue). The scale bar is 20 µm.(**N, O**)Statistical analysis of the probabilities of single cells having exactly 2, exactly 3, or a number not equal to 2 or 3, for chromosome 8 (**O**) and chromosome 17 (**N**), after treatment under normoxia for 48 h, hypoxia for 12 h, or hypoxia for 48 h. (**P**) Representative scanning electron microscopy (SEM) images of cancer spheroids under three-dimensional culture conditions, cultured for 42 h under 21% (left) and 2% (right) oxygen. Mitochondria are indicated by red circles. The scale bar is 5 µm. (**Q**) Quantitative analysis of the mitochondrial number per cell in cancer spheroids cultured under 21% and 2% oxygen for 42 h. For all statistical plots, unpaired Student's t-test (n > 3 experiments, data are mean ± SEM) was conducted for all data with **** P < 0.0001, *** P < 0.001, ** P < 0.1, * P <0.5, ns P > 0.5. The error bars are the standard error of the mean of the data.

Fig. 4. Hypoxia promotes spheroid growth in 3D by modulating the cell cycle. (**A**) Representative Confocal images of tumor spheroid under 21% oxygen (left) and 2% oxygen (right) conditions after 42 hours of 3D culture. The images are the typical reflection of more than three independent experiments. The green and red channels are LifeAct and H2B, respectively. The scale bar is 10 µm. (**B**) Proliferation rate of HEK293T cells under different 3D culture conditions of normoxia, hypoxia, and PHAi experiments. (**C**) Proportion of HEK293T cells in the S/G2/M phases under different 3D culture conditions of normoxia, hypoxia, and PHAi experiments. (**D, E, F, G**) Typical confocal images of tumor spheroids composed of HEK293T-FUCCI cell line under various culture conditions of normoxia control (**D**), hypoxia (**E**), normoxia with Rho-activate II treatment (**F**) and hypoxia with Y-27632 treatment (**G**). The upper column is images taken at 0 hours and the lower column is images taken at 42 hours. The green and red channels are hCdt1 and hGem, respectively. The scale bar is 20 µm. (**H, I, J, K**) Proportion of cells in G1 phase or S/G2/M phases as a function of time normoxia (**H**), hypoxia (**I**), normoxia with Rho-activate II treatment (**J**), and hypoxia with Y-27632 treatment (**K**). (**L,**) Representative structured illumination microscopy (SIM) and confocal images of TP53 immunofluorescence in 3D-cultured cancer cell spheroids following 48 h of normoxia (left), 12 h of hypoxia (middle), or 48 h of hypoxia (right). Red fluorescence indicates TP53, and blue fluorescence corresponds to Hoechst-stained nuclei. The scale bar is 10 µm. (**M, N**) Statistical analysis showing the probability of TP53 localizing to the nucleus (**M**) or to the cytoplasm (**N**) in cells subjected to 48 h of normoxia, 12 h of hypoxia, or 48 h of hypoxia. For all statistical plots, unpaired Student's t-test ($n > 3$ experiments, data are mean ± SEM) was conducted for all data with **** $P < 0.0001$, *** $P < 0.001$, ** $P < 0.1$, * $P < 0.5$, ns $P > 0.5$. The error bars are the standard error of the mean of the data.

Supplementary Materials for

Hypoxia Promotes Early Tumorigenesis through Dynamic and Genetic Instability

Authors: Zhengduo Wang[1], Li Tian[2], Bo Li[1, *]

Corresponding author: Bo Li, libo@whu.edu.cn

The PDF file includes:

Materials and Methods
Supplementary Text
Figs. S1 to S14
Tables S1 to S5
References

Other Supplementary Materials for this manuscript include the following:

Movies S1 to S10
Data S1 to S13
Code S1a to S1c

Materials and Methods

EXPERIMENTAL DETAILS

Cell line maintenance and culture. HEK293T (ATCC) cells were grown in DMEM (Adamas life, C8013-500mL) supplemented with 10% heat-inactivated FBS (Gibco). Cells were maintained in an incubator at 37 °C and 5 % CO2 and passaged every 2 to 3 days. Before imaging, the medium was changed or PHAi treatments were applied according to experimental requirements, including DMSO (Adamas Life, 75927AA, 30 μM), Rho Activator II (Cytoskeleton, Cat. # CN03, 2 μg/mL), or Y-27632 (Yesen, 53006ES08, 30 μM). The prepared cell samples were then transferred to a live-cell workstation, where confocal imaging was performed. The mycoplasma testing was conducted weekly on the cell lines using the Mycoplasma Detection Kit (Solea, CA1080). We use Corning Matrigel (356234-5mL) to create a 3D culture environment that assists the tumor cell in forming spheroids. (*1, 2*) After thawing the Matrigel according to the manufacturer's recommendations, mix it thoroughly with a pipette to ensure homogeneity. Dilute the Matrigel to a 50% concentration with a serum-free medium. Then pour the diluted Matrgel on the confocal dish and incubate at 37°C for 15 minutes to allow solidification. Finally, seed the cells on the confocal dish with solidified Matrigel and add complete culture medium.

Pharmaceutical interference experiment. Rho Activator II (CN03) from Cytoskeleton (*3, 4*), is stored in a desiccated state at 4°C for no more than 6 months. For reconstitution, briefly centrifuge to collect the product at the bottom of the tube and resuspend each vial in 200 μl of sterile water, place on ice for 10 minutes prior to mixing, and mix by gently pipetting up and down to yield a concentration of 0.1 μg/μl. During use, the compound was diluted in a culture medium to achieve a final concentration of 2 μg/mL for cell treatment. Y-27632 was purchased from Yeasen Biotechnology and is provided as a powder with a purity exceeding 98 % (*5, 6*). The powder should be aliquoted and stored at -20 °C dry environment for no more than 2 years. To prepare a stock solution, 10 mg of Y-27632 was dissolved in 312 μL of DMSO to create a 100 mmol/L solution, which was then diluted 10-fold with DMSO to achieve a concentration of 10 mmol/L. This solution was stored at -20 °C. For cell treatment, the solution was further diluted in culture medium to a final concentration of 30 μM.

Construction of monoclonal genetically modified cell lines. We utilized overexpression lentiviral vectors to add fluorescent signals to the target protein for visualization imaging (*7*), RNA interference (*8-12*), and of target proteins (*13*). The lentiviral vectors used in this study were constructed and synthesized by GeneChem (https://www.genechem.com.cn/about.html). We packaged the synthesized vectors into lentivirus. The GeneChem lentiviral system consists of the GV lentiviral vector series, pHelper 1.0, and pHelper 2.0 plasmids. After mixing the plasmids, we performed transient transfection into HEK293T cells using the E-trans DNA transfection reagent (GeneChem, 10038555). Following gentle mixing, the cells were incubated for 48 hours, and the

supernatant was collected. Lentivirus was purified using the GeneChem lentiviral particle purification kit and stored at -80 °C. The day before infection, cells were counted and approximately 10,000 cells were seeded in a 12-well plate. After overnight culture, the virus was diluted in serum-free medium and added to the plate to infect the cells at a recommended MOI. After 12 hours, the virus-containing solution was removed, and a complete medium was added for cell culture. After 48 hours, fluorescence intensity was observed under a fluorescence microscope. Corresponding antibiotics were added for cell selection, and monoclones were picked for subsequent experiments. Five stable cell lines are constructed for this study: HEK293T-LifeAct-H2B to visualize F-actin and H2B, HEK293T-FUCCI to visualize cell cycle, HEK293T-DSG2^{OE} to overexpress DSG2, HEK293T-DSG2^{RNAi} to knockdown DSG2, and HEK293T-ITGB3^{RNAi} to knockdown ITGB3. More details about the construction procedure and characteristics of the cell lines are offered in the **Supplementary Information**.

Immunostaining Experiments. For the samples in 3D, the culture medium was aspirated, and the samples were-washed with PBS. They were then fixed at room temperature with 0.4 % glutaraldehyde (National Medicines, 30092436) for 15 minutes, followed by another wash with PBS. Next, the samples were treated with 0.1 % sodium borohydride (Kemiou, 80115818KMO) at 4 °C for one hour to eliminate the effects of glutaraldehyde on imaging. After washing with PBS again, the samples were permeabilized at room temperature with 0.1 % Triton X-100 (Solarbio, T8200-500ml) for 30 minutes. They were then blocked at room temperature for 2 hours using a solution of 3% BSA (Pumeike, PMK0181-250g) prepared in 0.1 % Triton X-100. The samples were incubated overnight at 4°C in the dark with Alexa Fluor™ 488 phalloidin (Thermo Fisher, A12379) diluted 2000-fold in 3 % BSA for actin (*14*). The p53 primary antibody (Abcam, catalog no. ab26) was diluted 500-fold with 3 % BSA. The diluted antibody was incubated with the 3D samples overnight at 4 °C. On the following day, the p53 antibody was removed, and the samples were washed three times with PBS, each wash lasting 10 minutes. The Goat anti-Mouse IgG (H+L) secondary antibody was then diluted 1000-fold in 3% BSA and incubated with the samples for 4 hours at room temperature in the dark. Finally, the samples were washed three times with PBS, each wash lasting 10 minutes (*15, 16*). After washing twice with PBS, Hoechst 33258 (Pumei Biological, PMK0965) was added for a 30-minute incubation at room temperature to stain the DNA (*17*). For the samples in 2D, the culture medium was aspirated and washed once with PBS. They were then fixed at room temperature with 4% paraformaldehyde (Pumei Biological, PMK2040) for 15 minutes, followed by another wash with PBS. The samples were permeabilized at room temperature with 0.5% Triton X-100 (Solarbio, T8200-500ml) for 10 minutes and then washed again with PBS. Next, a blocking solution of 3% BSA (Pumei Biological, PMK0181-250g) prepared in PBS was applied for 1 hour at room temperature. The samples were then incubated overnight at 4 °C in the dark with Alexa Fluor™ 488 phalloidin (Thermo Fisher, A12379), diluted 2000-fold in 3 % BSA. After washing twice with PBS, an anti-fade mounting medium containing DAPI (Pumei Biological, PMK0272) was added, and the samples were incubated at room temperature for 15 minutes before imaging.

Live cell dye staining experiments. SiR-actin (CY-SC001, Cytoskeleton) is a fluorescent probe based on Silicon Rhodamine (SiR) conjugated with the actin-binding natural product Jasplakinolide. This combination enables specific and low-background labeling of F-actin in live

cells (*18*). Hoechst 33258 was diluted 1000-fold in culture medium and incubated at 37 °C for 1 hour (*17*). A 1 mM SiR-actin or Hoechst 33258 stock solution was prepared in anhydrous DMSO or PBS and stored at -20 °C. For labeling, 3D-cultured cancer cell spheroids were collected, and the SiR-actin or Hoechst 33258 stock solution was diluted to 500 nM in culture medium. The cells were then incubated at 37 °C with 5 % CO_2 for 1 hour, with the incubation time adjustable based on the staining outcome. For cell lines with high levels of efflux pump expression, the addition of 10 μM Verapamil to the staining solution may improve the staining quality. After incubation, imaging was performed using a live-cell workstation with a spinning-disk confocal microscope. The laser wavelength was set to 640 nm (100 mW) with 20 % laser intensity and an exposure time of 200 ms.

Live cell imaging. For 3D imaging, we established a live cell imaging platform by integrating a 3-gas controller (Oko-lab, 3GF-MIXER-HYPOXIA) and a temperature incubator (Oko-lab, H301-MINI) onto a spinning disk confocal microscope (SpinSR, Evident Olympus). The microscope incubators maintain a temperature of 37°C for live cell culture, while the gas controller regulates the flow rates of air, carbon dioxide, and nitrogen to maintain a carbon dioxide concentration of 5% and an oxygen concentration of either 21% or 2%, depending on experimental requirements. Cell samples in confocal dish (Nest, 801001) were placed on the live cell workstation. Typically, we set the laser intensity to 20% and the exposure time to 200 ms. To capture the dynamics of tumor spheroids, we utilized a laser with a wavelength of 488 nm to image the cytoskeleton and a laser with a wavelength of 561 nm to image the nuclei. To capture cell cycle , the 488 nm laser was used to image nuclei in the S/G2/M phases, while the 561 nm laser was employed to image nuclei in the G1 phase (*19*). To enhance experimental throughput, we selected a quad-well confocal dish (Cellvis, D35C4-20-1.5-N) for imaging, where each well operates independently without interference. Typically, three imaging positions are chosen within each well. When imaging 3D samples, at each position, a total 60 μm range along the z-axis was scanned at an interval of 5 μm, resulting in a total number of 15 images for one stack. When imaging 2D samples, images are captured at each position along the Z-axis at 3 μm intervals, resulting in a total of 7 images for one stack and a total z-range of 18 μm. The super-resolution images are obtained under the corresponding mode of the spinning disk confocal microscopy, using a 60x objective. Images were captured every hour for a total duration of 42 hours, with no significant phototoxicity observed (*20-22*).

Scanning electron microscopy. Cells were seeded in Matrigel and cultured under either 21% or 2% oxygen for 48 hours. After collection, the samples were washed once with PBS and fixed with 0.4% glutaraldehyde (National Medicines, 30092436) at room temperature for 15 minutes, which preserved both the spheroid morphology and the Matrigel network structure. Subsequently, the samples were processed for electron microscopy. They were immersed in a mixture containing 2% paraformaldehyde (PFA) and 2.5% glutaraldehyde at 4°C overnight, followed by three washes with 0.1 M cacodylate/PB buffer (pH 7.4) at 4°C for 10 minutes each. Post-fixation was performed with 2% osmium tetroxide and 1.5% potassium ferrocyanide on ice for 1 hour. The samples were

then rinsed with 0.1 M cacodylate/PB buffer on ice for 30 minutes, and washed three times with ice-cold ddH_2O for 5 minutes each. This was followed by treatment with 1% thiocarbohydrazide (TCH) at 40°C in the dark for 30 minutes, and subsequent washing with ice-cold ddH_2O three times for 10 minutes each. The samples were then treated with 2% osmium tetroxide on ice for 1 hour, washed four times with ice-cold ddH_2O for 10 minutes each, and stained with 1% uranyl acetate (UA) in ddH_2O at 4°C overnight. After warming at 50°C for 2 hours, the samples were washed four times with ice-cold ddH_2O for 10 minutes each, treated with lead aspartate at 60°C for 1 hour, and again washed four times with ice-cold ddH_2O for 10 minutes each. Dehydration was carried out using a graded ethanol series, followed by two rinses with 100% acetone for 20 minutes each at room temperature. Finally, the samples were embedded in resin for further processing.

Resin-embedded tumor spheroids was mounted onto an aluminum pin and trimmed to a cubic shape using an ultramicrotome (Leica UC7) until the tissue was exposed. Samples were subsequently coated with a 40-nm platinum layer using a high-vacuum sputter coater (Leica EM ACE600). The aluminum pin was then transferred to a Gatan 3View2 system within a serial block-face scanning electron microscope (SBF-SEM, Zeiss Gemini 300). Samples imaging was performed at an acceleration voltage of 1.5 kV with a 30μm aperture and a dwell time of 1 μs. Images were acquired at a resolution of 11,000× 11,000 pixels (5-nm pixel size), with serial sectioning at 70nm z-intervals.

Laser ablation experiments. To assess the mechanical property of tumor spheres, we employed a high-power laser to ablate individual cells within the tumor spheroids and monitored the response (*23*). Tumor spheroids cultured were first placed under a confocal microscope. Before laser ablation, ensure that tumor spheroids in different samples were at comparable z0 heights and had similar sizes. The intensity of the 405 nm laser was set to 100 % (50 mW), with a duration of 10 seconds for each ablation. A single cell at the edge of the tumor sphere was randomly selected for ablation. After laser exposure 4-5 times, the selected cell was ablated. During the ablation process, real-time imaging of the actin was conducted using a 488 nm laser, allowing for simultaneous live cell recording. Subsequent analysis focused on the deformation of the tumor spheroids over time.

Nano-identation measurements. The nano-indentation instrument (PIUMA Chiaro) can characterize the Young's modulus of cell surfaces with high precision without deconstructing the cells (*24*). We measured the Young's modulus of cell surfaces under both hypoxia and normoxia conditions. The sample preparation method was identical to that used for two-dimensional live-cell imaging. The confocal dish was placed under the microscope when the cell density reached approximately 70-80 %. We first observe the sample under the objective, placing the interested cell at the center of view field. Then a nanoindentation probe with the size of 2 μm is lowered onto the cell surface, giving feedback to the *in situ* force it senses. Nine random locations were selected on each confocal dish for measurement with the same nanoindentation probe.

Quantification and statistical analysis

Data reconstruction and 3D visualization. The reconstruction of imaging stacks from confocal microscopy is conducted using Cell Sens Dimension Desktop 4.2.1(https://lifescience.evidentscientific.com.cn/en/software/cellsens/). In the top planer view, the Maximum Intensity Projection (MIP) algorithm is adopted to overlay all images in the z-stack into a single image. In the side view, the Marching Cubes (Surface Reconstruction Algorithms) algorithm is used to yield the stereoscopic spheroids.

Analysis of live cell imaging data. To analyze the spheroid, we segmented the tumor spheroids using CellPose (*25*), which provided the mask file of the spheroids. XY coordinates of each point on the spheroid's edge are then calculated based on the mask data. Subsequently, using the segmentation data, we employed custom-written MATLAB code to analyze dynamic parameters, including area, perimeter, circularity, movement direction, and size of the tumor spheroids. Time-series image stacks were imported into ImageJ. The Tracking Plugin Manual Tracking (*26*) was utilized to obtain the movement trajectories, centroid spatial coordinates, distance, and speed of the tumor spheroids. To give a closer look into cells, we first segment the cells for one imaging using CellPose 2.0 (*27*), determining the optimal input parameters. Then, we utilized home-built Python code to perform batch segmentation for a series of image stacks. Once the batch-processed data were obtained, we re-imported them into CellPose for fine-tuning for segmentation parameters and obtaining the mask data of the cells. After acquiring the cell edge coordinates from the mask data, we employed home-built MATLAB scripts to analyze various properties of the cells, including centroid coordinates, area, roundness, fluorescence intensity, motility, and direction. Subsequently, statistical analysis and visualization were performed using OriginLab and ImageJ, respectively.

Transcriptome sequencing and analysis. The tumor spheroids cultured in three dimensions are embedded in the matrix gel and cannot be separated individually. Therefore, when extracting RNA from these three-dimensional tumor spheres, we directly added Trizol into the matrix gel containing the tumor spheroid for extraction (*28*). In contrast, cells cultured in two dimensions can be lysed directly using Trizol. After culturing cancer cell spheroids under normoxia or hypoxia conditions for 42 hours, the culture medium was aspirated, and TransZol (TransGen, ET101-01-V2) was added directly to the mixture containing matrix gel and cells. RNA was then extracted and purified using the EasyPure® RNA Kit (TransGen, ER501-01-V2). The purified RNA was sent to Beijing Genomics Institution for library construction and sequencing, yielding sequencing data (*29*). We subsequently utilized R packages and Galaxy (https://usegalaxy.cn/) to align the sequencing data with human genomic information. To elucidate patterns and regulatory mechanisms of gene expression, regular analyses have been conducted, including sequence alignment, gene expression quantification, and differential expression analysis, Furthermore, we conducted GO and KEGG enrichment analyses of differentially expressed genes to gain deeper insights into the molecular mechanisms and regulatory networks underlying biological processes.

Supplementary Text

Construction and characterization of cell lines.

To achieve the visualization of target proteins and validate their related functions, we modified cell lines at the genetic level using lentiviral vector infection (*7, 30*), the procedure and outcome of which are summarized in this section (**Figures S1 and S2**). This included randomly inserting a green fluorescent Lifeact into the genome, which expresses green fluorescence and binds to F-actin in cells, thereby enabling visualization of cellular F-actin. Additionally, we achieved visualization of the nucleus by inserting the chimera gene with H2B and a red fluorescent, mCherry, into the genome (We visualized the cell nuclei by infecting cells with lentiviral vectors expressing exogenous H2B and red fluorescence). For the overexpression of DSG2 and ITGB3, we introduced these genes as exogenous genes through random insertion, utilizing a broad-spectrum promoter. As a result, the mRNA levels of the target genes in the overexpressing cell lines were upregulated by at least 100-fold (**Figures S2A-S2D**). For RNA interference (RNAi) targeting DSG2 and ITGB3, we randomly inserted shRNA specific to the target proteins into the genome, facilitating continuous production of RNAi against the target genes. Consequently, the mRNA levels of the target genes in the RNAi cell lines were downregulated by at least 70 % (**Figures S2O and S2P**).

The lentiviral vector used in this study was commercially constructed and synthesized (GeneChem Ltd, Shanghai). We packaged the synthesized vector into lentivirus. The lentiviral system consists of the GV lentiviral vector series, pHelper 1.0, and pHelper 2.0 plasmids. The GV lentiviral vector serves as the core of the viral genome and contains essential components of HIV, including the 5' LTR and 3' LTR, as well as viral packaging signals and other auxiliary elements such as the woodchuck hepatitis virus posttranscriptional regulatory element (WPRE). The GV vector can be modified according to specific experimental objectives to insert target genes or fragments for gene function studies (*31, 32*). The pHelper 1.0 vector is an auxiliary plasmid that contains the gag gene, which encodes the major structural protein of the virus; the pol gene, which encodes virus-specific enzymes; and the rev gene, which encodes a regulatory factor that modulates the expression of the gag and pol genes. The pHelper 2.0 vector, also an auxiliary plasmid, contains the VSV-G gene derived from the herpes simplex virus, providing the envelope protein necessary for viral packaging (*33, 34*). Linearized vectors were obtained through restriction enzyme digestion, and target gene fragments were prepared via PCR amplification. The amplification primers were designed to add homologous recombination sequences at their 5' ends, ensuring that the sequences at the 5' and 3' ends of the amplified product matched those of the linearized cloning vector. The reaction system was set up using the linearized vector and the amplified target gene product for the recombination reaction, achieving in vitro circularization of the linearized vector and target gene fragment. The recombinant products were directly transformed, and single clones from the plates were screened through PCR identification. Positive clones were sequenced and analyzed.

Correctly cloned bacterial cultures were expanded, and plasmids were extracted to obtain high-purity plasmids for downstream virus packaging (*34*).

HEK293T cells were seeded in 10 cm culture dishes and incubated in a serum-free medium for 1 hour when the cell density reached approximately 70-80 % in preparation for virus packaging. The constructed plasmid, along with pHelper 1.0 and pHelper 2.0 plasmids, was mixed with serum-free medium and E-trans DNA transfection reagent (GeneChem, 10038555) and incubated at room temperature for 15 minutes. This mixture was then added to the cells, and supernatants were collected every 24 hours. The collected supernatants containing lentivirus were purified using Lenti-X™ Concentrator (PT4421-2). Specifically, 500 g of the viral suspension was centrifuged for 10 minutes, and the clarified supernatant was transferred to a sterile container. One volume of viral purification reagent was mixed with three volumes of the clarified supernatant. The mixture was gently inverted and incubated overnight at 4 °C. Following this, the mixture was centrifuged at 1500 g for 45 minutes at 4 °C, and the supernatant was carefully discarded. The viral pellet was resuspended in 1-2 mL of sterile PBS and stored at -80 °C.

On the day before infection, healthy cells were digested and seeded in 24-well plates, aiming for a cell density of approximately 20 % after 24 hours. Typically, 500 µL of viral solution was mixed with 500 µL of culture medium and subsequently added to the cells. After 12 hours of viral infection, the viral-containing medium was removed and replaced with a serum-containing medium for continued culture. Forty-eight hours later, fluorescence expression was observed under a microscope. Monoclonal cell lines were established for the purpose of avoiding genetic heterogeneity and ensuring a substantial strength of the fluorescence signals. To do this, we continued the cultivation in Petri dishes by adding an appropriate dose of culture medium containing specific antibiotics. The HEK293T-LifeAct cell line was selected using a medium containing G418, while the HEK293T-H2B and HEK293T-FUCCI cell lines were selected using medium containing puromycin. The HEK293T-DSG2 cell line was selected with a medium containing puromycin, and the HEK293T-ITGB3 cell line was selected with a medium containing puromycin. The HEK293T-DSG2 RNAi cell line was selected using a medium containing blasticidin, and the HEK293T-ITGB3 RNAi cell line was selected with a medium containing puromycin. Typically, the culture medium was replaced every two days until no significant cell death was observed. Subsequently, the cells were digested with trypsin to prepare a cell suspension, which was then diluted to an appropriate concentration and seeded into a 96-well plate, ensuring that only one cell was seeded per well. After 24 hours, once the cells had adhered, fluorescence signals were observed again using a confocal microscope. Cells exhibiting positive fluorescence signals were selected for further cultivation. When the cells approached confluence, they were digested with trypsin and reseeded into a 24-well plate for continued culture until a large number of monoclonal cells were obtained for preservation and experimentation. Throughout the entire process of monoclonal cell expansion, culture was performed using media containing lower concentrations of the corresponding antibiotics than those used during selection, until a substantial number of monoclonal cells were achieved (**Figures S2I-S2T**).

All cell culture and manipulations of cell lines (*35*) are conducted in a cell room that satisfies ISO 7 in the ISO 14644-1 system or Class 10,000 in the FS 209E system. The mycoplasma test (*36*) was done every week and no positive result has been reported.

We verified the accuracy of the recombinant plasmid using PCR gel electrophoresis and assessed the mRNA expression of the target gene in the constructed cell lines via qPCR (**Figures S2A-S2H)**. All primers used for qPCR are listed in **Table S1**. Additionally, we confirmed the localization of the target protein in the cells through confocal microscopy.

The stable cell lines used in this study are summarized in **Table S2**, and we provide in this paragraph a detailed description of their nomenclature, characteristics, and excitation wavelength, etc. To enable dynamic visualization of the cellular processes, we constructed HEK293T cells expressing LifeAct-EGFP and H2B-mCherry (HEK293T-LifeAct-H2B). LifeAct is a small peptide that specifically binds to F-actin, thereby labeling the actin structures. This binding makes LifeAct an important tool for studying cytoskeletal dynamics. By fusing LifeAct with enhanced green fluorescent protein (EGFP), we can visualize actin filaments. The primary excitation wavelength for EGFP is approximately 488 to 490 nm. The mCherry fluorescent protein is fused with the histone H2B to enable visualization of chromatin. The primary excitation wavelength for mCherry is around 550 to 563 nm. To investigate cell cycle dynamics, we constructed HEK293T cell lines that express the FUCCI system (HEK293T-FUCCI), a dual-color fluorescent probe. This system combines mKO2 (red) and mAG (green) fluorescent proteins with two cell cycle-dependent proteins—Cdt1 and Geminin—allowing us to indicate whether individual live cells are in the G1 phase or the S/G2/M phase. The excitation wavelength for the red fluorescent protein mKO2 is typically around 530 to 550 nm, while the excitation wavelength for the green fluorescent protein mAG is approximately 488 to 495 nm. To investigate the role of intercellular communications and the cell-ECM interaction, we constructed different cell lines that overexpress DSG2 and ITGB3, or reduce their expression through RNA interference. For the overexpression of DSG2(HEK293T-DSG2^{OE}), we built a vector that fuses DSG2 with mCherry and integrated it into the HEK293T genome, thereby simultaneously enhancing DSG2 expression and enabling its visualization. The overexpression strategy for ITGB3 (HEK293T-ITGB3^{OE}) was similar to that of DSG2. For the reduction of DSG2 expression (HEK293T-DSG2^{RNAi}), we constructed a separate cell line that expresses shRNA fused with EBFP targeting DSG2. After being integrated into the HEK293T genome, the sustained expression of the interfering RNA results in decreased DSG2 levels. The method used to lower ITGB3 expression (HEK293T-ITGB3^{RNAi}) was analogous to that employed for DSG2.

<u>Porous ECM gel for 3D culture.</u>

The porous ECM structure formed from the Matrigel provides the 3-dimensional microenvironment for the tumor cell to survive and proliferate (**Figures S3A and S3B**). This method has been widely used to reproduce 3D cellular processes *in vitro*, including organoid

culture, internal angiogenesis experiments, and tumor growth in nude mice (*37-39*). To elucidate the microenvironment of the tumor spheroid, we directly image the ECM structure by bright field and confocal microscopy. Empty porous with 20-40 μm size are homogeneously distributed throughout a 3D Matrigel network (**Figure S3**). The size of the porous is much larger compared to that of a typical tumor spheroid, offering sufficient space for the spheroid to move and grow. So any confinement force from the ECM can be excluded. In other words, the ECM serves as a gentle strut for the 3D culture but affects little on the spheroid behavior.

Here we provide more details of fabricating the ECM structure with the appropriate porous size. Mix the Matrigel and DMEM basal medium in a 1:1 ratio and place the mixture on ice. For a 35 mm confocal dish, add approximately 80 μL of the prepared Matrigel; for a four-well confocal dish, add 20 μL of Matrigel to the bottom of each well. Use a pre-chilled 10 μL sterile pipette tip to spread the Matrigel evenly. The amount of Matrigel applied should be appropriate; too much may reduce imaging depth, while too little can lead to cell adhesion without spheroid formation. After using the Matrigel, place the confocal dish at 37 °C for approximately 10 minutes to allow it to solidify. Next, aspirate the cell culture medium and wash the cells twice with PBS, reserving 1 mL of PBS. Add 0.5 mL of 0.25 % trypsin to digest the cells. When the cells round up and begin to detach, add 1 mL of serum-containing medium to terminate digestion. Gently pipette to create a homogeneous cell suspension, transfer the suspension to a centrifuge tube, and centrifuge at 1400 rpm for 5 minutes. Resuspend the cells in the prepared Matrigel solution and add them to the confocal dish containing the Matrigel. Incubate at 37 °C for 10 minutes to allow solidification. Finally, add DMEM medium containing 10 % serum and incubate at 37 °C with 5 % CO_2.

<u>Cell segmentation, imaging reconstruction, and data analysis.</u>

In this section, we provide more information about imaging and data analysis. To obtain the morphology and dynamics of each cell, the outcome image (**Figures S3C**) of the overlay from CellSens software was imported into CellPose *(25, 27)*, where parameters were adjusted to segment the cells. For cell segmentation using CellPose, the "cell diameter" parameter in the segmentation settings was first adjusted according to the size of the cells to be identified. The appropriate fluorescence signal channel for segmentation was then selected, with other parameters left at their default values. Pre-configured segmentation models in CellPose, such as "cyto," "cyto2," and "nuclei," were tested to assess their segmentation performance. The model yielding the best results was chosen for further processing using custom-written Python code for batch processing. The segmentation results were subsequently re-input into CellPose for validation, and any misclassified data were manually corrected. Incorrectly segmented image data can be corrected by re-importing the data into CellPose, where errors can be removed using Ctrl + left-click. The correct cell boundaries are then manually outlined, and the corrected data are saved. All data underwent manual correction to accurately capture the boundary information of each cell (**Figures S3D**). The segmentation of the 3D spheroid follows the same procedure as that of the 2D cell segmentation.

During the three-dimensional imaging of tumor spheroids, the full imaging depth of the microscope can reach 200 µm. A field of view in xy plane is 245 µm by 245 µm under 60x oil objective. Using the motorized sample stage, more than ten field of view are recorded simultaneously. The typical diameter of a tumor spheroid after 48 hour hypoxia treatment is 37.024 µm. So the throughput of our experiment can reach more than eighty spheroids per trial. Typically, we acquired video data at 3 µm per layer along the z-axis, resulting in totally 21 layers with an overall z-axis height of 60 µm. Consequently, for analyzing the three-dimensional movement trajectories of the tumor spheroids, we utilized the maximum projection data obtained by stacking the 21 z-axis layers. This method applies for all confocal images presented main text and extended data figures. Another way of 3D reconstruction is to use surface reconstruction algorithms, giving out the side view of the spheroid (**Figure S3E**). The side view reconstruction appears to have compromised spatial resolution compared with the top-down view because of the resolution inconsistency of confocal imaging method in xy plane (200 nm) and z scanning (450 nm).

After segmentation using CellPose, the spatial coordinates of the boundaries and inner area of the ROI (Region of Interest) will be obtained, including the brightness of each pixel in the ROI. The ROI could be either spheroid or cells, depending on the object we are looking into. For analyzing the movement speed and distance of the tumor spheroids, we employed the "Manual Tracking" plugin from ImageJ (*26*). After setting the appropriate time interval and pixel size, we manually marked the movement trajectories of the tumor spheroids. The more dedicate kinetic analysis was performed using a custom-written MATLAB code. Let the function (I(x, y)) represent the intensity or grayscale values at all positions within the segmented boundary. If (R) is a discrete region, then for each pixel location, the value is typically set to 1 (indicating that we are essentially counting the number of pixels). Thus, (A) can be understood as the total number of pixels within the region (R). The area (A) can be expressed as follows:

$$\boldsymbol{A = \sum_{(x,y)\in R} I(x,y)} \quad \ldots\ldots\ldots\ldots\ldots\ldots\ldots\ldots\ldots \quad \textbf{Eq.S1}$$

The centroid (C_x, C_y) can be calculated using the following formula:

$$\boldsymbol{C_x = \frac{1}{A}\sum_{(x,y)} x \times I(x,y)} \quad \ldots\ldots\ldots\ldots\ldots\ldots\ldots\ldots\ldots \quad \textbf{Eq.S2}$$

$$\boldsymbol{C_y = \frac{1}{A}\sum_{(x,y)} y \times I(x,y)} \quad \ldots\ldots\ldots\ldots\ldots\ldots\ldots\ldots\ldots \quad \textbf{Eq.S3}$$

The perimeter of the ROI (Region of Interest) is denoted as:

$$\boldsymbol{P = \sum_{(x,y)\in B} I(x,y)} \quad \ldots\ldots\ldots\ldots\ldots\ldots\ldots\ldots \quad \textbf{Eq.S4}$$

$(x, y) \in B$ represents the summation of all pixel coordinates within the boundary B.

The roundness of the ROI (Region of Interest) is defined as:

$$\boldsymbol{C = \frac{4\pi A}{P^2}} \quad \ldots\ldots\ldots\ldots\ldots\ldots\ldots\ldots\ldots \quad \textbf{Eq.S5}$$

where A is the area and P is the perimeter.

Velocity can be calculated by measuring the displacement over a unit time interval. The displacements in the x-direction and y-direction within that unit time are denoted as $\boldsymbol{\Delta X}$ and$\boldsymbol{\Delta Y}$, respectively.

$$\boldsymbol{\Delta x = x_t - x_{t-1}} \quad \ldots\ldots\ldots\ldots\ldots\ldots\ldots\ldots\ldots \quad \textbf{Eq.S6}$$

$$\boldsymbol{\Delta y = y_t - y_{t-1}} \quad \ldots\ldots\ldots\ldots\ldots\ldots\ldots\ldots\ldots \quad \textbf{Eq.S7}$$

Therefore, the velocity (v) can be expressed as:

$$\boldsymbol{v = \sqrt{\Delta x^2 + \Delta y^2}} \quad \ldots\ldots\ldots\ldots\ldots\ldots\ldots\ldots \quad \textbf{Eq.S8}$$

To calculate the direction of motion of the tumor sphere, we first compute the vector difference between the positions at two adjacent time points. This is expressed as:

$$\boldsymbol{\vec{B} = (x - x_{P1}, y_{P2} - y_{P1})} \quad \ldots\ldots\ldots\ldots\ldots\ldots\ldots\ldots\ldots \quad \textbf{Eq.S9}$$

Let A be the velocity vector and B be the displacement vector. The cosine of the angle between the two vectors can be expressed as:

$$\boldsymbol{\cos\theta = \frac{A \times B}{|A| \times |B|}} \quad \ldots\ldots\ldots\ldots\ldots\ldots\ldots\ldots\ldots\ldots \quad \textbf{Eq.S10}$$

The projection of the velocity vector onto the direction of the displacement vector can be expressed as:

$$\boldsymbol{projection = |A| \cos(\theta)} \quad \ldots\ldots\ldots\ldots\ldots\ldots\ldots\ldots\ldots \quad \textbf{Eq.S11}$$

<u>Verification and analysis of transcriptomic data.</u>

To conduct the transcriptomic analysis, we extract the RNA from the cells. First, we implanted cancer cells into a three-dimensional (3D) culture system. Then, the 3D-cultured cancer cells were placed in an incubator set at 37 ℃ with 5% CO_2 and 21% O_2, or in a hypoxic incubator at 37 ℃ with 5% CO_2 and 2% O_2, depending on the experimental requirements, for 12 to 48 hours. After the treatment period, the culture dishes containing the cells were removed, the culture medium was aspirated, and the cells were washed once with PBS. RNA extraction was performed using the TransZol Up Plus RNA Kit (ER501-01-V2). The microcentrifuge tubes were removed from the -80 ℃ freezer and placed on ice until thawed. After thawing, 200 μL of RNA Extraction Agent, TransZol, was added into each 3.5 cm culture dishes for cell cultivation, and the sample was pipetted repeatedly until no visible precipitate remained in the lysate. The mixture was vortexed at room temperature for 5 minutes and then centrifuged at 10,000 g for 15 minutes at 4 ℃. At this

stage, the sample separated into three layers: a colorless aqueous phase (top layer), a middle layer, and a pink organic phase (bottom layer). The RNA is located in the aqueous phase. The colorless aqueous phase (400 µL) was carefully transferred to a new centrifuge tube, and an equal volume of anhydrous ethanol was added. The solution was gently mixed by inverting the tube. The mixture, including any precipitate, was then transferred to a spin column and centrifuged at 12,000 g at room temperature for 30 seconds. The flow-through was discarded, and 500 µL of CB9 buffer was added. The sample was centrifuged at 12,000 g at room temperature for 30 seconds, and the flow-through was discarded. This step was repeated once. Then, 500 µL of WB9 buffer was added, and the sample was centrifuged at 12,000 g at room temperature for 30 seconds. The flow-through was discarded, and the washing step was repeated once more. Finally, the sample was centrifuged at 12,000 g for 2 minutes to completely remove any residual ethanol. The spin column was transferred into an RNase-free tube, and 40 µL of RNase-free water was added to the center of the column. The column was incubated at room temperature for 1 minute, followed by centrifugation at 12,000 g for 1 minute to elute the RNA. The extracted RNA was stored at -80 ℃.

The prepared RNA samples used in transcriptome sequencing were delivered to BGI Genomics for sequencing. The purity and integrity of the RNA were assessed through agarose gel electrophoresis in our laboratory before submitting the samples for further quality checks by the company. After passing the double-check procedures, the sequencing started. The library construction and sequencing process includes the following steps First, the mRNA is extracted using oligo-Dt and the total amount of it is quantified. Then, the mRNA chain is fragmented by chemical method. The use of metal ions, such as zinc ions, can catalyze the cleavage of phosphodiester bonds within RNA molecules, thereby fragmenting the RNA into smaller segments. Random primers are added for the synthesis of single-stranded cDNA from the fragmented mRNA. With the synthesized double-stranded cDNA, a ploy-A tail and ligation of adapters were used for the end repair. The prepared cDNA further underwent PCR amplification, quality assessment, and circularization to establish the library. The circular DNA molecules were rolled up to generate DNA nanoballs (DNBs). Finally, the DNBs were sequenced on the DNBSEQ platform.

After sequencing, the raw data undergoes filtering to remove contaminants, adapters, and low-quality data. Some raw sequences may contain adapter sequences or a small number of low-quality bases. We perform a series of data processing steps to eliminate impurities and obtain high-quality data. This analysis is conducted using SOAPnuke (*48*), a filtering software developed by BGI. The filtering parameters for SOAPnuke are set as follows: "-n 0.001 -l 20 -q 0.4 --adaMR 0.25 --polyX 50 --minReadLen 150." The filtering steps are described as follows. An adapter filtering was conducted to discard any sequencing read matching an adapter sequence at 25.0 % or more (allowing for a maximum of two mismatches). Read length filtering then removed reads shorter than 150 bp. Removal of N bases discard reads that contain 0.1% or more N bases. PolyX filtering deletes reads with a polyX length (where X can be A, T, G, or C) exceeding 50 bp. If the proportion of bases with a quality score below 20 exceeds 40.0 %, the low-quality data filtering removes the entire read. Finally, the output reads are assigned quality values based on the Phred+33 scale. Following the filtering of the raw data, we monitor data quality to ensure the integrity of the sequencing results (**Figure S3F**).

To support opinions in the corresponding parts of the main text, we provide here a more detailed analysis of the transcriptomic data. Transcriptomic data show substantial differences in the gene expression pattern between the HEK293T cells in 3-dimensional and 2-dimensional cultures. In 3D, a significant number of genes that control cancer stemness are upregulated (**Table S3**). For example, we found SAGE1 (Squamous Aggressive Growth Enhancer 1) is upregulated by 53.43 fold under hypoxia conditions. SAGE1 is upregulated in various squamous cell carcinomas and is therefore considered a potential diagnostic or prognostic biomarker for assessing disease progression and patient treatment response. Studies have suggested that SAGE1 may promote tumor growth and development by modulating cell cycle regulation, enhancing cell proliferation, and inhibiting apoptosis. Additionally, SAGE1 has been implicated in increasing the invasiveness and migratory capacity of cancer cells, thereby facilitating distant metastasis (*49, 50*). In terms of mechanics, the differences between 3D and 2D cultures are complex. The genes that are relevant to the cell-cell adhesion and cell-ECM interaction do not exhibit collective upregulation or downregulation. For example, although CDH18, CDH11, and DSG2 are all responsible for cell-cell adhesion (*51-54*), their gene expression shows very different trends of upregulation, downregulation, and no change, respectively, in 3D culture (**Table S3**). Therefore, it is difficult to judge from the transcriptomic data whether the cell-cell adhesion changes in 3D culture. The same situation is for the genes that control cell-substrate interaction. These data suggest the major difference between 3D and 2D culture lies in the cancer stemness. Compared with the growth in adherence with the substrate, the anchorage-independent environment in 3D culture makes the genetic expression of the HEK293T cells closer to that of tumor cells.

When comparing the gene expression between hypoxia and normoxia conditions in 3D culture, the changes in the mechanics are more prominent (**Table S4**). Genes responsible for actin polymerization exhibit collective upregulation and those for cell-cell adhesion in general are downregulated. The expression of both INTB1 and INTB3 exhibits no significant change. All these sequencing outcomes are consistent with the PHAi, RNAi, and OE experiments reported in the main text. Besides cell mechanics, our transcriptomic data underwent Gene Ontology (GO) enrichment analysis, with Biological Process results showing significant enrichment of genes involved in extracellular matrix (ECM) organization and canonical glycolysis, which suggest the involvement of extracellular matrix remodeling and metabolism (**Table S4**). ECM organization refers to processes involving the assembly, maintenance, and remodeling of the extracellular matrix, a complex network of proteins and polysaccharides secreted by cells (*55, 56*). ECM is crucial for cellular functions such as morphology, differentiation, migration, and signal transduction (*57*). It provides physical support and protection to cells and helps maintain tissue structural integrity (*58*). Components of the ECM serve as carriers of signaling molecules, facilitating intercellular communication. The structure and composition of the ECM influence cellular migration and are vital for processes such as embryonic development (*59, 60*), wound healing (*61-63*), and cancer metastasis (*56, 64*). Furthermore, ECM interacts with cell surface receptors to regulate differentiation and cell fate. Canonical glycolysis refers to the classic glycolytic pathway (*65, 66*), in which glucose is broken down into pyruvate. Glycolysis is one of the primary mechanisms for ATP production in cells, particularly under hypoxic conditions (*65,*

67). This pathway is critical for cell survival and proliferation, especially in rapidly proliferating cells, such as cancer cells (*68, 69*).

Under hypoxic conditions, the upregulation of genes associated with these processes indicates that cancer cells are actively involved in tumor microenvironment remodeling (*70*). Cancer cells actively utilize and alter their surrounding environment to promote tumor progression, fostering an environment conducive to tumor formation (*71-73*). Moreover, glycolysis is a fundamental metabolic process, particularly in cancer cells, where its aberrant activation and dysregulation play a critical role in tumor initiation, progression, and metastasis. Tumor cells are often in a state of rapid proliferation, resulting in an elevated energy demand (*74*). Glycolysis provides a fast means of ATP production under hypoxic conditions, thus meeting the energy needs of tumor cells. Intermediates generated during glycolysis, such as 3-phosphoglyceraldehyde and phosphoenolpyruvate, can be used for the synthesis of nucleic acids, lipids, and proteins, supporting the rapid proliferation of cancer cells (*69*). Additionally, the NADH and NADPH produced through glycolysis contribute to antioxidant defense mechanisms, protecting tumor cells from oxidative stress-induced damage (*75, 76*). In summary, under hypoxic conditions, tumor cells actively reprogram their behavior, including metabolic pathways and protein expression, to facilitate tumorigenesis and progression.

In brief, we identified enrichment in signaling pathways related to glycolysis and cell-extracellular matrix interactions. As mentioned earlier, the expression of glycolytic enzymes was significantly upregulated under hypoxic conditions, and genes related to extracellular matrix components secreted by cancer cells were also significantly upregulated. These findings are consistent with the altered energy metabolism of tumors and the remodeling of the tumor microenvironment.

Although thousands of genes are upregulated or downregulated in response to hypoxia, no existing signal pathway was identified. Some examples of classical signal pathways are summarized in Figure S13. The MAPK (Mitogen-Activated Protein Kinase) signaling pathway plays a critical role in the initiation, progression, and metastasis of cancer (*77, 78*). This pathway consists of three main branches: the ERK (Extracellular signal-Regulated Kinase) pathway, the JNK (c-Jun N-terminal Kinase) pathway, and the p38 MAPK pathway (*79-81*). These pathways regulate various biological processes such as cell proliferation, differentiation, survival, migration, and apoptosis through a series of cascade reactions (*79, 82*). Ras is one of the key initiators in the MAPK pathway, receiving signals from cell surface receptors and transmitting them to downstream Raf kinases. Our sequencing data indicate that under hypoxic conditions, Ras expression is upregulated, along with the expression of downstream genes such as c-fos, MKP, and AP1. Additionally, we observed the downregulation or no significant change in the expression of some genes. Hypoxia-inducible factor 1 (HIF-1) is a transcription factor activated under hypoxic conditions (*67, 83*). Its activation not only helps cells adapt to low-oxygen environments but also plays a role in various physiological and pathological processes, including tumor development. In our signal enrichment analysis, while the expression of HIF1α did not show a significant change, all downstream target genes of this pathway were significantly upregulated. This indicates that a series of downstream target genes and their associated activities are activated in response to hypoxia.

Time-dependent molecular analysis on the function of cancer stemness, hypoxia factor, and cell mechanics.

Early detection of cancer significantly enhances treatment efficacy and improves survival rates (*40-42*). However, over 50% of cancers are diagnosed at advanced stages. The progression of tumors follows a continuum from normal tissue to dysregulation, carcinogenesis, proliferation, differentiation, and metastasis. By the time cancer is clinically detected, cancer cells have undergone sufficient genetic and phenotypic alterations, leading to challenges such as drug resistance and recurrence. Therefore, targeted interventions during the early stages of cancer development may yield better anti-tumor outcomes.

One critical challenge in early cancer detection is the lack of research into the early biological characteristics of cancer (*40, 43*), primarily due to the difficulty in observing the first cancer cells that appear in tissues *in vivo*. We propose an *ex vivo* model to simulate the tumor microenvironment for studying early cancer biology. The HEK293T cells, when transplanted into three-week-old mice, form tumors within 14 days (*44*). Histologically, tumors formed by 293T cells are consistent with poorly differentiated breast cancer, exhibiting high expression of vimentin and β-catenin, along with low expression of E-cadherin and cytokeratin 19, which aligns with the expression profile of poorly differentiated tumors (*44*). In three-dimensional (3D) culture, 293T cells in spheroids display a higher proportion of ALDH1 positive cells and CD44+/CD24- cell populations compared to those in two-dimensional (2D) monolayer cultures, both of which are markers of cancer stem cells. The cells within the 3D spheroids exhibit radio-resistance and upregulate signaling pathways associated with stem cell survival, including the expression of β-catenin, Notch1, and Survivin under radiation exposure. Additionally, spheroid cells show increased expression of mesenchymal genes (vimentin, N-cadherin, ZEB1, Snail, and Slug) as well as pro-metastatic genes (RhoC, Tenascin C, and MTA1) (*45, 46*). Transcriptomic sequencing and qPCR results further demonstrate significant upregulation of cancer embryonic antigen-related genes SAGE1, MAGEC2, and ALDH1A (**Figure S4A, S4B and S4C**). After forming spheroid in 3D culture, the 293T cells exhibit typical cancer stem cell characteristics, including self-renewal ability, treatment resistance, and metastatic potential. This cellular model serves as a crucial tool for investigating the molecular and biological mechanisms of cancer stem cells and will aid in the development of novel therapeutic strategies targeting cancer stem cells.

Data on early tumor growth dynamics indicate that under hypoxia conditions, tumor spheroids promote fusion between each other by facilitating actin polymerization. RNA sequencing results show that genes regulating cytoskeletal dynamics are upregulated under hypoxia (**Figure 4G**). We validated the expression levels of MAP6, a key regulator of the cytoskeleton, at different time points after hypoxia using qPCR, and found that MAP6 expression levels increased following hypoxia (**Figure S4G**). We further examined the mRNA expression levels of SAGE1, an embryonic antigen-related gene, at different time points during 3D culture. The results demonstrated that SAGE1 was persistently upregulated under 3D culture conditions. The longest

time point we tested was 48 hours in 3D culture, at which time the mRNA level of SAGE1 remained more than 100 times higher compared to 2D culture (**Figure S4C**). Our findings suggest that the weakened intercellular interactions under hypoxic 3D culture conditions play a crucial role in the early oncogenic potential of cancer cells. We also measured the mRNA expression of DSG2 at different time points under hypoxic 3D culture conditions, and observed a continuous downregulation of DSG2 expression at 48 hours under hypoxia (**Figure S4H**).

Additionally, we assessed the expression of HIF1α at various time points after hypoxia, revealing dynamic changes in HIF1α mRNA expression (**Figure S4I**). The expression of HIF1α declined by almost 30 % at 6 hours and 24 hours after hypoxia treatment, in sharp contrast with previous studies in 2D systems (*47*). It is until 48 hours, the HIF1α expression shows a slight increase compared to the control group. But at this time, the active fusion and enhanced tumorigenesis have already finished. KEGG enrichment at 24 hours shows no sign of enriched HIF1α pathways either. So the time-dependent mRNA test excludes the possibility that the classical HIF1α pathway is responsible for the dynamics of the tumor spheroids.

<u>RNAi, PHAi, and OE experiments.</u>

The gene expression and pharmaceutical perturbation is a major approach we used to identify the effects of various molecular factors. We provide more details of such experiments in this section. The contents include the working principles of each perturbation method, the procedures and doses used in the experiments, and the raw outcome of the experiments.

Rho Activator II (CN03) was obtained from Cytoskeleton, provided as a grayish-white lyophilized solid. The active site of CN03 is based on the catalytic domain of the bacterial cytotoxic necrotizing factor (CNF) toxins (*3*-*5*). The catalytic domain is covalently attached to a proprietary cell penetrating moiety. CN03 activates Rho GTPase isoforms by deamidating glutamine-63, which is located in the Switch II region of these GTPases. This modification converts glutamine-63 to glutamate, which blocks intrinsic and GAP-stimulated GTPase activity, resulting in constitutively active Rho (*3*). CN03 robustly increases the level of GTP-bound RhoA within 2-4 h after addition to the culture medium. Moreover, the targeted action of this activator makes it a far more attractive tool for the study of Rho GTPase signaling than classic indirect activators (LPA) that concomitantly activate other signaling pathways (Ras, PI3K, and PLC). Each vial contains 20 μg of CN03 protein with a purity exceeding 80 %. The lyophilized protein should be stored in a desiccated state at 4 °C for no more than 6 months. For reconstitution, centrifuge at 1400 rmp for 5 min to collect the product at the bottom of the tube and resuspend each vial in 200 μl of sterile water, place on ice for 10 minutes prior to mixing, and mix by gently pipetting up and down to yield a concentration of 0.1 μg/μl. During use, the compound was diluted in a culture medium to achieve a final concentration of 2 μg/mL for cell treatment.

Y-27632 was purchased from Yeasen Biotechnology and is provided as a powder with a purity exceeding 98 %. Y-27632 is an orally bioavailable, ATP-competitive selective inhibitor of Rho-associated protein kinase (ROCK). It is a potent, cell-permeable, reversible, and selective inhibitor, with a Ki value of 140 nM for p160 ROCK (*6, 84, 85*). The powder should be aliquoted and stored at -20 °C dry environment for no more than 2 years. To prepare a stock solution, 10 mg of Y-27632 was dissolved in 312 µL of DMSO to create a 100 mmol/L solution, which was then diluted 10-fold with DMSO to achieve a concentration of 10 mmol/L. This solution was stored at -20 °C. For cell treatment, the solution was further diluted in culture medium to a final concentration of 30 µM.

Under hypoxia conditions, the tumor spheroid formation rate nearly doubled compared to normoxia conditions, resulting in larger volumes and a greater number of tumor spheroids. Analysis of live-cell imaging data revealed that tumor spheroids exhibited more complex dynamic behavior under hypoxia. The fusion frequency between tumor spheroids increased significantly, with the time required for two spheroids to fuse being markedly reduced (average fusion time under hypoxia was approximately 6.4 hours, compared to 21.1 hours under normoxia). Additionally, we observed that tumor spheroids underwent greater deformation under hypoxia conditions. Thus, we hypothesized that the increased fusion frequency under hypoxia is closely related to cytoskeleton properties that mainly involve dynamical-mechanical coupling. To validate the hypothesis above, we employed PHAi, RNAi, and OE experiments to examine the major components of the cytoskeleton one by one. The detailed results of all perturbation experiments are summarized in **Table S5**. In the next paragraph, we present an extended discussion to support the opinions in the main text.

Rho Activator II, which enhances RhoA levels, promoted actin polymerization, while Y-27632 inhibited Rho, thereby suppressing actin polymerization. Our results demonstrated that the addition of Rho Activator II under normoxia conditions significantly increased the fusion frequency of tumor spheroids (23.9 % in normoxia vs. 49.5 % Rho Activator II treatment) and notably decreased fusion time (21.1 hours in normoxia vs. 6.4 hours after treatment), leading to increased tumor formation rates. Conversely, the addition of Y-27632 under hypoxia conditions reduced tumor formation rates and fusion frequency (47.5 % in hypoxia vs. 13.4 % after Y-27632 treatment), with fusion time greatly increased (9.4 hours in hypoxia vs. 28.2 hours after treatment). This suggests that promoting actin polymerization under hypoxia conditions enhances the fusion frequency of tumor spheroids, ultimately leading to increased tumor formation rates. Tumor spheroids consist of multiple cells, and intercellular interactions may influence the overall dynamics of the spheroids. The results of RNA sequencing indicated that genes mediating intercellular interactions, such as PCDH20 and PCDH15, are downregulated under hypoxia conditions (**Table 4**). By reducing DSG2 expression in tumor spheroids via RNA interference under normoxia conditions, we observed a slight increase in tumor formation rates (147 % vs. 207 %). In contrast, overexpression of DSG2 under hypoxia conditions resulted in decreased tumor formation rates (321 % vs. 188 %), indicating that intercellular interactions also impact tumor dynamics.

Effects of cell-ECM interaction.

The interactions between tumors in the tumor microenvironment significantly influence tumor growth. Transcriptome sequencing results indicated that the gene expression related to the interaction between cells and the extracellular matrix did not change. We investigated the effect of the interaction between tumor spheroids and the extracellular matrix (ECM) on tumor formation rates. Under normoxia conditions, we reduced the expression levels of ITGB3 in tumor spheroids using RNA interference (RNAi), theoretically weakening the interaction between the spheroids and the ECM and allowing greater freedom for the spheroids. Experimental results indicated that the reduction of ITGB3 did not affect the tumor formation rate (normoxia: 147 % vs. normoxia with ITGB3 RNAi: 155 %) (**Figure S8A**), nor did it change the fusion frequency of the tumor spheroids (normoxia: 23.9 % vs. normoxia with ITGB3 RNAi: 23.5 %) (**Figure S8B**). Furthermore, under hypoxia conditions, the overexpression of ITGB3 to enhance spheroid-ECM interactions also did not impact the tumor formation rate (hypoxia: 321 % vs. hypoxia with ITGB3 overexpression: 329 %). The expression of ITGB3 exhibits little effect on the dynamics of the spheroid, like the distance before fusion (**Figure S8G**) and speed (**Figure S8E**), either. These numbers are summarized in **Table S5**. Therefore, we propose that the interactions between tumor spheroids and the ECM may not play a significant role in the growth strategies observed in our study. We also examined the three-dimensional collagen gel network in which our tumor spheroids were cultured. Our findings revealed that the network consists of stacked, multi-layered two-dimensional structures, each containing multiple pores with an average diameter of approximately 30 μm (**Figures S3A and S3B**). The pore sizes are larger than the initial diameter of the tumor spheroids, suggesting that the spheroids exist in a relatively free three-dimensional environment. This may explain why interactions between cells and the ECM have a limited effect during the early growth phase of tumors.

Optimize rather than “the more the better”.

In the main text, we propose an opinion that the properties of the cytoskeletons are optimized for the proper functioning of the spheroid. Emphasizing “optimize” means there is no simple linear relationship between the spheroid dynamics and the expression of any cytoskeleton components. Instead, multiple factors are tuned and balanced into the most suitable receipt for the active fusion. This picture distinguishes the delicate bio-adaptation of tumor cells and spheroids with the scope of non-living models. In this section, we offer more experimental evidence to support our opinion further.

In the main text, we report that actin polymerization is promoted and cell-cell adhesion is weakened in response to hypoxia (**Figures 1C, 1D, 1E, and 1F**). However, if we further enhance actin polymerization or weaken cell-cell adhesion under hypoxia conditions with PHAi and RNAi

approach, the active fusion and tumorigenesis won't be further encouraged. In surprising contrast, the dynamics and tumorigenesis fall back to the value of normoxia (**Figures S10A-S10D**). There is no simple linear relationship between active fusion and spheroid stiffness either. In general, actin polymerization advances cell polarization and makes them more dynamic, and it also leads to higher stiffness. However, weakening cell-cell adhesion usually makes the spheroid softer. These two cytoskeleton factors have the opposite effect on the spheroid stiffness. The RNAi experiments on DSG2 tell the same story. Further weakening cell-cell interaction under hypoxic conditions makes the tumorigenesis behaviors similar to those under normoxic conditions (**Figures S10A-S10D**). The fact that no certain signal pathway could be identified from the sequencing data also suggests the systematic optimization of many factors (Figure S13). In summary, to realize the bio-function of the active fusion, multiple factors in the cytoskeleton are balanced to the most appropriate states.

Chemically induced hypoxia by $CoCl_2$.

Cobalt chloride (CoCl2) is one of the most commonly used models to induce chemical hypoxia. It can stabilize the expression of HIF-1α and HIF-2α in cells under normoxia conditions for relatively prolonged periods, facilitating the handling and analysis of samples within a broader time window (*86*). The stabilization and accumulation of HIF-1α occur because these chemical agents inhibit the activity of prolyl hydroxylases (PHDs), interfere with the hydroxylation of HIF-1α, and suppress the ubiquitin-dependent 26S proteasomal degradation pathway (*86-88*).

To double-check the phenomena observed under physical hypoxia in the 3-gas incubator, we conducted a chemical hypoxia experiment by adding Cobalt Chloride (CoCl2) with the following procedures. CoCl2 was purchased from Sigma (catalog number 232696). A total of 0.12984 g of CoCl2 was weighed and dissolved in 10 mL of PBS to prepare a 100 mM CoCl2 solution. The prepared solution was then filtered through a 0.22 μm filter, aliquoted into sterile centrifuge tubes, and stored at -20 °C in the dark. During the experiments, 3 μL of the prepared CoCl2 solution was added to 1 mL of culture medium before imaging. Imaging procedures were carried out as previously described.

As summarized in **Figures S14**, following CoCl2 treatment, the fusion frequency of tumor spheroids increased (39.4 % with CoCl2 treatment vs. 23.9 % under normoxia), and the fusion time was shortened (12 hours with CoCl2 treatment vs. 23 hours under normoxia). The overall behaviors of the tumor spheroids are consistent under chemical and physical hypoxia. Additionally, we monitored the expression of HIF1α at various time points post-CoCl2 treatment, finding that HIF1α mRNA expression was upregulated following CoCl2 exposure (**Figure S14F**). In contrast, no discernable upregulation of HIF1α occurs in the physical hypoxia samples (**Figure S4I**). This inconsistency in molecular pathways implies that the classical HIF1α pathway is not the major inducing factor of the active fusion.

SI References

1. T. R. Sodunke *et al.*, Micropatterns of Matrigel for three-dimensional epithelial cultures. *Biomaterials* **28**, 4006-4016 (2007).
2. F. K. Braun *et al.*, Scaffold-Based (Matrigel™) 3D Culture Technique of Glioblastoma Recovers a Patient-like Immunosuppressive Phenotype. *Cells* **12**, (2023).
3. G. Flatau *et al.*, Toxin-induced activation of the G protein p21 Rho by deamidation of glutamine. *Nature* **387**, 729-733 (1997).
4. S. Tokic *et al.*, The RhoA guanine exchange factor ABR: a glucose-sensitive mediator of actin reorganization in feto-placental arterial endothelial cells altered by gestational diabetes mellitus. *J Physiol*, (2024).
5. H. Bito *et al.*, A critical role for a Rho-associated kinase, p160ROCK, in determining axon outgrowth in mammalian CNS neurons. *Neuron* **26**, 431-441 (2000).
6. D. Isler *et al.*, Antitumoral effect of a selective Rho-kinase inhibitor Y-27632 against Ehrlich ascites carcinoma in mice. *Pharmacol Rep* **66**, 114-120 (2014).
7. J. Riedl *et al.*, Lifeact: a versatile marker to visualize F-actin. *Nat Methods* **5**, 605-607 (2008).
8. T. Mannan, S. Jing, S. H. Foroushania, F. Fortune, H. Wan, RNAi-mediated inhibition of the desmosomal cadherin (desmoglein 3) impairs epithelial cell proliferation. *Cell Prolif* **44**, 301-310 (2011).
9. G. Shan, RNA interference as a gene knockdown technique. *Int J Biochem Cell Biol* **42**, 1243-1251 (2010).
10. F. Cai *et al.*, Desmoglein-2 is overexpressed in non-small cell lung cancer tissues and its knockdown suppresses NSCLC growth by regulation of p27 and CDK2. *J Cancer Res Clin Oncol* **143**, 59-69 (2017).
11. P. G. Miller *et al.*, In Vivo RNAi screening identifies a leukemia-specific dependence on integrin beta 3 signaling. *Cancer Cell* **24**, 45-58 (2013).
12. M. Kovacheva, M. Zepp, S. Berger, M. R. Berger, Conditional knockdown of integrin beta-3 reveals its involvement in osteolytic and soft tissue lesions of breast cancer skeletal metastasis. *J Cancer Res Clin Oncol* **147**, 361-371 (2021).
13. H. J. Hu *et al.*, Integrin beta 3-overexpressing mesenchymal stromal cells display enhanced homing and can reduce atherosclerotic plaque. *World J Stem Cells* **15**, 931-946 (2023).
14. S. Mayr *et al.*, Localization Microscopy of Actin Cytoskeleton in Human Platelets. *Int J Mol Sci* **19**, (2018).
15. Z. Yu *et al.*, Targeting UBR5 inhibits postsurgical breast cancer lung metastases by inducing CDC73 and p53 mediated apoptosis. *Int J Cancer* **154**, 723-737 (2024).
16. J. Liu *et al.*, Tanshinone IIA promotes apoptosis by downregulating BCL2 and upregulating TP53 in triple-negative breast cancer. *Naunyn Schmiedebergs Arch Pharmacol* **396**, 365-374 (2023).
17. N. P. Bazhulina *et al.*, Binding of Hoechst 33258 and its derivatives to DNA. *J Biomol Struct Dyn* **26**, 701-718 (2009).
18. G. Lukinavičius *et al.*, Fluorogenic probes for live-cell imaging of the cytoskeleton. *Nat Methods* **11**, 731-733 (2014).

19. A. Sakaue-Sawano *et al.*, Visualizing spatiotemporal dynamics of multicellular cell-cycle progression. *Cell* **132**, 487-498 (2008).
20. M. Gintoli *et al.*, Spinning disk-remote focusing microscopy. *Biomed Opt Express* **11**, 2874-2888 (2020).
21. A. J. Ewald, Z. Werb, M. Egeblad, Dynamic, long-term in vivo imaging of tumor-stroma interactions in mouse models of breast cancer using spinning-disk confocal microscopy. *Cold Spring Harb Protoc* **2011**, pdb.top97 (2011).
22. S. Hayashi, Y. Okada, Ultrafast superresolution fluorescence imaging with spinning disk confocal microscope optics. *Mol Biol Cell* **26**, 1743-1751 (2015).
23. T. P. Lele, C. K. Thodeti, D. E. Ingber, Force meets chemistry: analysis of mechanochemical conversion in focal adhesions using fluorescence recovery after photobleaching. *J Cell Biochem* **97**, 1175-1183 (2006).
24. L. Qian, H. Zhao, Nanoindentation of Soft Biological Materials. *Micromachines (Basel)* **9**, (2018).
25. C. Stringer, T. Wang, M. Michaelos, M. Pachitariu, Cellpose: a generalist algorithm for cellular segmentation. *Nat Methods* **18**, 100-106 (2021).
26. I. C. Fabrice CordeliÔøΩres, Orsay. (2005).
27. M. Pachitariu, C. Stringer, Cellpose 2.0: how to train your own model. *Nat Methods* **19**, 1634-1641 (2022).
28. R. Ferretti *et al.*, Tumor cell invasion into Matrigel: optimized protocol for RNA extraction. *Biotechniques* **70**, 327-335 (2021).
29. H. M. Kim *et al.*, Comparative analysis of 7 short-read sequencing platforms using the Korean Reference Genome: MGI and Illumina sequencing benchmark for whole-genome sequencing. *Gigascience* **10**, (2021).
30. J. L. Klessner, B. V. Desai, E. V. Amargo, S. Getsios, K. J. Green, EGFR and ADAMs cooperate to regulate shedding and endocytic trafficking of the desmosomal cadherin desmoglein 2. *Mol Biol Cell* **20**, 328-337 (2009).
31. Y. P. Liu, B. Berkhout, HIV-1-based lentiviral vectors. *Methods Mol Biol* **1087**, 273-284 (2014).
32. T. Maetzig, M. Galla, C. Baum, A. Schambach, Gammaretroviral vectors: biology, technology and application. *Viruses* **3**, 677-713 (2011).
33. M. Federico, *Lentivirus Gene Engineering Protocols*. (2010).
34. R. H. Kutner, X. Y. Zhang, J. Reiser, Production, concentration and titration of pseudotyped HIV-1-based lentiviral vectors. *Nat Protoc* **4**, 495-505 (2009).
35. R. I. Freshney, Culture of Animal Cells: A Manual of Basic Technique and Specialized Applications. (2010).
36. R. J. Hay, M. L. Macy, T. R. Chen, Mycoplasma infection of cultured cells. *Nature* **339**, 487-488 (1989).
37. L. Ma *et al.*, Organoid culture of human prostate cancer cell lines LNCaP and C4-2B. *Am J Clin Exp Urol* **5**, 25-33 (2017).
38. R. A. Wimmer, A. Leopoldi, M. Aichinger, D. Kerjaschki, J. M. Penninger, Generation of

blood vessel organoids from human pluripotent stem cells. *Nat Protoc* **14**, 3082-3100 (2019).

39. M. L. Ponce, Tube formation: an in vitro matrigel angiogenesis assay. *Methods Mol Biol* **467**, 183-188 (2009).
40. D. Crosby *et al.*, Early detection of cancer. *Science* **375**, eaay9040 (2022).
41. K. Unger-Saldaña, Challenges to the early diagnosis and treatment of breast cancer in developing countries. *World J Clin Oncol* **5**, 465-477 (2014).
42. J. J. Sciubba, Oral cancer. The importance of early diagnosis and treatment. *Am J Clin Dermatol* **2**, 239-251 (2001).
43. J. D. Schiffman, P. G. Fisher, P. Gibbs, Early detection of cancer: past, present, and future. *Am Soc Clin Oncol Educ Book*, 57-65 (2015).
44. B. G. Debeb *et al.*, Characterizing cancer cells with cancer stem cell-like features in 293T human embryonic kidney cells. *Mol Cancer* **9**, 180 (2010).
45. A. A. Stepanenko, V. V. Dmitrenko, HEK293 in cell biology and cancer research: phenotype, karyotype, tumorigenicity, and stress-induced genome-phenotype evolution. *Gene* **569**, 182-190 (2015).
46. C. Shen *et al.*, The tumorigenicity diversification in human embryonic kidney 293 cell line cultured in vitro. *Biologicals* **36**, 263-268 (2008).
47. A. Muñiz-García *et al.*, Hypoxia-induced HIF1α activation regulates small extracellular vesicle release in human embryonic kidney cells. *Sci Rep* **12**, 1443 (2022).
48. Y. Chen *et al.*, SOAPnuke: a MapReduce acceleration-supported software for integrated quality control and preprocessing of high-throughput sequencing data. *Gigascience* **7**, 1-6 (2018).
49. Y. Zhang *et al.*, SAGE1: a Potential Target Antigen for Lung Cancer T-Cell Immunotherapy. *Mol Cancer Ther* **20**, 2302-2313 (2021).
50. Y. T. Chen, N. C. Panarelli, K. C. Piotti, R. K. Yantiss, Cancer-testis antigen expression in digestive tract carcinomas: frequent expression in esophageal squamous cell carcinoma and its precursor lesions. *Cancer Immunol Res* **2**, 480-486 (2014).
51. X. X. Li *et al.*, Cadherin-18 loss in prospermatogonia and spermatogonial stem cells enhances cell adhesion through a compensatory mechanism. *Zool Res* **45**, 1048-1060 (2024).
52. Y. H. Bai *et al.*, A Novel Tumor-Suppressor, CDH18, Inhibits Glioma Cell Invasiveness Via UQCRC2 and Correlates with the Prognosis of Glioma Patients. *Cell Physiol Biochem* **48**, 1755-1770 (2018).
53. B. T. Zheng *et al.*, CDH11 Regulates Adhesion and Transcellular Migration of Tongue Squamous Cell Carcinoma. *Onco Targets Ther* **14**, 4211-4222 (2021).
54. H. Ungewiß *et al.*, Dsg2 via Src-mediated transactivation shapes EGFR signaling towards cell adhesion. *Cell Mol Life Sci* **75**, 4251-4268 (2018).
55. C. Frantz, K. M. Stewart, V. M. Weaver, The extracellular matrix at a glance. *J Cell Sci* **123**, 4195-4200 (2010).
56. C. Bonnans, J. Chou, Z. Werb, Remodelling the extracellular matrix in development and disease. *Nat Rev Mol Cell Biol* **15**, 786-801 (2014).
57. R. O. Hynes, The extracellular matrix: not just pretty fibrils. *Science* **326**, 1216-1219 (2009).

58. D. E. Discher, P. Janmey, Y. L. Wang, Tissue cells feel and respond to the stiffness of their substrate. *Science* **310**, 1139-1143 (2005).
59. D. D. Sebinger, A. Ofenbauer, P. Gruber, S. Malik, C. Werner, ECM modulated early kidney development in embryonic organ culture. *Biomaterials* **34**, 6670-6682 (2013).
60. E. D. Hay, Extracellular matrix, cell skeletons, and embryonic development. *Am J Med Genet* **34**, 14-29 (1989).
61. P. Bainbridge, Wound healing and the role of fibroblasts. *J Wound Care* **22**, 407-408, 410-412 (2013).
62. F. X. Maquart, J. C. Monboisse, Extracellular matrix and wound healing. *Pathol Biol (Paris)* **62**, 91-95 (2014).
63. R. B. Diller, A. J. Tabor, The Role of the Extracellular Matrix (ECM) in Wound Healing: A Review. *Biomimetics (Basel)* **7**, (2022).
64. P. Lu, K. Takai, V. M. Weaver, Z. Werb, Extracellular matrix degradation and remodeling in development and disease. *Cold Spring Harb Perspect Biol* **3**, (2011).
65. M. G. Vander Heiden, L. C. Cantley, C. B. Thompson, Understanding the Warburg effect: the metabolic requirements of cell proliferation. *Science* **324**, 1029-1033 (2009).
66. S. Y. Lunt, M. G. Vander Heiden, Aerobic glycolysis: meeting the metabolic requirements of cell proliferation. *Annu Rev Cell Dev Biol* **27**, 441-464 (2011).
67. G. L. Semenza, Hypoxia-inducible factors in physiology and medicine. *Cell* **148**, 399-408 (2012).
68. A. Marín-Hernández, J. C. Gallardo-Pérez, S. J. Ralph, S. Rodríguez-Enríquez, R. Moreno-Sánchez, HIF-1alpha modulates energy metabolism in cancer cells by inducing over-expression of specific glycolytic isoforms. *Mini Rev Med Chem* **9**, 1084-1101 (2009).
69. C. M. Metallo *et al.*, Reductive glutamine metabolism by IDH1 mediates lipogenesis under hypoxia. *Nature* **481**, 380-384 (2011).
70. X. Wang *et al.*, Hypoxia-induced myeloid derived growth factor promotes hepatocellular carcinoma progression through remodeling tumor microenvironment. *Theranostics* **11**, 209-221 (2021).
71. N. Koundouros, G. Poulogiannis, Reprogramming of fatty acid metabolism in cancer. *Br J Cancer* **122**, 4-22 (2020).
72. D. Hanahan, R. A. Weinberg, Hallmarks of cancer: the next generation. *Cell* **144**, 646-674 (2011).
73. X. Hao, Y. Ren, M. Feng, Q. Wang, Y. Wang, Metabolic reprogramming due to hypoxia in pancreatic cancer: Implications for tumor formation, immunity, and more. *Biomed Pharmacother* **141**, 111798 (2021).
74. J. W. Kim, I. Tchernyshyov, G. L. Semenza, C. V. Dang, HIF-1-mediated expression of pyruvate dehydrogenase kinase: a metabolic switch required for cellular adaptation to hypoxia. *Cell Metab* **3**, 177-185 (2006).
75. K. Smolková, P. Ježek, The Role of Mitochondrial NADPH-Dependent Isocitrate Dehydrogenase in Cancer Cells. *Int J Cell Biol* **2012**, 273947 (2012).
76. S. B. Wu, Y. H. Wei, AMPK-mediated increase of glycolysis as an adaptive response to

oxidative stress in human cells: implication of the cell survival in mitochondrial diseases. *Biochim Biophys Acta* **1822**, 233-247 (2012).

77. H. Sun *et al.*, USP11 promotes growth and metastasis of colorectal cancer via PPP1CA-mediated activation of ERK/MAPK signaling pathway. *EBioMedicine* **48**, 236-247 (2019).
78. L. Santarpia, S. M. Lippman, A. K. El-Naggar, Targeting the MAPK-RAS-RAF signaling pathway in cancer therapy. *Expert Opin Ther Targets* **16**, 103-119 (2012).
79. E. F. Wagner, A. R. Nebreda, Signal integration by JNK and p38 MAPK pathways in cancer development. *Nat Rev Cancer* **9**, 537-549 (2009).
80. J. Y. Fang, B. C. Richardson, The MAPK signalling pathways and colorectal cancer. *Lancet Oncol* **6**, 322-327 (2005).
81. C. R. Weston, R. J. Davis, The JNK signal transduction pathway. *Curr Opin Cell Biol* **19**, 142-149 (2007).
82. Y. J. Guo *et al.*, ERK/MAPK signalling pathway and tumorigenesis. *Exp Ther Med* **19**, 1997-2007 (2020).
83. P. H. Maxwell *et al.*, The tumour suppressor protein VHL targets hypoxia-inducible factors for oxygen-dependent proteolysis. *Nature* **399**, 271-275 (1999).
84. T. Ishizaki *et al.*, Pharmacological properties of Y-27632, a specific inhibitor of rho-associated kinases. *Mol Pharmacol* **57**, 976-983 (2000).
85. T. Wang, W. Kang, L. Du, S. Ge, Rho-kinase inhibitor Y-27632 facilitates the proliferation, migration and pluripotency of human periodontal ligament stem cells. *J Cell Mol Med* **21**, 3100-3112 (2017).
86. J. Muñoz-Sánchez, M. E. Chánez-Cárdenas, The use of cobalt chloride as a chemical hypoxia model. *J Appl Toxicol* **39**, 556-570 (2019).
87. A. Vengellur, J. J. LaPres, The role of hypoxia inducible factor 1alpha in cobalt chloride induced cell death in mouse embryonic fibroblasts. *Toxicol Sci* **82**, 638-646 (2004).
88. Z. Ji *et al.*, Induction of hypoxia-inducible factor-1alpha overexpression by cobalt chloride enhances cellular resistance to photodynamic therapy. *Cancer Lett* **244**, 182-189 (2006).

Fig. S1. Schematics of the experimental design and workflow of this study. In the sample preparation stage, lentivirus is used to construct cell lines expressing target proteins with fluorescent tags. The cells are seeded into a three-dimensional matrix gel network, and spheroids are allowed to form over 24 hours. Live-cell imaging is then performed on the integrated platform composed of a spinning disk confocal microscope and a three-gas incubator. The whole dynamical processes over extended periods are recorded under various oxygen concentrations with minimal phototoxicity. The obtained imaging data are processed by AI-based cell segmentation. The dynamic information of the tumor spheroid is extracted using homebuilt MATLAB codes and the ImageJ plugin. Advanced molecular cell biology techniques, including transcriptomic sequencing and qPCR, are used to further elucidate the molecular mechanisms behind the dynamical phenotype.

Fig. S2. Validation of the techniques, materials, and methods used in this study. (**A, B, C, and D**) qPCR quantification of mRNA expression levels of Lifeact labeled with green fluorescence to indicate F-actin in HEK293T-Actin-H2B (**A**), H2B in HEK293T-Actin-H2B (**B**), DSG2 in HEK293T-DSG2OE (**C**) and ITGB3 in HEK293T-ITGB3OE (**D**) cell lines. (**E, F, G, and H**) Electrophoresis results of PCR-amplified target genes inserted into the expression vector. E corresponds to Lifeact, F to H2B, G to DSG2, and H to ITGB3. Lane 1: negative control (ddH_2O); Lane 2: negative control (empty vector); Lane 3: positive control (GAPDH); Lane 4: DNA ladder, with bands from top to bottom corresponding to 5 kb, 3 kb, 2 kb, 1.5 kb, 1 kb, 750 bp, 500 bp, 250 bp, and 100 bp; Lanes 5–8: transformants. (**I, J, K, and L**) Representative confocal images of the established cell lines expressing green fluorescence for F-actin (**I**), red fluorescence for H2B (**J**), red fluorescence for DSG2 (**K**), and red fluorescence for ITGB3 (**L**). (**M**) qPCR quantification of mRNA expression levels of Geminin in the fluorescently labeled cell line for Cdt1 and Geminin. (**N**) Agarose gel electrophoresis analysis of PCR products amplifying the target gene Geminin after its insertion into the expression vector. Lane 1: negative control (ddH_2O); Lane 2: negative control (empty vector); Lane 3: positive control (GAPDH); Lane 4: DNA ladder with bands (from top to bottom): 5 kb, 3 kb, 2 kb, 1.5 kb, 1 kb, 750 bp, 500 bp, 250 bp, and 100 bp; Lanes 5–8: transformants. (**O, P**) qPCR quantification of mRNA expression levels of ITGB3 in the ITGB3 RNAi cell line (**O**) and DSG2 in the DSG2 RNAi cell line (**P**). (**Q, R**) Cell cycle profiling of the established cell line: Cdt1 (red, G1 phase) and Geminin (green, S/G2/M phases). (**S, T**) RNAi validation: blue fluorescence indicates shRNA transfection for ITGB3 (**S**) and DSG2 (**T**). For all statistical plots, unpaired Student's t-test ($n > 3$ experiments, data are mean ± SEM) was conducted for all data with **** $P < 0.0001$, *** $P < 0.001$, ** $P < 0.1$, * $P < 0.5$, ns $P > 0.5$. The error bars are the standard error of the mean of the data.

Fig. S3. The workflow comprised a 3D culture system, robust cell segmentation, and stringent RNA-seq quality control. (**A, B**) Three-dimensional network structure of the matrix gel under bright field (**A**) and confocal illumination (**B**). The scale bar is 20 μm. (**C**) Confocal microscopy images of two-dimensional cultured cells, with red fluorescence labeling H2B and green fluorescence labeling F-actin. (**D**) The data from (**C**) were imported into CellPose 2.0 and

after adjusting the relevant parameters, the cell segmentation was conducted. The shaded area and the dashed line are the cell body and cell boundary detected by CellPose, respectively. (**E**) 3D reconstruction of the tumor spheroid composed of HEK293T-Actin-H2B cells from the z-stack of confocal microscopy images. The reconstruction is done by CellSens Dimension Desktop 4.2.1, with red fluorescence labeling H2B and green fluorescence labeling F-actin. (**F**) Distribution of bases and quality after filtering the transcriptome data from 24-hour normoxia culture. The left panel shows the base positions within the reads on the x-axis and the proportion of each base type on the y-axis; different colors represent different base types. Under normal conditions, samples exhibit separation of AT and CG bases. The observed jitter in the first few base pairs is attributed to the instability of random primers and enzyme-substrate binding during the sequencing reaction, representing normal variability inherent to the sequencing process. The right panel displays the base positions on the x-axis and the quality values of individual bases on the y-axis; each point represents the quality value of the corresponding base in the reads. The intensity of color indicates the number of bases; a deeper color at a specific quality value indicates a higher proportion of that quality value in the sequencing data.

Fig. S4. Molecular analysis on relevant bio-chemical factors. (**A**) Volcano plots of differentially expressed genes under 3D and 2D culture. Cancer-related genes are indicated by black arrows. (**B, C**) mRNA expression levels of ALDH1A (**B**) and SAGE1(**C**) in two-dimensional and three-dimensional cultured cells. The different time points in (B) refer to the time after the cells are subjected to hypoxia. (**D, E, and F**) KEGG enrichment analysis of differentially expressed genes on biological process (**D**), cellular component (**E**), and molecular function (**F**). The bubble plot illustrates the top ten representative results. The y-axis is described as follows. d1:extracellular structure organization, d2:extracellular matrix organization,, d3: positive regulation of cell adhesion, d4: cell−cell adhesion via plasma−membrane adhesion molecules, d5: G protein−coupled receptor signaling pathway, coupled to cyclic nucleotide second messenger, d6: potassium ion transport, d7: adenylate cyclase−modulating G protein−coupled receptor signaling pathway, d8: potassium ion transmembrane transport, d9: multicellular organismal signaling, d10:regulation of blood pressure; e1: collagen−containing extracellular matrix, e2: transporter complex, e3: transmembrane transporter complex, e4: synaptic membrane, e5: ion channel complex, e6: apical plasma membrane, e7: endoplasmic reticulum lumen, e8: cation channel complex, e9: potassium channel complex, e10: voltage−gated potassium channel complex; f1: passive transmembrane transporter activity, f2: channel activity, f3: ion channel activity, f4: metal ion transmembrane transporter activity, f5: monovalent inorganic cation transmembrane transporter activity, f6: gated channel activity, f7: cation channel activity, f8: voltage−gated ion channel activity, f9: voltage−gated channel activity, f10: potassium channel activity The size of each bubble represents the number of genes involved, the color indicates the significance level (p-value). Data are from three independent experiments. (**G, H, and I**) mRNA expression levels of, MAP6 (**G**), DSG2 (**H**), and HIF1α (**I**) in three-dimensional cultured cells. The different time points in the plots refer to the time after the cells are subjected to hypoxia. (**J, K**) Quantitative analysis of the normalized gene expression levels of the mitochondrial membrane protein MTFP1 (**J**) and

the mitochondrial transport complex subunit TOMM20L (**K**) under normoxic and hypoxic conditions from transcriptome sequencing data. For all statistical plots, unpaired Student's t-test (n > 3 experiments, data are mean ± SEM) was conducted for all data with **** P < 0.0001, *** P < 0.001, ** P < 0.1, * P <0.5, ns P > 0.5. The error bars are the standard error of the mean of the data.

Fig. S5. Dynamics of Directed Fusion in tumor spheroids. (**A**) Speed in 3-dimension of tumor spheroids under different culture conditions of normoxia, hypoxia, PHAi, and RNAi treatment. (**B**) The distance between the non-fused tumor spheres and their initial positions over time under various conditions of normoxia, hypoxia, PHAi, and RNAi treatment. (**C**) The distance between two tumor spheroids before active fusion occurs under various conditions of normoxia, hypoxia, PHAi, and RNAi treatment. (D, E, F, and G) Typical trajectories of two fusing tumor spheroids under various conditions of 21% normal oxygen (**D**), 2% hypoxia (**E**), normoxia treated with Rho-activate II (**F**), and hypoxia treated with Y-27632 (**G**). The data is a typical reflection of three independent experiments. The dashed and solid vectors represent the trajectory of the two spheroids each. The direction and length of the vectors indicate the movement direction and speed of the spheroids at each time point, respectively. The color represents the time. For all statistical plots, unpaired Student's t-test (n > 3 experiments, data are mean ± SEM) was conducted for all data with **** P < 0.0001, *** P < 0.001, ** P < 0.1, * P <0.5, ns P > 0.5. The error bars are the standard error of the mean of the data.

Fig. S6. Additional analysis on the outreaching F-actin and tiny cells. (A, B, C and D) Representative confocal images out of three independent experiments demonstrating the channels formed by outreaching F-actin between tumor spheroids under hypoxia conditions. The green channel is Phalloidin which labels F-actin, and the blue channel is Hoechst which labels nuclei. The scale bar is 20 µm. (E, F, G and H) Representative time-lapse confocal images showing the formation of channels between two tumor spheroids through F-actin. Red fluorescence represents F-actin labeled with SiR-actin. The scale bar represents 20 µm. (I, J, K and L) Representative confocal images out of two independent experiments demonstrating that the nuclei of the tiny cells locate between two fusing tumor spheroids under hypoxia conditions. The white dotted circle indicate the position of the tiny cells. The cells are labeled with FUCCI, in which the color indicates different stages of the cell cycle. - Red marks hCdt1, indicating cells are in the G1 phase, and green marks hGem, indicating cells are in the S/G2/M phases. The scale bar is 10 µm. (M, N, O and P) Representative structured illumination microscopy (SIM) images of tumor spheroids out of three independent immunostaining experiments proving that tiny cells contain chromosome materials. The cell nuclei are labeled with Hoechst. The white dotted circle indicates the tiny cells. The scale bar is 10 µm. (Q) Average area of nuclei inside and outside the channels formed by F-actin during tumor spheroid fusion. (R) The angle between the long axis of cell nuclei and the direction of the channel itself. (S) Ratio of the long axis length to the short axis length of cell nuclei inside and outside the F-actin channels. (T) Probability distribution of nucleus sizes calculated from the immunostaining data under hypoxia and normoxia conditions in 3D control. For all

statistical plots, unpaired Student's t-test (n = 3 experiments, data are mean ± SEM) was conducted for all data with **** P < 0.0001, *** P < 0.001, ** P < 0.1, * P <0.5, ns P > 0.5. The error bars are the standard error of the mean of the data.

Fig. S7. Laser ablation experiments on the outreaching F-actin and tiny cells. (A, B, and C) Representative confocal images showing the effects of laser ablation on micronuclei after culturing for 42 hours under normoxia conditions (A) or for 42 hours under 2% oxygen conditions (B), laser ablation followed by continued hypoxia culture for an additional 24 hours (C). The green fluorescence indicates F-actin labeled with phalloidin, while the blue fluorescence marks the nuclei with Hoechst. The scale bar is 200 µm. (D) Tumor spheroid sizes under different culture conditions. (E, F, and G) Representative confocal images depicting the channels formed between two tumor spheroids after laser ablation following 42 hours of culture under normoxia conditions (E) or 42 hours under 2% oxygen conditions (F), and laser ablation then continued hypoxia culture for an additional 42 hours (G). The green fluorescence indicates F-actin labeled with phalloidin, while the blue fluorescence marks the nuclei with Hoechst. The scale bar is 200 µm. (H) Tumor spheroid sizes under different culture conditions. For all statistical plots, unpaired Student's t-test (n = 3 experiments, data are mean ± SEM) was conducted for all data with **** P < 0.0001, *** P < 0.001, ** P < 0.1, * P <0.5, ns P > 0.5. The error bars are the standard error of the mean of the data.

Fig. S8. Regulation of ITGB3 expression does not affect tumorigenesis mediated by active fusion under hypoxia conditions. (**A**) Tumorigenesis rate of HEK293T cells under different conditions of normoxia, hypoxia, ITGB3-OE, and ITGB3-RNAi treatments. (**B**) Fusion frequency of tumor spheroids under different culture conditions. (**C**) Proportion of active and growth modes in the fusion under different culture conditions of normoxia, hypoxia, ITGB3-OE, and ITGB3-RNAi treatments. (**D**) Time required for the active fusion under different culture conditions of normoxia, hypoxia, ITGB3-OE, and ITGB3-RNAi treatments. (**E**) Speed in 3-dimension of tumor spheroids under different culture conditions of normoxia, hypoxia, ITGB3-OE, and ITGB3-RNAi treatments. (**F**) Circularity of the tumor spheroid during active fusion under different culture conditions. (**G**) The distance between two tumor spheroids before active fusion occurs under various conditions of normoxia, hypoxia, ITGB3-OE, and ITGB3-RNAi treatments. (**H**) The distance between the non-fused tumor spheroids and their initial positions over time under various conditions of normoxia, hypoxia, ITGB3-OE, and ITGB3-RNAi treatments. For all statistical plots, unpaired Student's t-test (n > 3 experiments, data are mean ± SEM) was conducted for all data with **** P < 0.0001, *** P < 0.001, ** P < 0.1, * P <0.5, ns P > 0.5. The error bars are the standard error of the mean of the data.

Fig. S9. Comparison between the cell behaviors in 3D and 2D cultures under hypoxia. (A) Confocal images of HEK293T cells cultured under normoxia conditions (left) and hypoxia conditions (right) for 42 hours. The white lines indicate the borders of the cell colonies. The green and red channels are LifeAct and H2B, respectively. The scale bar is 100 µm. The images are

representative ones from more than three independent experiments. (B) Frequency of cell cluster fusion within ten hours under various culture conditions. (C) Relative cell number changes 42 hours after seeding. (D, E) Typical trajectories of HEK293T cell clusters under normoxia (D) and hypoxia (E) conditions in two-dimensional culture. (F) Speed of HEK293T cells under different culture conditions in 2D. (G, H) Confocal images of HEK293T-FUCCI cells from 3 independent experiments under nomoxia (G) and hypoxia (H) conditions in 2D culture. The left and right panels are images taken at 0 hours and 42 hours, respectively, after cell seeding. The green and red channels are hGem and hCdt1, respectively. The scale bar is 20 μm. (I, J) Proportion of cells in G1 phase and S/G2/M phases under normoxia (I) or hypoxia (J) conditions as a function of time. (K) Proportion of HEK293T cells in the S/G2/M phases under hypoxia and normoxia conditions in 2D culture. For all statistical plots, unpaired Student's t-test ($n > 3$ experiments, data are mean ± SEM) was conducted for all data with **** $P < 0.0001$, *** $P < 0.001$, ** $P < 0.1$, * $P <0.5$, ns $P > 0.5$. The error bars are the standard error of the mean of the data.

Fig. S10. Effect of DSG2 expressionand further actin polymeration. (**A**) Fusion frequency of tumor spheroids under different culture conditions of normoxia, hypoxia, PHAi and RNAi treatments. (**B**) Proportion of directed and growth modes in the fusion under different culture conditions of normoxia, hypoxia, PHAi and RNAi treatments. (**C**) The distance between two tumor spheroids before active fusion occurs under various conditions of normoxia, hypoxia, PHAi and RNAi treatment. (**D**) Speed in 3-dimension of tumor spheroids under different culture conditions of normoxia, hypoxia, PHAi and RNAi treatment. For all statistical plots, unpaired Student's t-test ($n > 3$ experiments, data are mean ± SEM) was conducted for all data with **** $P < 0.0001$, *** $P < 0.001$, ** $P < 0.1$, * $P <0.5$, ns $P > 0.5$. The error bars are the standard error of the mean of the data.

Fig. S11. Representative scanning electron microscopy (SEM) images of cancer spheroids under normoxic and hypoxic conditions in three-dimensional (3D) culture after 42 hours, showing different Z-axis planes. (A, B, C and D) SEM images of the same cancer spheroid cultured under 21% oxygen for 42 hours, captured at different depths. The scale bar is 5 μm. (E, F, G and H) SEM images of the same cancer spheroid cultured under 2% oxygen for 42 hours, captured at different depths. The scale bar is 5 μm.

Fig. S12. Schematic summary of early tumorigenesis under normoxia and hypoxia conditions. The overall tumorigenesis is significantly promoted by hypoxia treatment due to the altered dynamical phenotype of the tumor spheroids, including the major contribution from active fusion and minor contribution from enhanced growth. At the cellular level, the active fusion is directed by the outreaching F-actin and tiny cells that bridge the gaps between the fusion spheroids. At the molecular level, cytoskeleton proteins and nucleus are optimized for the structural basis for the dynamics and mechanics of the tumor spheroids, leading to their proper biological function in adaptation to hypoxia.

Fig. S13. Pathway enrichment in the transcriptome sequencing data under hypoxia conditions. (**A**) Enrichment of the cancer-related MAPK signaling pathway. (**B**) Enrichment of hypoxia-inducible factor-related signaling pathways. (**C**) Enrichment of carbon metabolism signaling pathways in cancer cells that support the energy demand of rapid proliferation. (**D**) Enrichment of adhesion molecule-related signaling pathways.

Fig. S14. Address the chemical simulation of hypoxia using $CoCl_2$ enhances tumorigenesis by promoting the active fusion of tumor spheroids. (**A**) Fusion frequency of tumor spheroids under different culture conditions. (**B**) Proportion of active and growth modes in the fusion under different culture conditions of normoxia, $CoCl_2$, PHAi treatments. (**C**) Time required for the active fusion under different culture conditions of normoxia, $CoCl_2$, PHAi, and DSG2-OE treatments. (**D**) The distance between two tumor spheroids before active fusion occurs under various conditions of normoxia, $CoCl_2$, PHAi, and DSG2-OE treatments. (**E**) Speed in 3-dimension of tumor spheroids under different culture conditions of normoxia, $CoCl_2$, PHAi, and DSG2-OE treatments. (**F**) mRNA expression levels of HIF1α in cells subjected to $CoCl_2$-induced chemical hypoxia at different time points. For all statistical plots, unpaired Student's t-test ($n > 3$ experiments, data are mean ± SEM) was conducted for all data with **** $P < 0.0001$, *** $P < 0.001$, ** $P < 0.1$, * $P < 0.5$, ns $P > 0.5$. The error bars are the standard error of the mean of the data.

Table S1.

List of primers required for qPCR validation of relevant gene mRNA expression levels.

Gene	primer
actin-F	CATGTACGTTGCTATCCAGGC
actin-R	CTCCTTAATGTCACGCACGAT
GMNN-F	GCCCTGGGGTTATTGTCCC
GMNN-R	AGCGCCTTTCTCCGTTTTTCT
ALDH1A1-F	GCACGCCAGACTTACCTGTC
ALDH1A1-R	CCTCCTCAGTTGCAGGATTAAAG
SAGE1-F	ACTTCAAACGAGTCAACCAACT
SAGE1-R	TCTAACCACGAGGACATACTCTT
MAP6-F	TTGATCGCAGAAGAATACGCAG
MAP6-R	GCCTTCCTCGTGGGCTTAT
DSG2-F	TGCTGCTTCTCCTGATCTGC
DSG2-R	CAGATCCTCTCCCTCCCGAA
HIF1α-F	GAACGTCGAAAAGAAAAGTCTCG
HIF1α-R	CCTTATCAAGATGCGAACTCACA
LifeAct-F	TGCTTCAGCCGCTACCC
LifeAct-R	AGTTCACCTTGATGCCGTTC
H2B-F	CACTACGACGCTGAGGTCAAG
H2B-R	TGGTGTAGTCCTCGTTGTGGG
ITGB3-F	CAGGCCCAAGCTGAACCTAA
ITGB3-R	GAGAAGTCGTCACACTCGCA

Table S2.

Summary of all cell lines used in this study.

ID	Name	Description	Excitation wavelength [nm]
1	HEK293T LifeAct	Visualize F-actin	488
2	HEK293T H2B	Visual nucleus	561
3	HEK293T FUCCI	Visualization and analysis of cell division cycle	488/561
4	HEK293T $DSG2^{OE}$	DSG2 was overexpressed	561
5	HEK293T $ITGB3^{OE}$	ITGB3 was overexpressed	561
6	HEK293T $DSG2^{RNAi}$	DSG2 expression levels were persistently decreased	405
7	HEK293T $ITGB3^{RNAi}$	ITGB3 expression levels were persistently decreased	405
8	HEK 293T WT	Human embryonic kidney cell line	N.A

Table S3.

Comparison of gene expression levels in 3D and 2D culture conditions.

Gene	Regulation	Fold change	Description
SAGE1	up	53.43	Cancer embryonic antigen, involved in tumor occurrence and development
MAGEC2	up	18.58	Cancer embryonic antigen, involved in tumor occurrence and development
PAX1	up	16.81	Promote the occurrence and progression of cancer
CD274	up	5.10	Drive the progression of cancer
MAGEH1	up	4.73	Tumor-specific antigen
RASGRF1	up	4.77	Associated with tumorigenesis
MAGEA3	up	4.38	Cancer embryonic antigen, involved in tumor occurrence and development
PCDHGB5	up	21.23	cell-cell interactions
PCDHGA12	up	4.64	cell-cell interactions
CDH18	up	3.03	cell-cell interactions
CDH11	down	-18.07	cell-cell interactions
DSG2	No change	-1.42	cell-cell interactions
ITGB7	up	3.79	cell-extracellular matrix adhesion
ITGAX	down	-7.25	cell-extracellular matrix adhesion
ITGB3	No change	-1.51	cell-extracellular matrix adhesion

Table S4.

Comparison of gene expression levels in hypoxia and normoxia in 3D culture conditions.

Gene	Regulation	Fold change	Description
MAP6	up	2.75	Regulates microtubules polymerization
DPYSL4	up	2.90	Promotes microtubule polymerization
EPHB3	up	2.29	Regulates the polymerization of the actin cytoskeleton
NEDD9	up	2.61	Regulates the dynamic rearrangement of the cytoskeleton
MYZAP	up	2.11	Affects the dynamic rearrangement of actin filaments
FSCN1	up	2.03	Overregulation of actin filament bundling
RIGI	up	1.84	Activation of RhoA leads to the polymerization of actin filaments
COL16A1	up	2.75	Involved in the assembly and stabilization of the extracellular matrix, providing physical support to the cells
MMP23B	up	2.67	Degrading various components of the extracellular matrix, a process crucial for tissue remodeling, cell migration
HAS2	up	2.31	Synthesize hyaluronic acid
COL12A1	up	2.17	Involved in the assembly and stabilization of collagen fibers in the extracellular matrix
GCK	up	3.34	Catalyze the reaction between glucose and ATP to produce glucose-6-phosphate (G6P) and ADP
ALDOC	up	3.18	Catalyze a key reaction in the glycolytic pathway, where fructose-1,6-bisphosphate (F1,6BP) is cleaved to produce glyceraldehyde-3-phosphate (G3P) and dihydroxyacetone phosphate (DHAP).

PGK1	up	2.41	Catalyze the reaction between glyceraldehyde-3-phosphate (G3P) and phosphoenolpyruvate (PEP) to produce 1,3-bisphosphoglycerate (1,3-BPG) and ATP
PCDH15	down	-4.00	Ensures tight junctions between cells
PCDH20	down	-3.25	Participates in cell-cell adhesion
MUC19	down	-2.66	Participates in cell surface adhesion
CLDN23	down	-2.50	Encodes a tight junction protein
TJP2	down	-2.26	Encodes a tight junction protein
CD34	down	-2.18	Encodes a cell surface glycoprotein
PCDHGA12	down	-1.80	Encodes a cell adhesion protein
CDH4	down	-1.75	Promotes cell-cell adhesion and interactions.
ITGB1	No change	1.04	cell-extracellular matrix adhesion
ITGB3	No change	-1.27	cell-extracellular matrix adhesion

Tables S5.

Summary of tumorigenesis and kinetics under different culture conditions.

	Tumorigenesis Rate [%]	**Fusion Frequency [%]**	**Fusion Mode**	**Fusion Time [h]**	**Speed [µm/min]**	**Circularity**
HEK293T 21%O_2	147	23.9	Growth	21.1	0.04	0.93
HEK293T 2%O_2	321	47.5	Active	9.4	0.06	0.76
HEK293T 21%O2 Rho activate II	424	49.5	Active	6.4	0.06	0.62
HEK293T 2%O_2 Y-27632	123	13.4	Growth	28.2	0.02	0.95
HEK293T 21%O_2 $DGS2^{RNAi}$	207	38.2	Active	12.1	0.05	0.88
HEK293T 21%O_2 $ITGB3^{RNAi}$	155	23.5	Active	21.2	0.03	0.94
HEK293T 2%O_2 $DGS2^{OE}$	188	23.0	Growth	14.9	0.05	0.88
HEK293T 2%O_2 $ITGB3^{OE}$	329	46.4	Active	8.87	0.07	0.80

Movie S1.

A typical time-lapse confocal video in a large field of view that compares the tumorigenesis process under normoxia (left) and hypoxia (right) conditions in 3D culture. Imaging was performed using a 10x objective lens, with F-actin labeled with green fluorescence and H2B with red fluorescence. Images were acquired every hour over a total duration of 42 hours. The laser wavelengths used for imaging were 488 nm and 561 nm, with a laser intensity of 20 % and an exposure time of 200 ms. For each z-scanning, the image was captured every 8 μm over the range of 168 μm, resulting in a total of 21 images. The video is about 18514 times the real time. The scale bar is 100 μm.

Movie S2.

A typical time-lapse confocal video in a zoom-in field of view that compares the spheroid dynamics under normoxia (left) and hypoxia (right) conditions in 3D culture. Imaging was performed using a 60x oil objective lens, with F-actin labeled with green fluorescence and H2B with red fluorescence. Imaging was performed at 1-hour intervals over a total duration of 42 hours. The laser wavelengths used for imaging were 488 nm and 561 nm, with a laser intensity of 100 mW and an exposure time of 200 ms. For each z-scanning, the image was captured every 5 μm over the range of 65 μm, resulting in a total of 13 images. The video is 21600 times the real-time. The scale bar is 20 μm.

Movie S3.

A typical time-lapse confocal video that demonstrates the directional fusion of the tumor spheroids. Both top-down (**left**) and side view (**right**) are provided. The imaging parameters are the same as those of **Video S2**. The video is 21600 times the real-time. The scale bar is 20 μm.

Movie S4.

A typical time-lapse confocal video that demonstrates the growth fusion of the tumor spheroids. Both top-down (**left**) and side view (**right**) are provided. The imaging parameters are the same as those of **Video S2**. The video is 18800 times the real time. The scale bar is 20 μm.

Movie S5.

A typical time-lapse confocal video that compares the response of a tumor spheroid after laser ablation under normoxia (left) and hypoxia (right) conditions. The intensity of the 405 nm ablation laser was set to 50 mW, with each tumor spheroid subjected to 4-5 laser exposures. Throughout the imaging process, a 488 nm laser was utilized, capturing a single-layer image of

the maximum section of the spheroid at a frame rate of 200 fps. The video is 51 times the real-time. The scale bar is 20 μm.

Movie S6.

A typical time-lapse confocal video that demonstrates the behavior of the tumor spheroids after pharmaceutical interference of Rho Activator II (left) and Y-27632 (right). The PHAi for Rho Activator II was conducted under normoxia conditions and that for Y-27632 was done under hypoxia conditions. The imaging parameters are the same as those of **Video S2**. The video is 18900 times the real-time. The scale bar is 20 μm.

Movie S7.

A typical video that highlights the F-actin channel and tiny cells locating between the tumor spheroids under 3D hypoxia conditions. Green fluorescence was used to label F-actin with phalloidin, and blue fluorescence to label the cell nucleus with Hoechst 33258, as detailed in the experimental methods. Imaging was performed using 405 nm and 488 nm lasers, with a power of 100mW, laser intensity at 20%, and an exposure time of 200 ms. The Z-axis motor of the microscope was employed to move the sample stage along the Z-axis, acquiring continuous optical sections at different Z-axis positions, with a 2 μm interval between adjacent layers. The acquired two-dimensional images were then aligned using Cellvis software and stacked in Z-axis order. These images were processed and analyzed via algorithms to reconstruct the three-dimensional structure of the sample. The scale bar is 40 μm.

Movie S8.

A typical video for the dynamics of the outreaching F-actin that guides active fusion. Imaging was performed using a 40x objective lens, with F-actin labeled by red fluorescence. Imaging was conducted hourly over a period of 42 hours. To capture F-actin dynamics more effectively, the samples were first cultured in a hypoxic incubator for 24 hours, followed by hypoxic imaging in a live-cell workstation. A 640 nm laser was used with a power of 100 mW and an exposure time of 200 ms. For each Z-scan, images were acquired at 3 μm intervals within a 60 μm range, yielding a total of 21 images. The video is 18000 times the real time. The scale bar is 20 μm.

Movie S9.

A typical time-lapse confocal video that demonstrates the tiny cells under hypoxia conditions. The imaging parameters are the same as those of **Video S2**. The video is 18900 times the real time. The scale bar is 20 μm.

Movie S10.

A typical time-lapse confocal video that compares cell cycle dynamics in the tumor spheroid under normoxia (left) and hypoxia (right) conditions in 3D culture. Cells in the G1 phase are labeled with red fluorescence, and cells in the S/G2/M phases are labeled with green fluorescence. Other imaging parameters are the same with those of **Video S2**. The video is 19800 times the real time. The scale bar is 20 μm.

Data S1. (separate file, data-2025.10.16.xlsx)

This dataset comprises all analytical results presented in the study, organized into 13 tables. A nomenclature system is used where each table is named after its corresponding figure in the article. To access the original data for a specific statistical graph, identify the target figure, find the table sharing its name, and then match the data column using the Y-axis label of the graph.

Code S1. (separate file, code-2025.10.30.xlsx)

This table summarizes the three custom codes developed for this study. **Code S1a** quantifies the kinematic parameters (velocity magnitude and direction) of two cancer cell spheroids over time, with the direction defined as the angle between the velocity vector and the inter-centroid line. It processes the centroid coordinates tracked by Fiji as input. **Code S1b** ensures the accurate pairing of original images with their corresponding mask files subsequent to Cellpose segmentation. **Code S1c** performs morphological analysis (e.g., perimeter, area, circularity) and fluorescence intensity quantification on the segmented masks, requiring the file paths for both the raw confocal images and the resulting masks.

Fig. 1

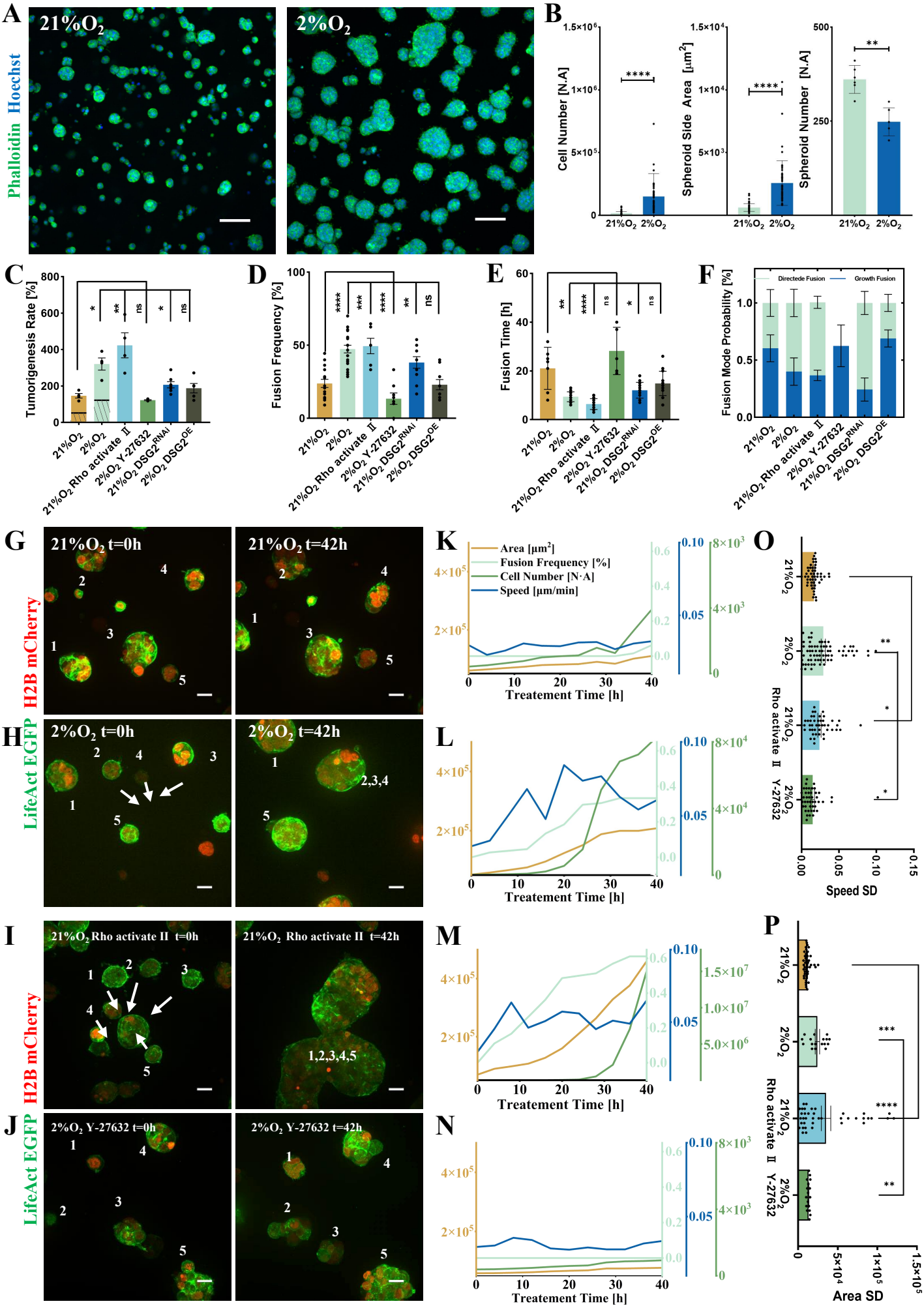
A
21%O2
2%O2
Phalloidin Hoechst
B
Cell Number [N.A]
Spheroid Side Area [μm2]
Spheroid Number [N.A]
21%O2 2%O2
C
Tumorigenesis Rate [%]
D
Fusion Frequency [%]
E
Fusion Time [h]
F
Fusion Mode Probability [%]
Directede Fusion
Growth Fusion
21%O2
2%O2
21%O2 Rho activate II
2%O2 Y-27632
21%O2 DSG2RNAi
2%O2 DSG2OE
G
21%O2 t=0h
21%O2 t=42h
H2B mCherry
H
2%O2 t=0h
2%O2 t=42h
LifeAct EGFP
I
21%O2 Rho activate II t=0h
21%O2 Rho activate II t=42h
J
2%O2 Y-27632 t=0h
2%O2 Y-27632 t=42h
K
Area [μm2]
Fusion Frequency [%]
Cell Number [N·A]
Speed [μm/min]
Treatement Time [h]
L
M
N
O
Speed SD
P
Area SD

Fig. 2

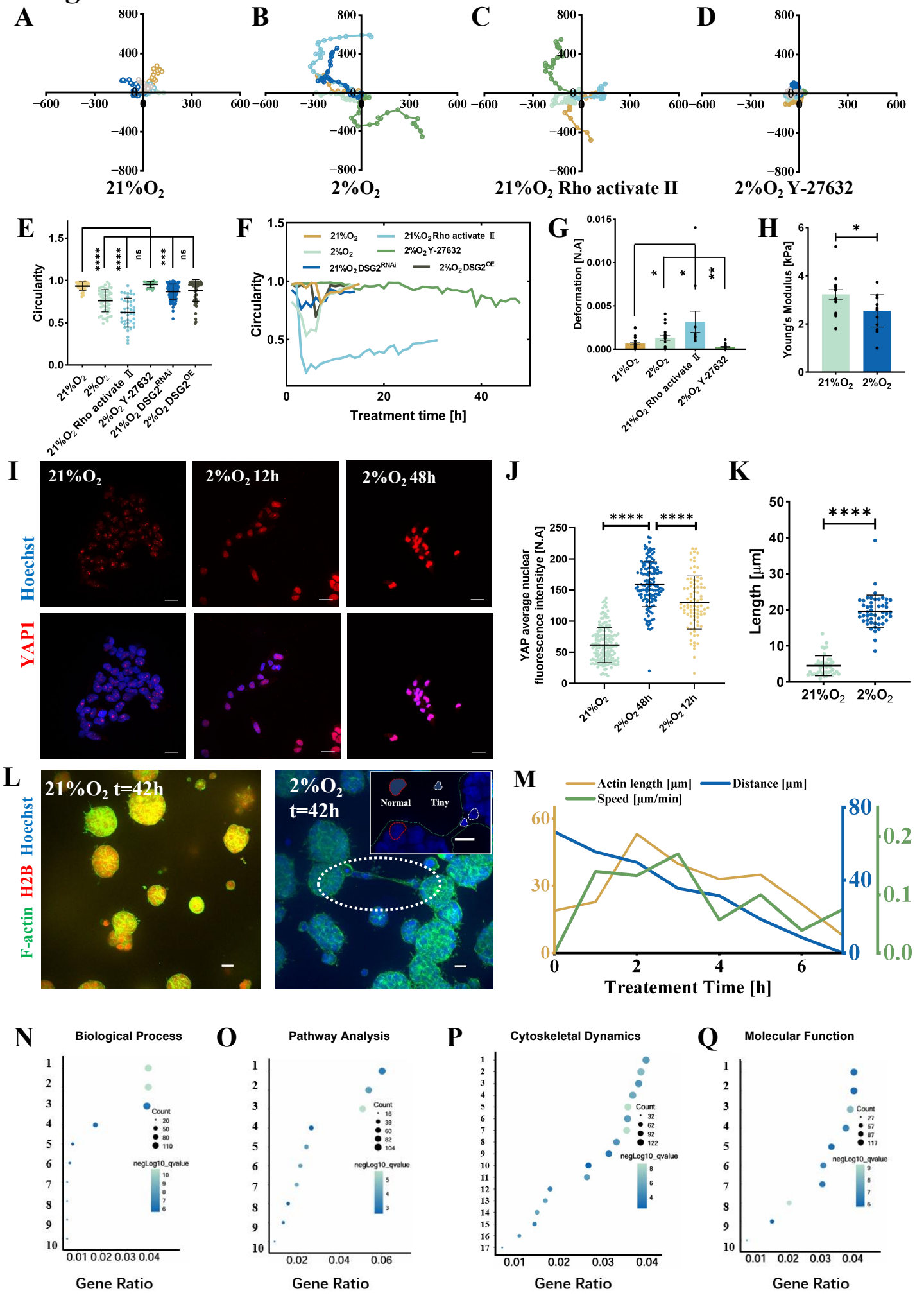
A
B
C
D
21%O2
2%O2
21%O2 Rho activate II
2%O2 Y-27632
E
Circularity
21%O2
2%O2
21%O2 Rho activate II
2%O2 Y-27632
21%O2 DSG2RNAi
2%O2 DSG2OE
F
Circularity
Treatment time [h]
G
Deformation [N.A]
H
Young's Modulus [kPa]
I
21%O2
2%O2 12h
2%O2 48h
Hoechst
YAP1
J
YAP average nuclear fluorescence intensitye [N.A]
K
Length [μm]
L
21%O2 t=42h
2%O2 t=42h
Normal
Tiny
Hoechst
H2B
F-actin
M
Actin length [μm]
Distance [μm]
Speed [μm/min]
Treatement Time [h]
N
Biological Process
O
Pathway Analysis
P
Cytoskeletal Dynamics
Q
Molecular Function
Count
negLog10_qvalue
Gene Ratio

Fig. 3

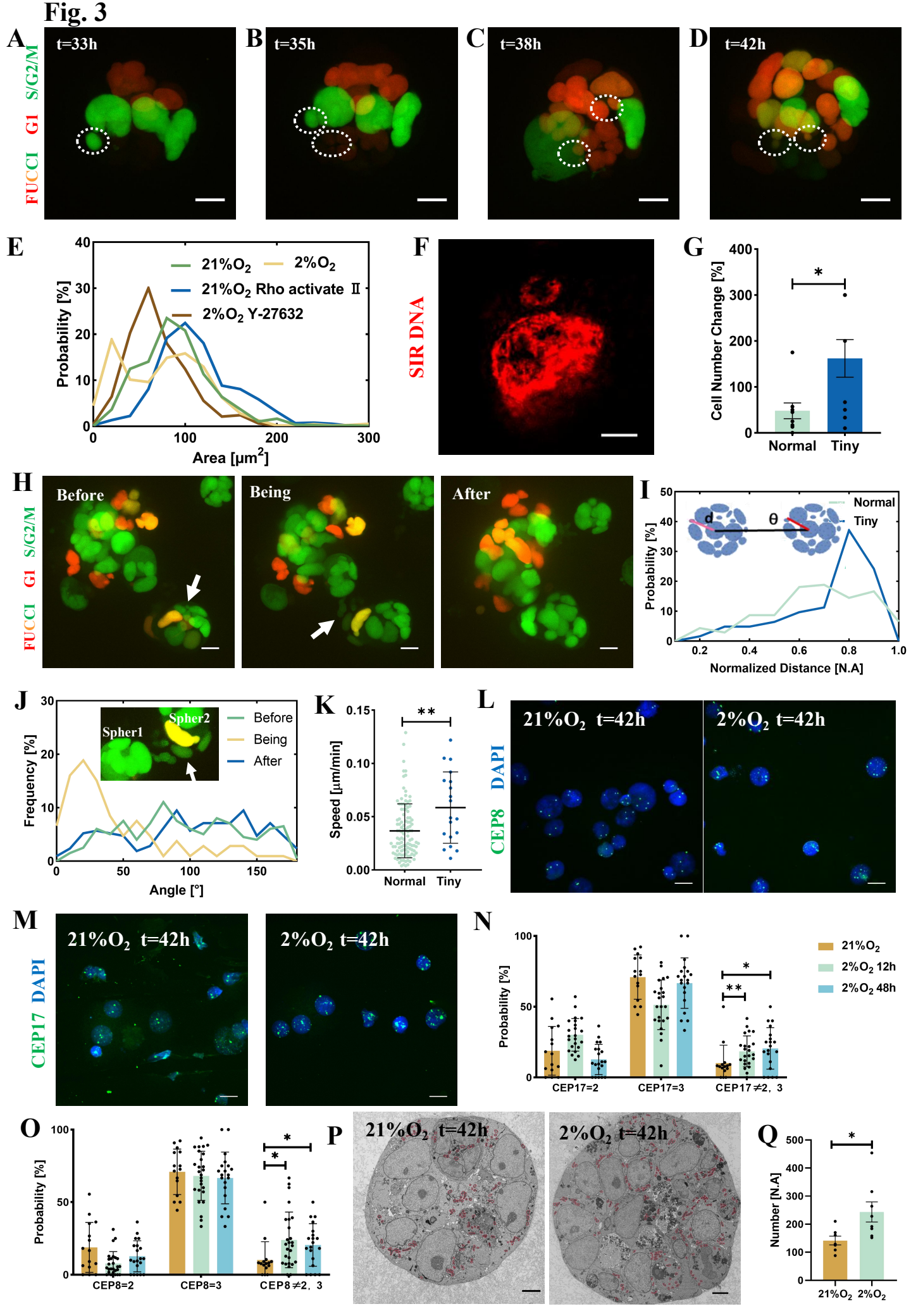
A
t=33h
B
t=35h
C
t=38h
D
t=42h
FUCCI G1 S/G2/M
E
21%O2
2%O2
21%O2 Rho activate Ⅱ
2%O2 Y-27632
Probability [%]
Area [μm2]
F
SIR DNA
G
Cell Number Change [%]
Normal
Tiny
H
Before
Being
After
FUCCI G1 S/G2/M
I
Normal
Tiny
d
θ
Probability [%]
Normalized Distance [N.A]
J
Spher1
Spher2
Before
Being
After
Frequency [%]
Angle [°]
K
Speed [μm/min]
Normal
Tiny
L
21%O2 t=42h
2%O2 t=42h
CEP8 DAPI
M
21%O2 t=42h
2%O2 t=42h
CEP17 DAPI
N
21%O2
2%O2 12h
2%O2 48h
Probability [%]
CEP17=2
CEP17=3
CEP17≠2, 3
O
Probability [%]
CEP8=2
CEP8=3
CEP8≠2, 3
P
21%O2 t=42h
2%O2 t=42h
Q
Number [N.A]
21%O2
2%O2

Fig. 4

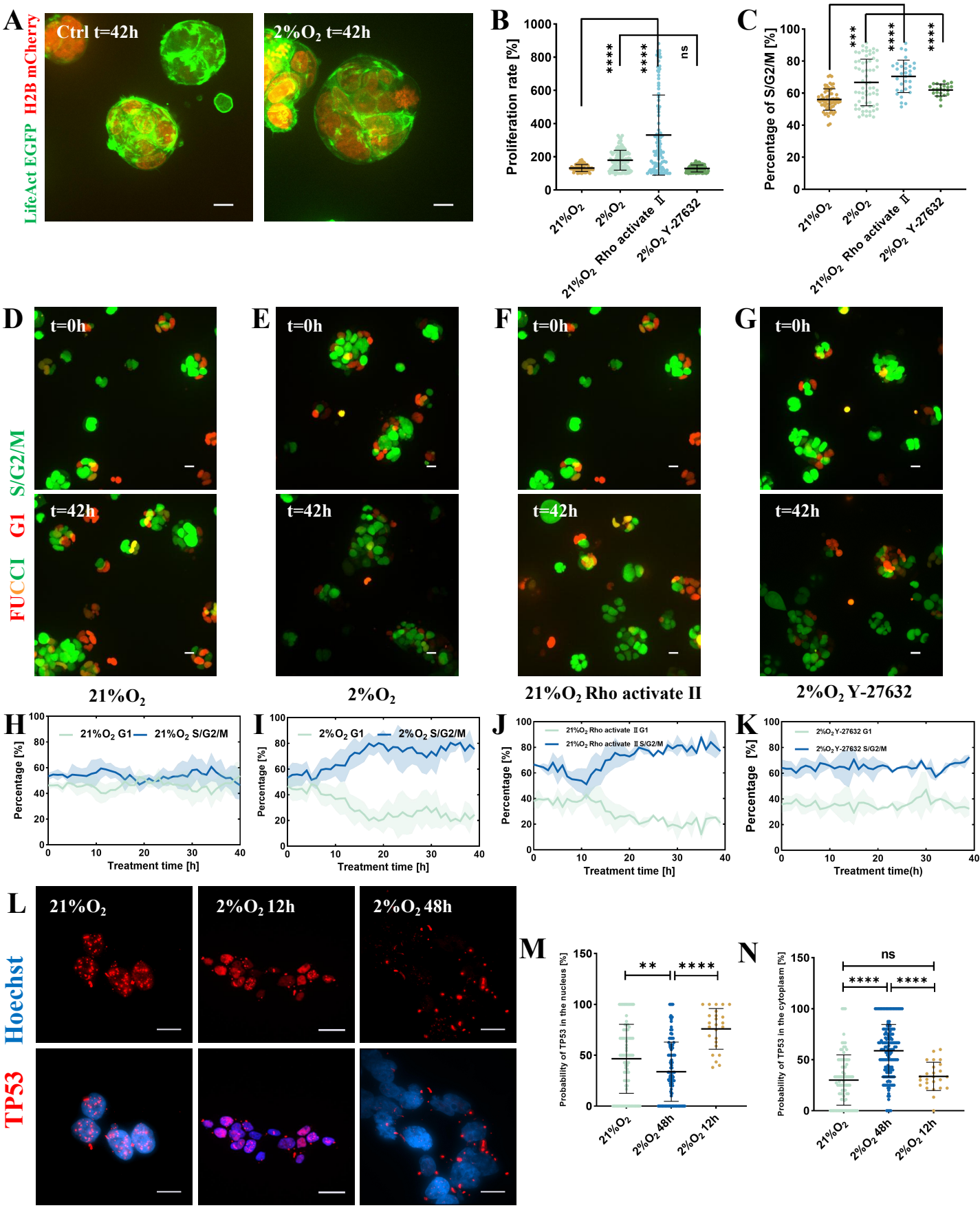
A
LifeAct EGFP H2B mCherry
Ctrl t=42h
2%O2 t=42h
B
Proliferation rate [%]
21%O2
2%O2
21%O2 Rho activate Ⅱ
2%O2 Y-27632
C
Percentage of S/G2/M [%]
D
E
F
G
FUCCI G1 S/G2/M
t=0h
t=42h
21%O2
2%O2
21%O2 Rho activate II
2%O2 Y-27632
H
I
J
K
Percentage [%]
Treatment time [h]
21%O2 G1
21%O2 S/G2/M
2%O2 G1
2%O2 S/G2/M
21%O2 Rho activate Ⅱ G1
21%O2 Rho activate Ⅱ S/G2/M
2%O2 Y-27632 G1
2%O2 Y-27632 S/G2/M
Treatment time(h)
L
Hoechst
TP53
21%O2
2%O2 12h
2%O2 48h
M
Probability of TP53 in the nucleus [%]
N
Probability of TP53 in the cytoplasm [%]
ns

Fig. S1

1. Cell Line Construction

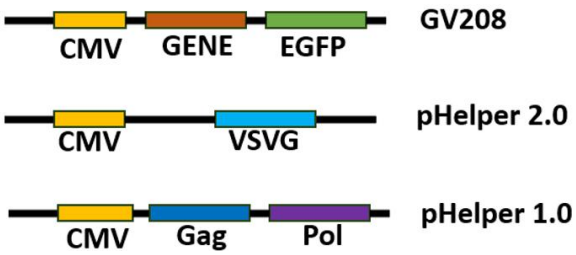

2. Three-dimensional Culture of Matrigel

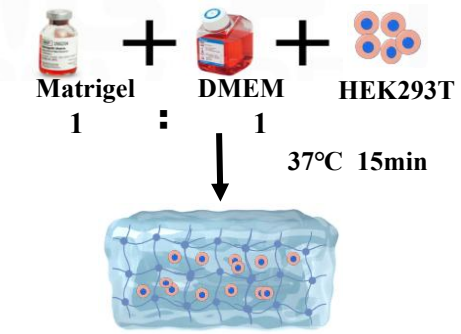

3. Live Cell Imaging

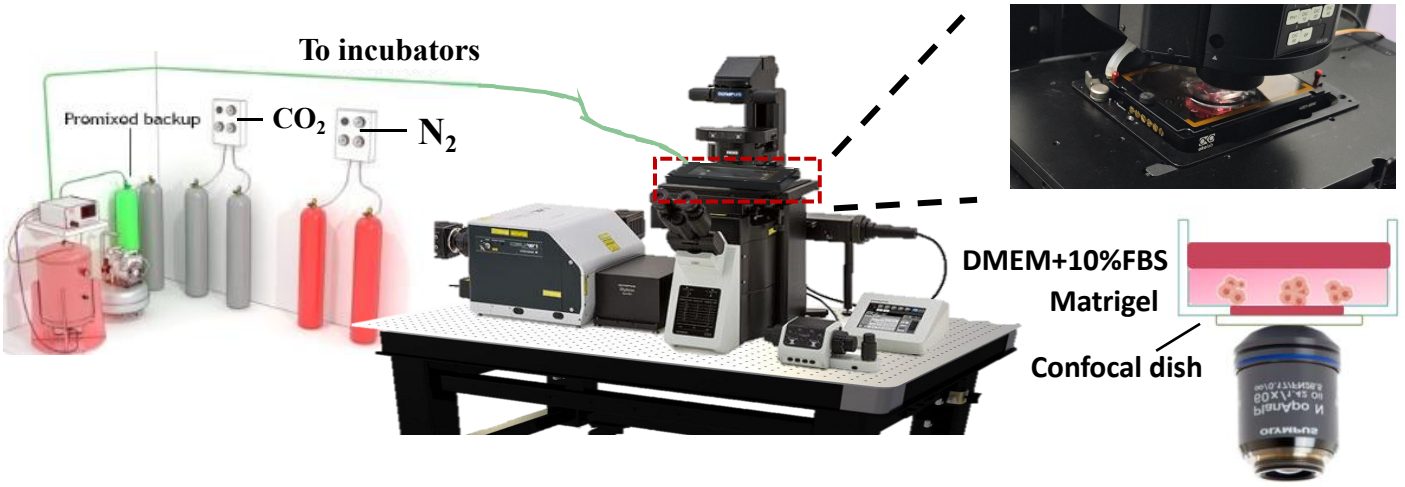

4. AI-base Image Analysis

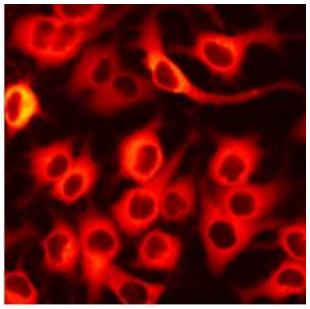

Original image

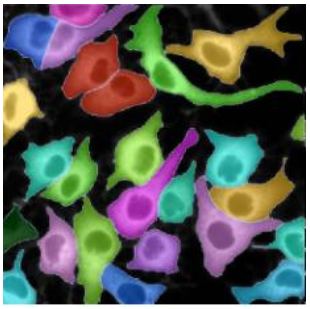

Predicted outlines

5. Advanced Molecular Cell Biology

RNA sequencing

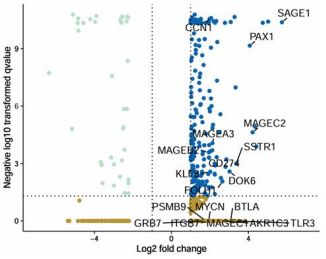

qPCR

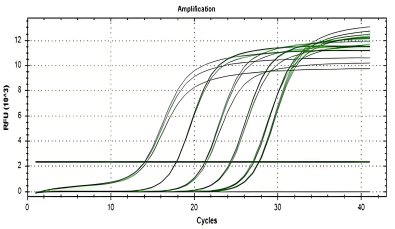

Fig. S2

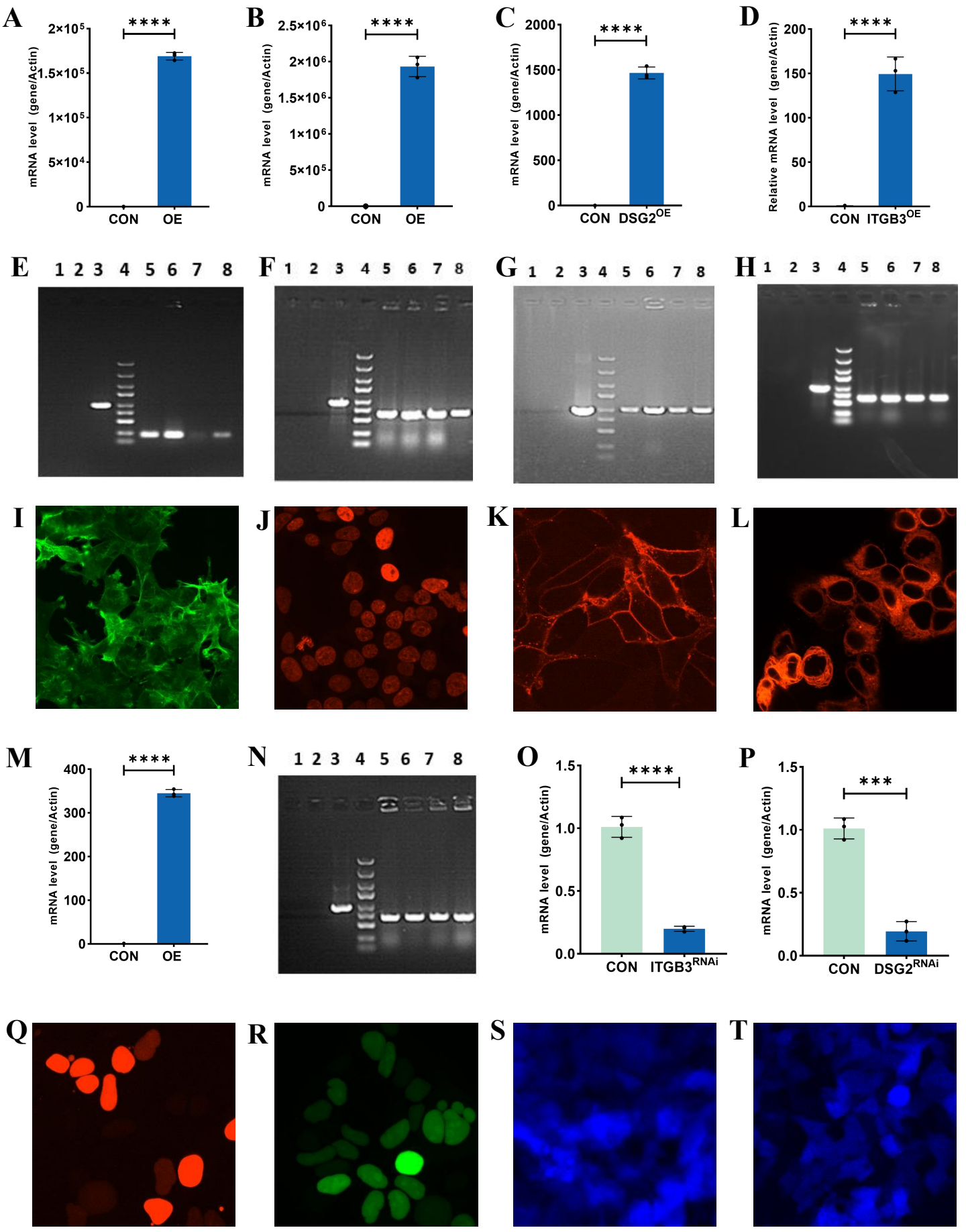
A
mRNA level (gene/Actin)
2×10⁵
1.5×10⁵
1×10⁵
5×10⁴
0
****
CON
OE
B
mRNA level (gene/Actin)
2.5×10⁶
2×10⁶
1.5×10⁶
1×10⁶
5×10⁵
0
****
CON
OE
C
mRNA level (gene/Actin)
2000
1500
1000
500
0
****
CON
DSG2OE
D
Relative mRNA level (gene/Actin)
200
150
100
50
0
****
CON
ITGB3OE
E
1 2 3 4 5 6 7 8
F
1 2 3 4 5 6 7 8
G
1 2 3 4 5 6 7 8
H
1 2 3 4 5 6 7 8
I
J
K
L
M
mRNA level (gene/Actin)
400
300
200
100
0
****
CON
OE
N
1 2 3 4 5 6 7 8
O
mRNA level (gene/Actin)
1.5
1.0
0.5
0.0
****
CON
ITGB3RNAi
P
mRNA level (gene/Actin)
1.5
1.0
0.5
0.0
***
CON
DSG2RNAi
Q
R
S
T

Fig. S3

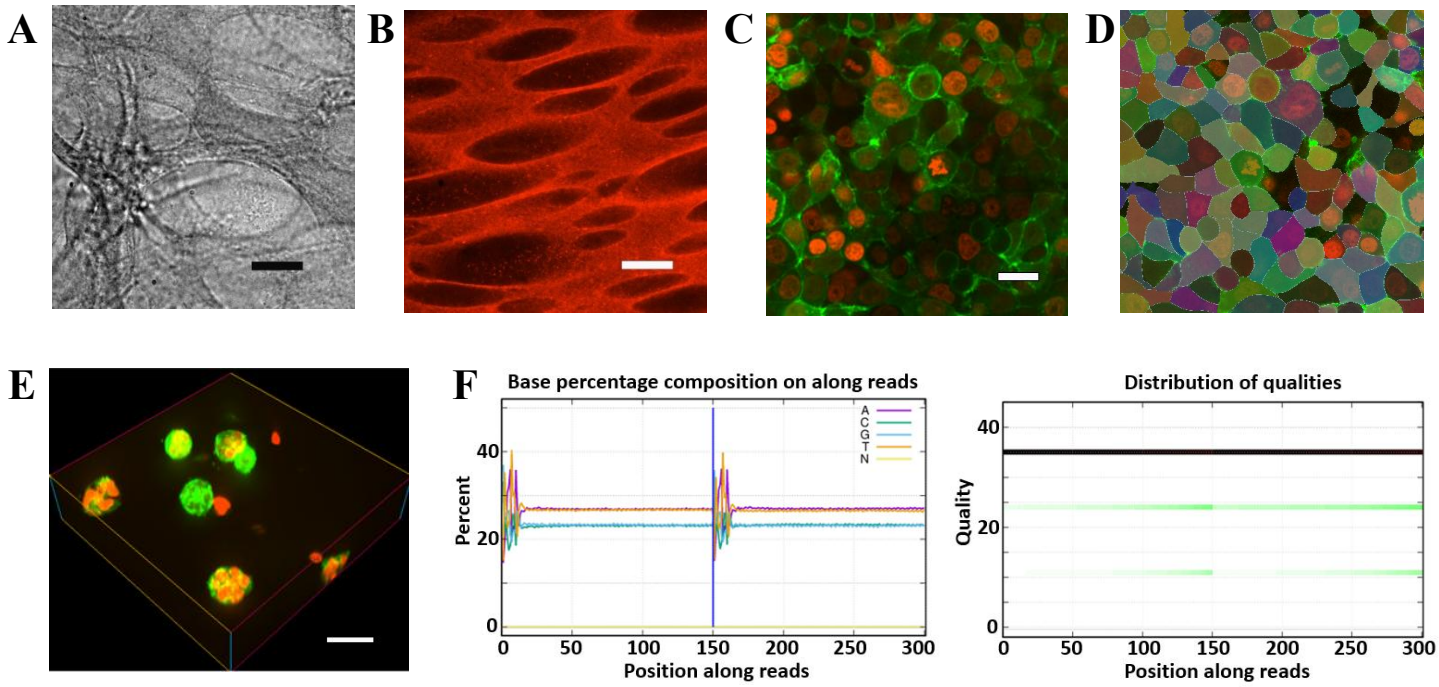
A
B
C
D
E
F
Base percentage composition on along reads
A
C
G
T
N
Percent
0
20
40
0
50
100
150
200
250
300
Position along reads
Distribution of qualities
Quality
0
20
40
0
50
100
150
200
250
300
Position along reads

Fig. S4

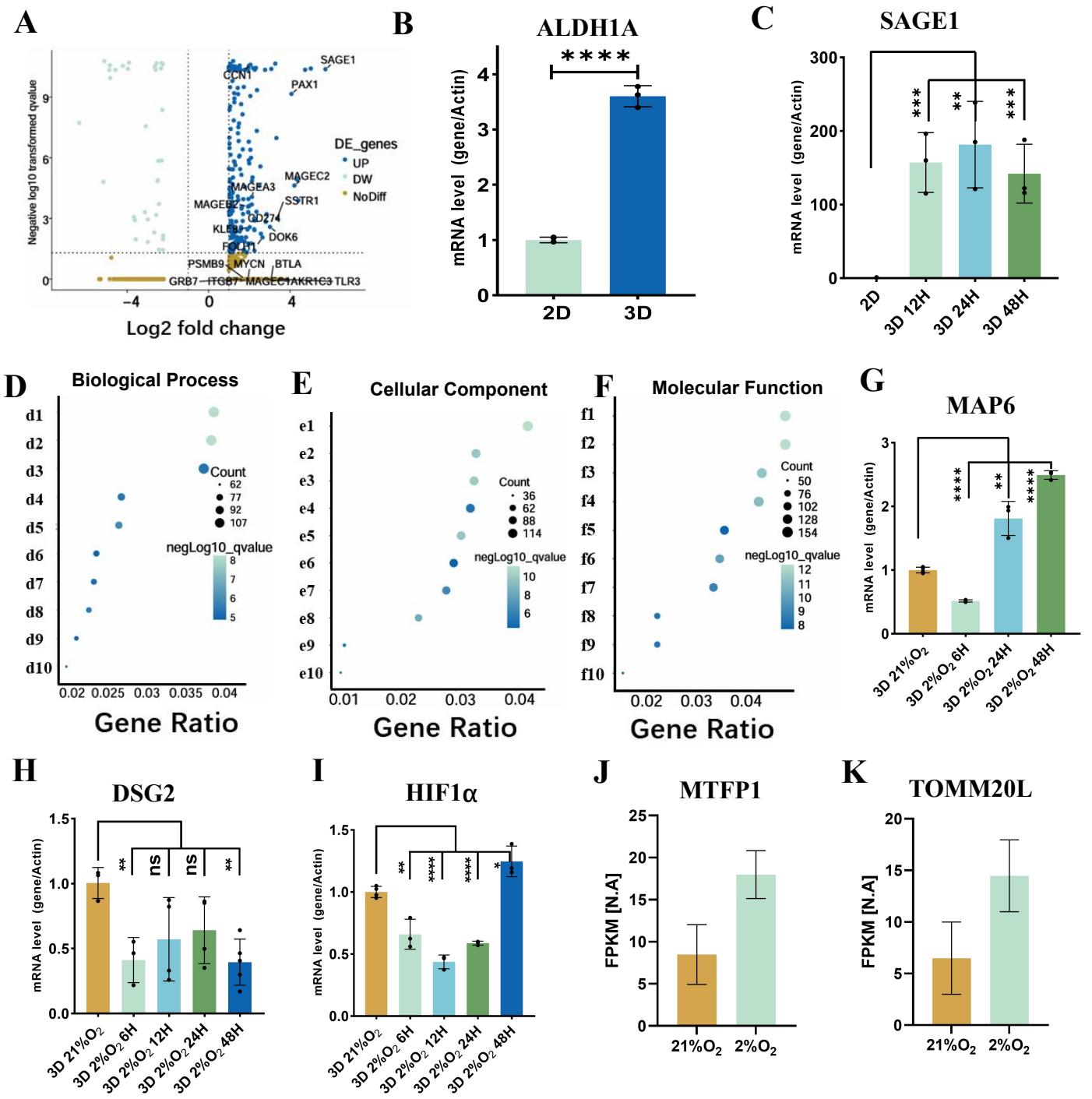
A
Negative log10 transformed qvalue
Log2 fold change
DE_genes
UP
DW
NoDiff
SAGE1
CCN1
PAX1
MAGEC2
MAGEA3
SSTR1
MAGEB2
CD274
KLRB1
DOK6
FOLH1
PSMB9
MYCN
BTLA
GRB7
ITGB7
MAGEC1
AKR1C3
TLR3
B
ALDH1A
mRNA level (gene/Actin)
2D
3D
C
SAGE1
mRNA level (gene/Actin)
2D
3D 12H
3D 24H
3D 48H
D
Biological Process
Count
negLog10_qvalue
Gene Ratio
E
Cellular Component
Count
negLog10_qvalue
Gene Ratio
F
Molecular Function
Count
negLog10_qvalue
Gene Ratio
G
MAP6
mRNA level (gene/Actin)
3D 21%O2
3D 2%O2 6H
3D 2%O2 24H
3D 2%O2 48H
H
DSG2
mRNA level (gene/Actin)
3D 21%O2
3D 2%O2 6H
3D 2%O2 12H
3D 2%O2 24H
3D 2%O2 48H
I
HIF1α
mRNA level (gene/Actin)
3D 21%O2
3D 2%O2 6H
3D 2%O2 12H
3D 2%O2 24H
3D 2%O2 48H
J
MTFP1
FPKM [N.A]
21%O2
2%O2
K
TOMM20L
FPKM [N.A]
21%O2
2%O2

Fig. S5

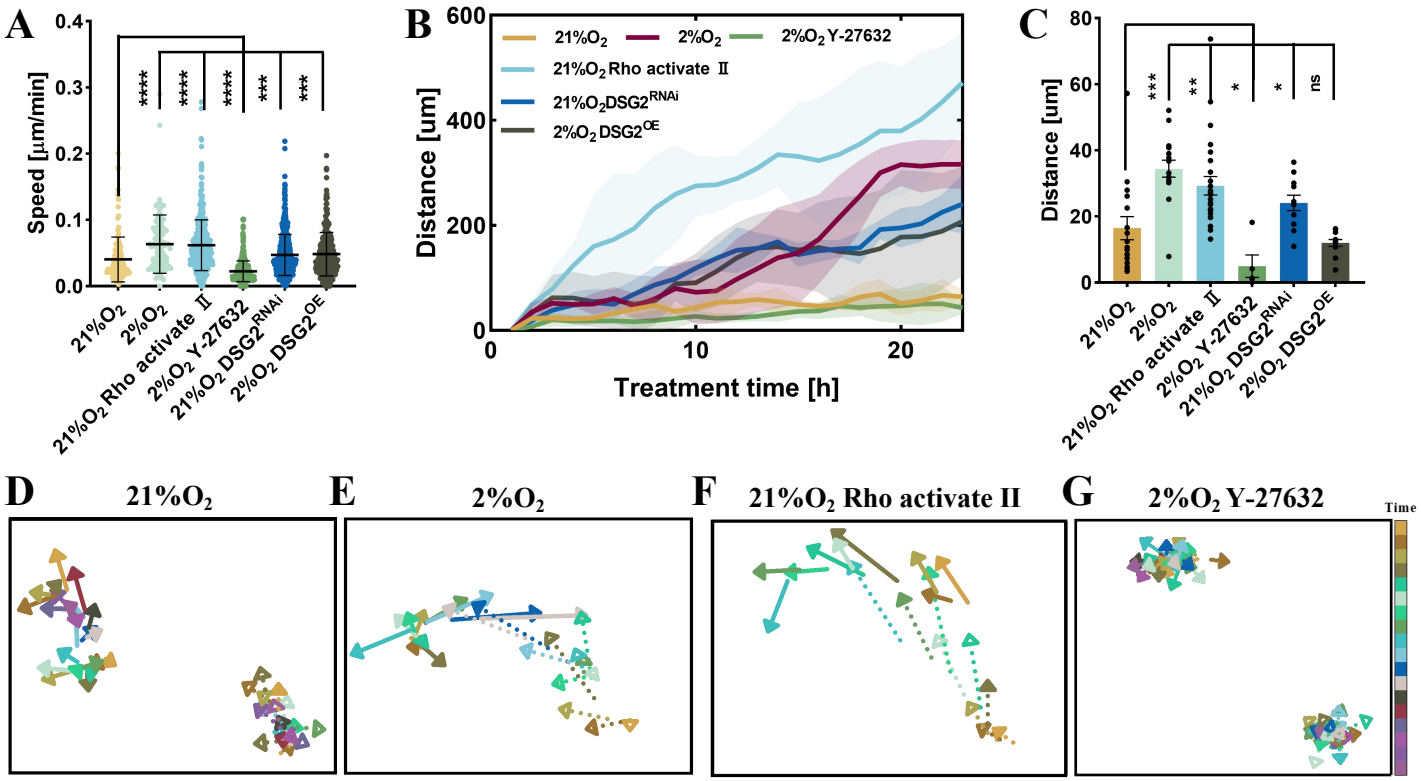
A
Speed [μm/min]
0.4
0.3
0.2
0.1
0.0
****
****
****
***
***
21%O2
2%O2
21%O2 Rho activate Ⅱ
2%O2 Y-27632
21%O2 DSG2RNAi
2%O2 DSG2OE
B
Distance [um]
600
400
200
0
21%O2
2%O2
2%O2 Y-27632
21%O2 Rho activate Ⅱ
21%O2DSG2RNAi
2%O2 DSG2OE
0
10
20
Treatment time [h]
C
Distance [um]
80
60
40
20
0
***
**
*
*
ns
21%O2
2%O2
21%O2 Rho activate Ⅱ
2%O2 Y-27632
21%O2 DSG2RNAi
2%O2 DSG2OE
D
21%O2
E
2%O2
F
21%O2 Rho activate II
G
2%O2 Y-27632
Time

Fig. S6

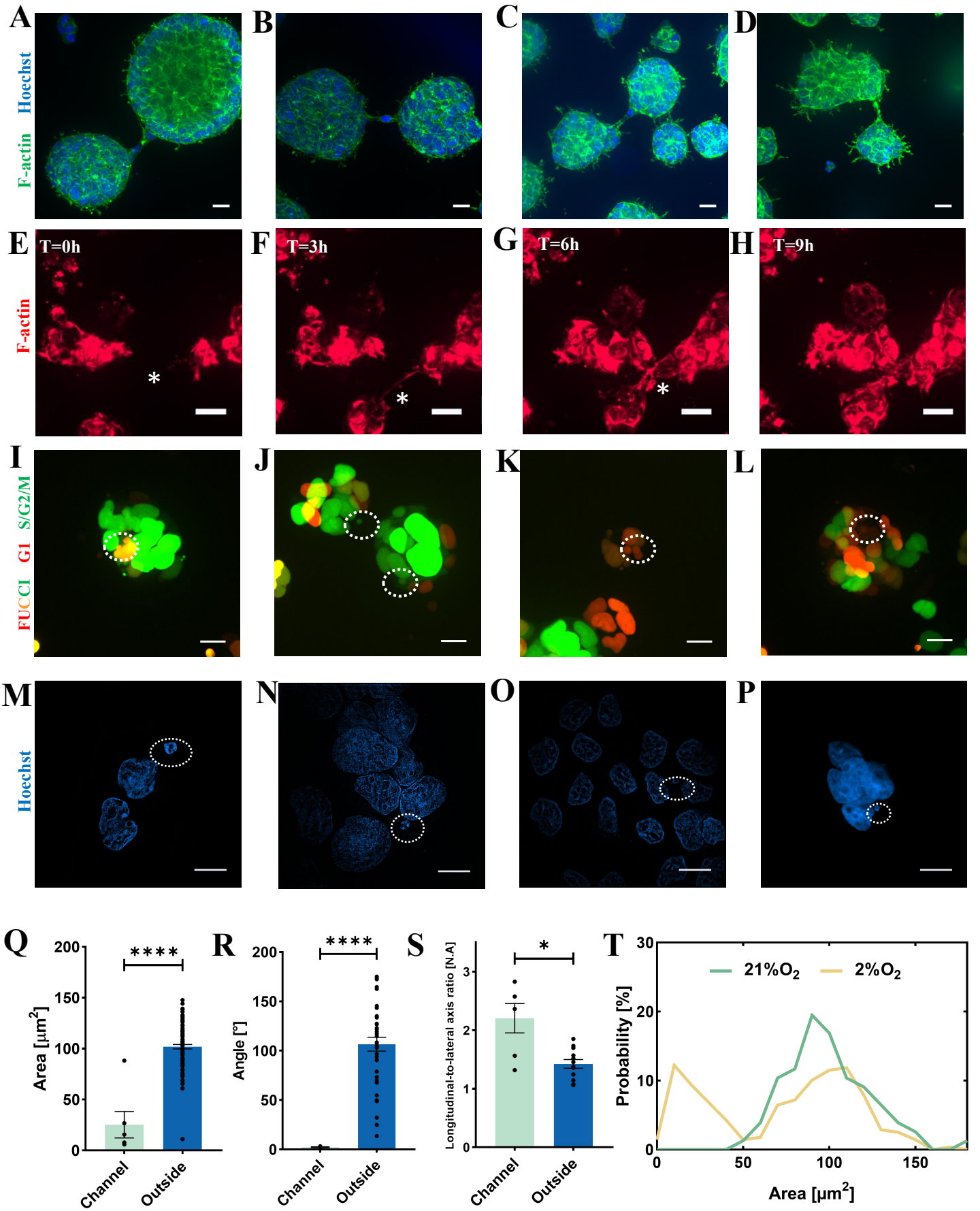
A
B
C
D
Hoechst
F-actin
E
T=0h
F
T=3h
G
T=6h
H
T=9h
F-actin
I
J
K
L
FUCCI
G1
S/G2/M
M
N
O
P
Hoechst
Q
Area [μm²]
****
Channel
Outside
R
Angle [°]
****
Channel
Outside
S
Longitudinal-to-lateral axis ratio [N.A]
*
Channel
Outside
T
21%O₂
2%O₂
Probability [%]
Area [μm²]

Fig. S7

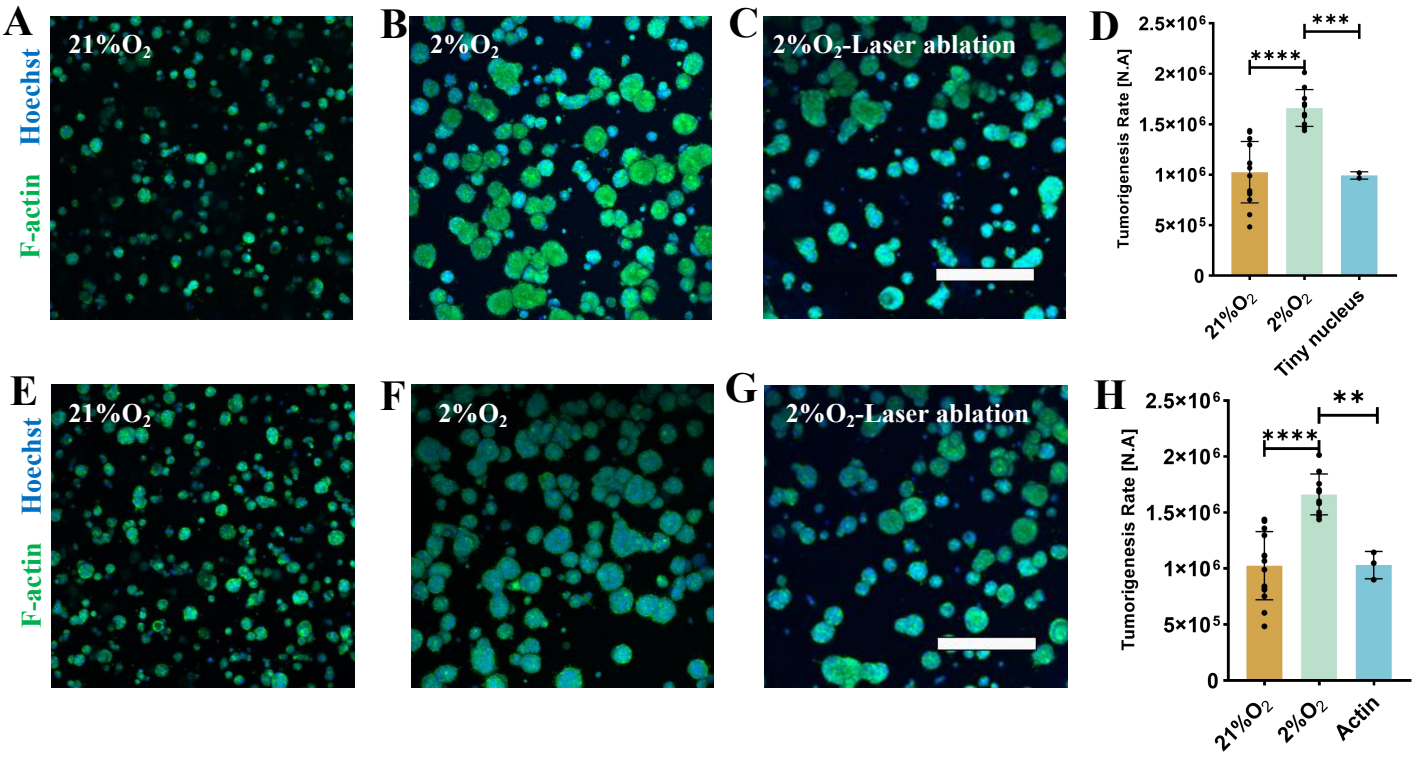
A
B
C
D
E
F
G
H
Hoechst
F-actin
21%O2
2%O2
2%O2-Laser ablation
Tumorigenesis Rate [N.A]
2.5×10^6
2×10^6
1.5×10^6
1×10^6
5×10^5
0
****
***
**
21%O2
2%O2
Tiny nucleus
Actin

Fig. S8

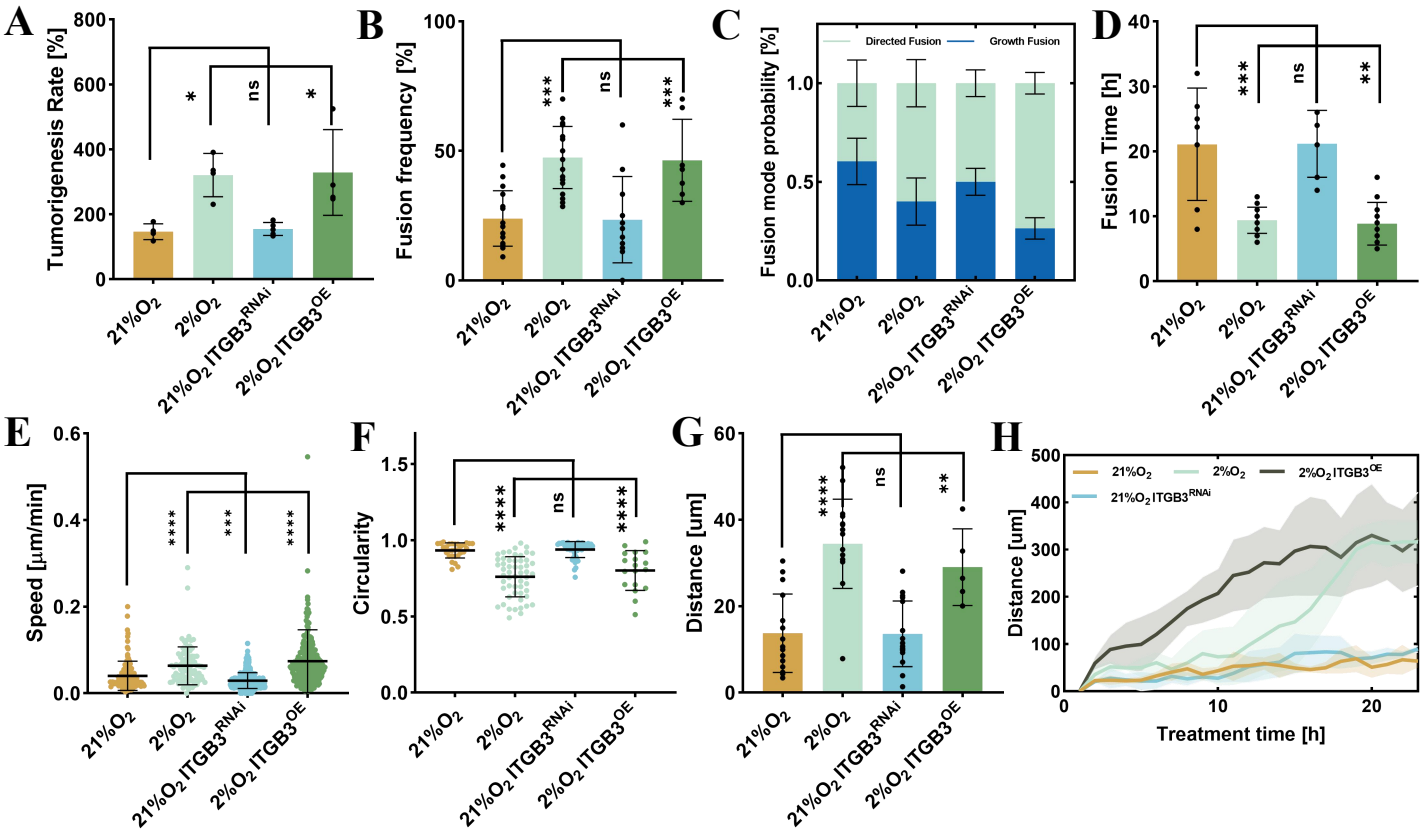
A
Tumorigenesis Rate [%]
800
600
400
200
0
*
ns
*
21%O2
2%O2
21%O2 ITGB3RNAi
2%O2 ITGB3OE
B
Fusion frequency [%]
100
50
0
***
ns
***
C
Fusion mode probability [%]
Directed Fusion
Growth Fusion
1.0
0.5
0.0
D
Fusion Time [h]
40
30
20
10
0
***
ns
**
E
Speed [µm/min]
0.6
0.4
0.2
0.0
****
***
****
F
Circularity
1.5
1.0
0.5
0.0
****
ns
****
G
Distance [um]
60
40
20
0
****
ns
**
H
Distance [um]
500
400
300
200
100
0
21%O2
2%O2
2%O2 ITGB3OE
21%O2 ITGB3RNAi
0
10
20
Treatment time [h]

Fig. S9

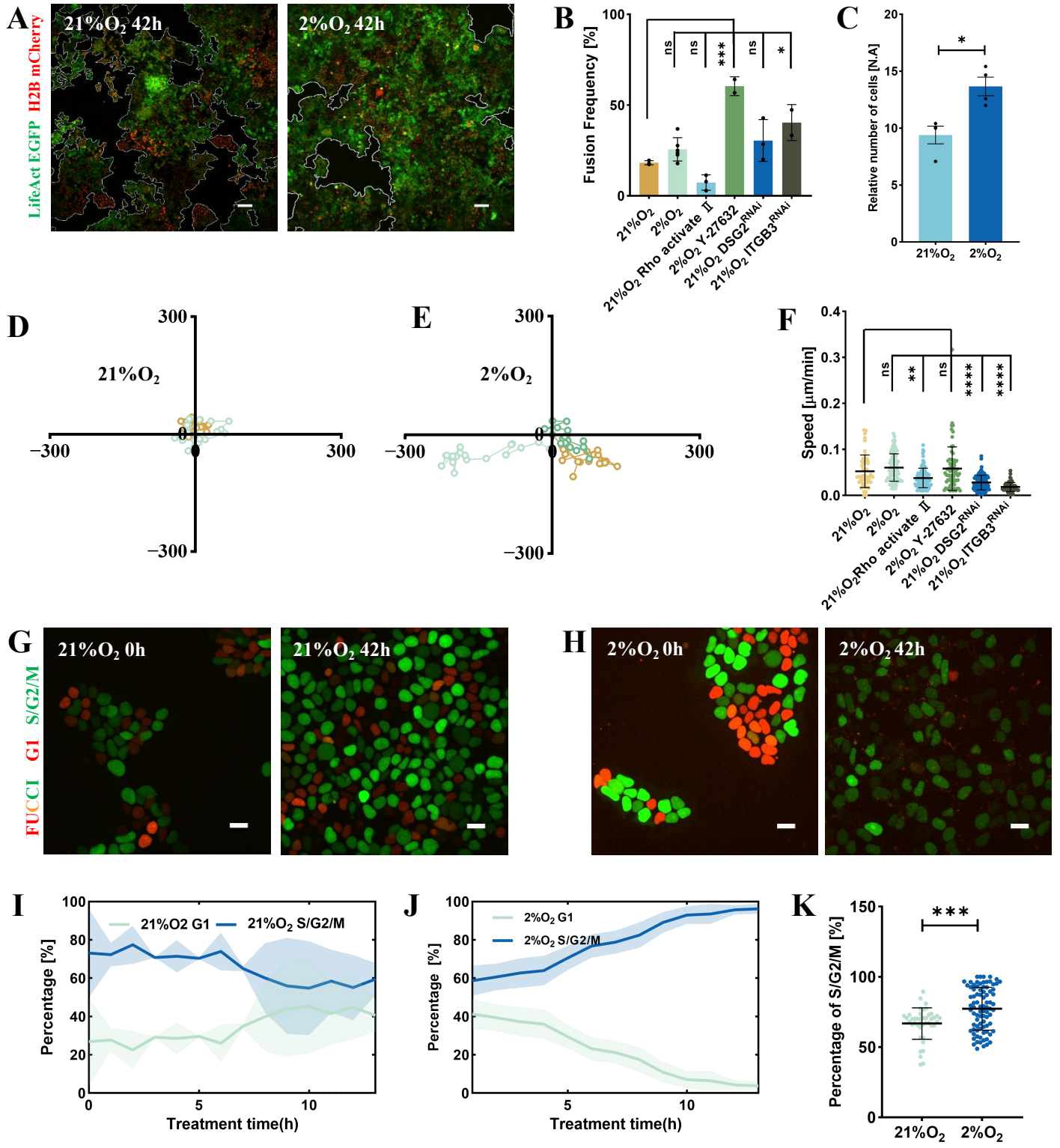
A
LifeAct EGFP H2B mCherry
21%O2 42h
2%O2 42h
B
Fusion Frequency [%]
ns
ns
***
ns
*
21%O2
2%O2
21%O2 Rho activate II
2%O2 Y-27632
21%O2 DSG2RNAi
21%O2 ITGB3RNAi
C
Relative number of cells [N.A]
*
21%O2
2%O2
D
21%O2
E
2%O2
F
Speed [μm/min]
ns
**
ns
****
****
21%O2
2%O2
21%O2Rho activate II
2%O2 Y-27632
21%O2 DSG2RNAi
21%O2 ITGB3RNAi
G
FUCCI G1 S/G2/M
21%O2 0h
21%O2 42h
H
2%O2 0h
2%O2 42h
I
21%O2 G1
21%O2 S/G2/M
Percentage [%]
Treatment time(h)
J
2%O2 G1
2%O2 S/G2/M
Percentage [%]
Treatment time(h)
K
Percentage of S/G2/M [%]
***
21%O2
2%O2

Fig. S10

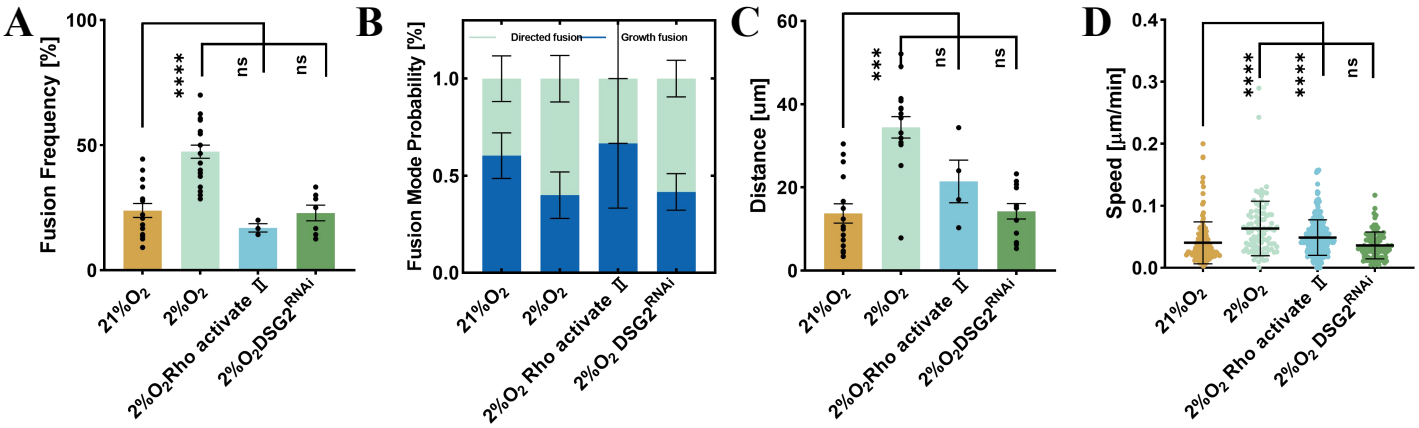
A
Fusion Frequency [%]
100
50
0
****
ns
ns
21%O2
2%O2
2%O2Rho activate Ⅱ
2%O2DSG2RNAi
B
Fusion Mode Probability [%]
Directed fusion
Growth fusion
1.0
0.5
0.0
21%O2
2%O2
2%O2 Rho activate Ⅱ
2%O2 DSG2RNAi
C
Distance [um]
60
40
20
0
***
ns
ns
21%O2
2%O2
2%O2Rho activate Ⅱ
2%O2DSG2RNAi
D
Speed [μm/min]
0.4
0.3
0.2
0.1
0.0
****
****
ns
21%O2
2%O2
2%O2 Rho activate Ⅱ
2%O2 DSG2RNAi

Fig. S11

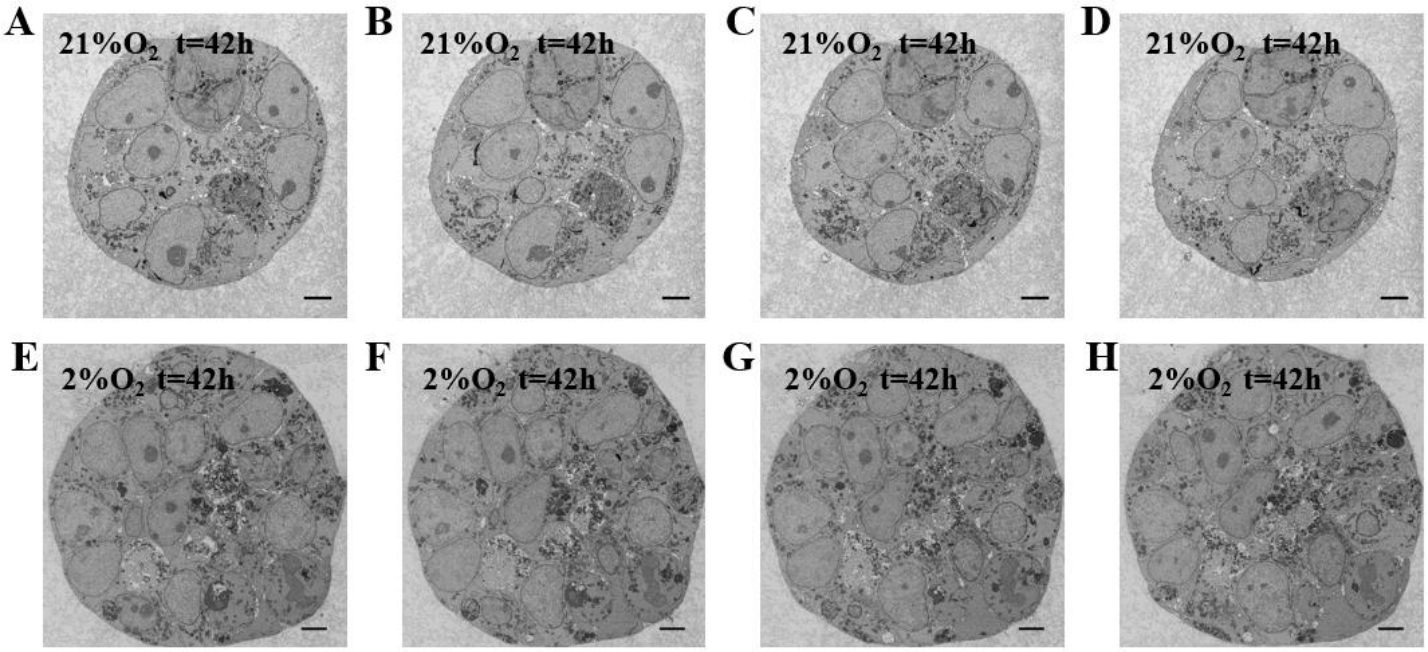
A
21%O2 t=42h
B
21%O2 t=42h
C
21%O2 t=42h
D
21%O2 t=42h
E
2%O2 t=42h
F
2%O2 t=42h
G
2%O2 t=42h
H
2%O2 t=42h

Fig. S12

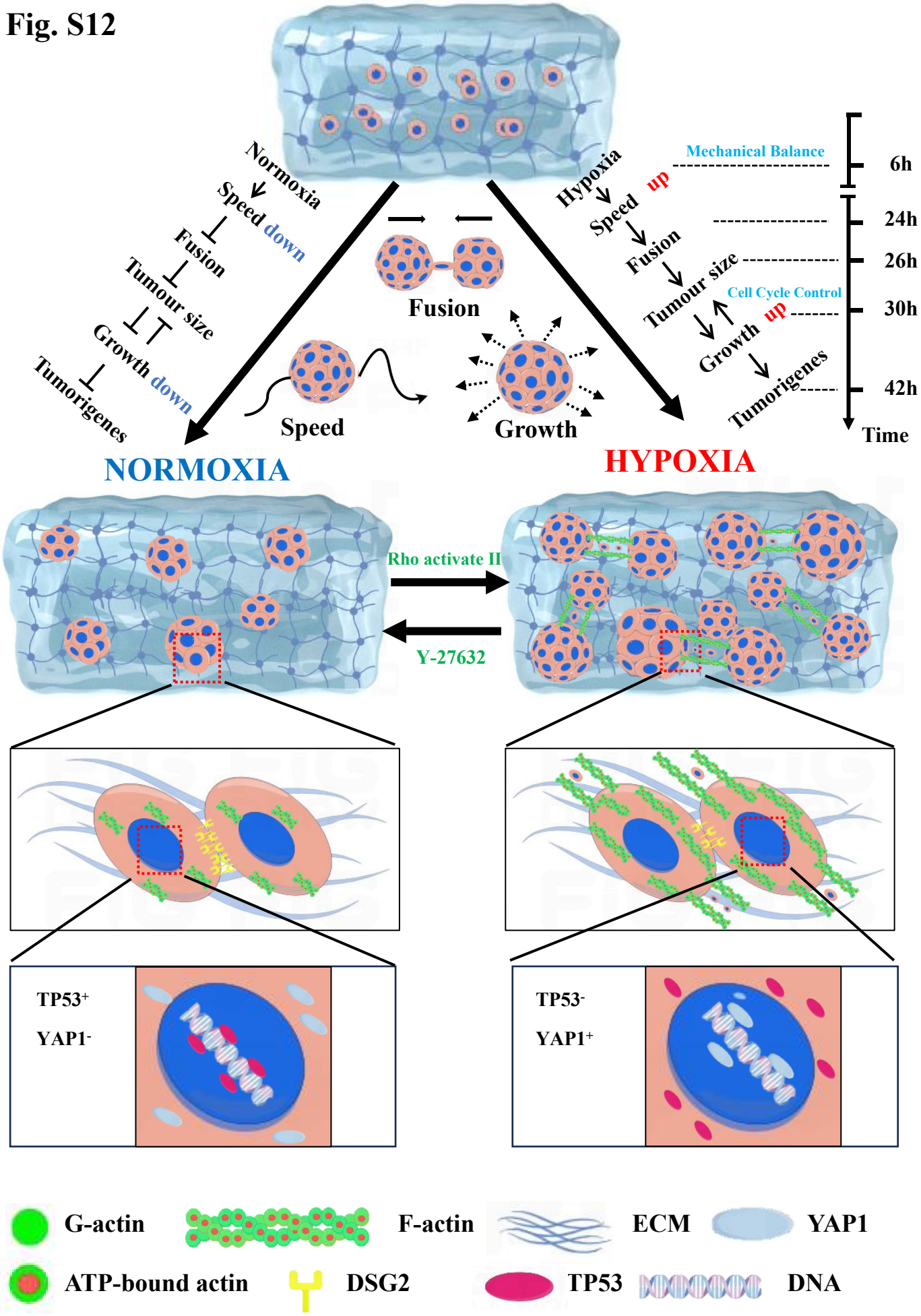
Normoxia
Speed down
Fusion
Tumour size
Growth down
Tumorigenes
Fusion
Speed
Growth
Hypoxia
Speed up
Fusion
Tumour size
Growth up
Tumorigenes
Mechanical Balance
Cell Cycle Control
6h
24h
26h
30h
42h
Time
NORMOXIA
HYPOXIA
Rho activate II
Y-27632
TP53+
YAP1-
TP53-
YAP1+
G-actin
F-actin
ECM
YAP1
ATP-bound actin
DSG2
TP53
DNA

Fig. S13

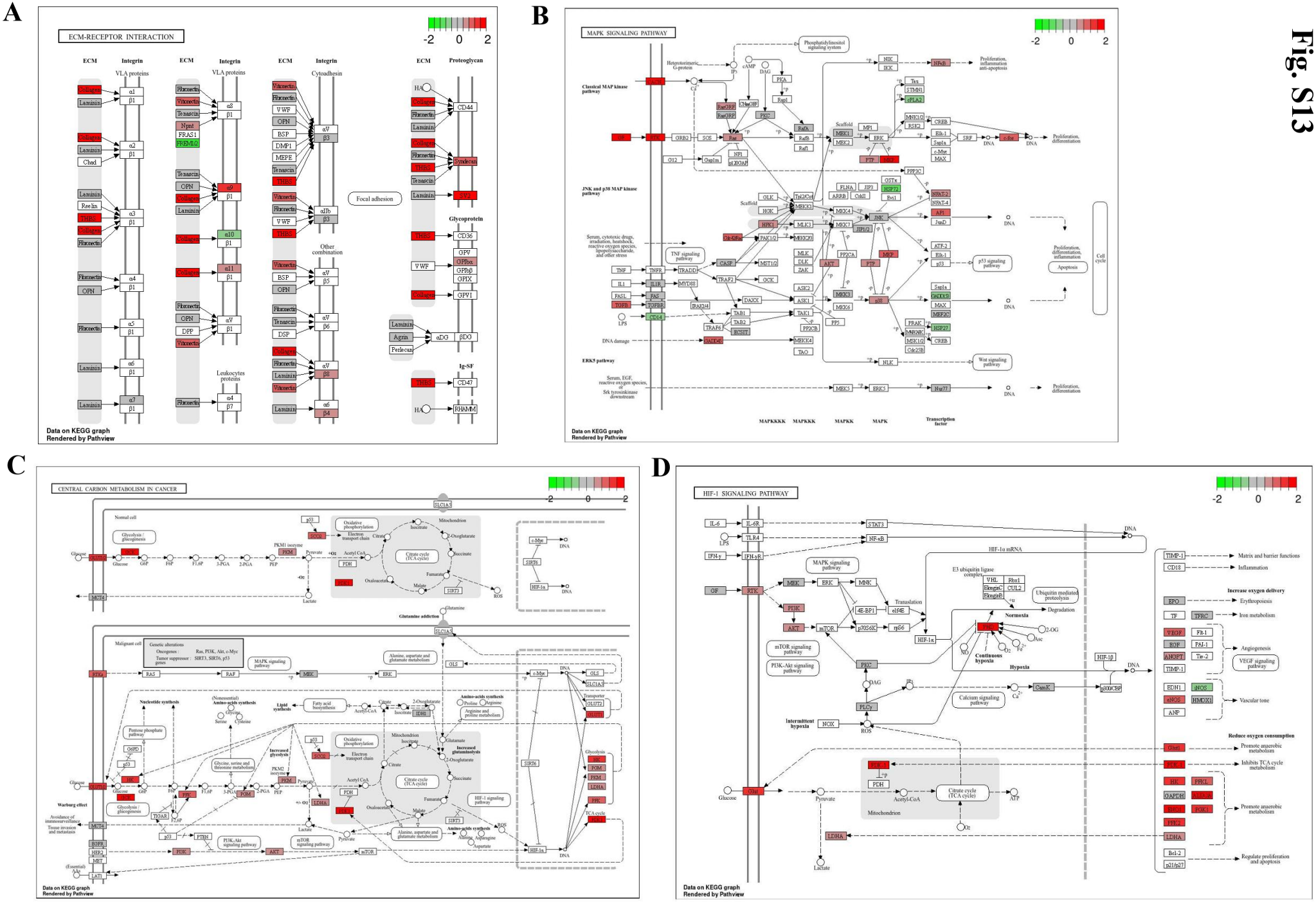
A
ECM-RECEPTOR INTERACTION
-2 0 2
ECM
Integrin
VLA proteins
Cytoadhesin
Proteoglycan
Focal adhesion
Other combination
Leukocytes proteins
Glycoprotein
Ig-SF
Data on KEGG graph
Rendered by Pathview
B
MAPK SIGNALING PATHWAY
Classical MAP kinase pathway
JNK and p38 MAP kinase pathway
ERK5 pathway
MAPKKKK
MAPKKK
MAPKK
MAPK
Transcription factor
Data on KEGG graph
Rendered by Pathview
C
CENTRAL CARBON METABOLISM IN CANCER
Normal cell
Malignant cell
Glutamine addiction
Warburg effect
Data on KEGG graph
Rendered by Pathview
D
HIF-1 SIGNALING PATHWAY
Normoxia
Hypoxia
Continuous hypoxia
Intermittent hypoxia
Increase oxygen delivery
Reduce oxygen consumption
Data on KEGG graph
Rendered by Pathview

Fig. S14

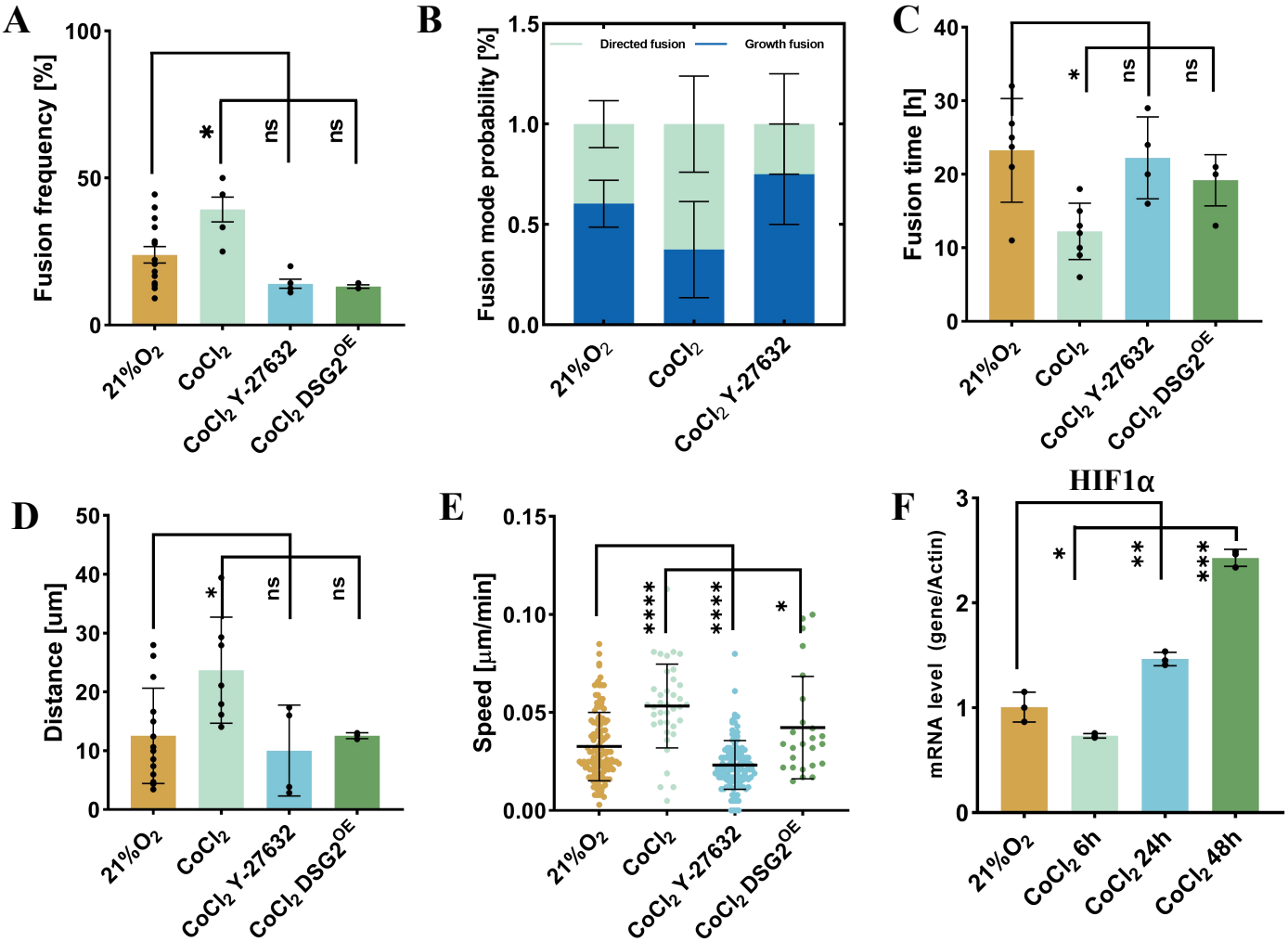
A
Fusion frequency [%]
100
50
0
*
ns
ns
21%O2
CoCl2
CoCl2 Y-27632
CoCl2 DSG2OE
B
Fusion mode probability [%]
1.5
1.0
0.5
0.0
Directed fusion
Growth fusion
21%O2
CoCl2
CoCl2 Y-27632
C
Fusion time [h]
40
30
20
10
0
*
ns
ns
21%O2
CoCl2
CoCl2 Y-27632
CoCl2 DSG2OE
D
Distance [um]
50
40
30
20
10
0
*
ns
ns
21%O2
CoCl2
CoCl2 Y-27632
CoCl2 DSG2OE
E
Speed [μm/min]
0.15
0.10
0.05
0.00
****
****
*
21%O2
CoCl2
CoCl2 Y-27632
CoCl2 DSG2OE
F
HIF1α
mRNA level (gene/Actin)
3
2
1
0
*
**
***
21%O2
CoCl2 6h
CoCl2 24h
CoCl2 48h